THE GAMMA-RAY ANGULAR DISTRIBUTION FROM THE REACTION $D(p,\gamma)^3He$ BELOW 200 KeV

by

MIGUEL ANGEL OLIVO

Licenciado en Fisica
Instituto de Fisica de S.C. de Bariloche,
Universidad Nacional de Cuyo, 1962

A THESIS SUBMITTED IN PARTIAL FULFILMENT
OF THE REQUIREMENTS FOR THE DEGREE OF

DOCTOR OF PHILOSOPHY
In the Department of
PHYSICS

We accept this thesis as conforming to the
required standard

THE UNIVERSITY OF BRITISH COLUMBIA

August, 1968

In presenting this thesis in partial fulfilment of the requirements for an advanced degree at the University of British Columbia, I agree that the Library shall make it freely available for reference and Study. I further agree that permission for extensive copying of this thesis for scholarly purposes may be granted by the Head of my Department or by his representatives. It is understood that copying or publication of this thesis for financial gain shall not be allowed without my written permission.

Department of Physics

The University of British Columbia
Vancouver 8, Canada

Date August 8th, 1968

ABSTRACT

The angular distribution of the gamma-rays from the direct radiative capture reaction $D(p,\gamma)^3He$ has been measured for 70 KeV and 144 KeV protons in the laboratory system, using thin deuterated polyethylene targets.

The study of this particularly simple reaction is of interest for determining some properties of the forces which bind nuclear particles to each other. In addition it plays a role in a number of astrophysical processes.

The ground state of ^3He is predominantly a symmetric ^2S state with admixtures of a ^4D state and a $^2S_{(m)}$ state of mixed symmetry. These admixtues are related to specific components of the two body forces coupling the three particles.

The measurements were made with a high current 180 KeV accelerator, built by the author, using an ORTEC duoplasmatron ion source. Technical problems involved in the development of the accelerator and the deuterated targets are discussed.

The angular distribution at 144 ± 16 KeV in terms of Legendre polynomials P_l is given in the centre of mass system by

$$W(\theta) = A_o\left[P_o+(.05\pm.02)P_1-(.94\pm.02)P_2-(.05\pm.02)P_3+(.03\pm.02)P_4\right]$$

and at 70 ± 20 KeV the angular distribution is given by

$$W(\theta) = A_o\left[P_o+(.06\pm.04)P_1-(.93\pm.05)P_2-(.06\pm.04)P_3+(.02\pm.05)P_4\right]$$

The coefficients in the Legendre polynomial expansion are related to the various transitions between the continuum and bound states. Their significance in terms of the different components of the ^{3}He ground state wave function is discussed.

The absolute cross section (i.e. the coefficient A_o) has not been measured. Plans for measuring it in the near future are discussed briefly.

TABLE OF CONTENTS

LIST OF TABLES

LIST OF FIGURES

ACKNOWLEDGEMENTS

I wish to express my sincere gratitude to Dr. G.M. Griffiths for his untiring supervision and conscientious assistance during the course of this work. His approachability together with his understanding of the problems involved, particularly the language problem, made this thesis possible.

The helpful discussions of Drs. G.M. Bailey, J.H. Williamson and P.H.R. Orth on various aspects of this work is appreciated. Furthermore, I wish to thank Mr. D. Hepburn and Dr. G.M. Bailey for their kind assistance in obtaining experimental data during the painfully long hours of the night.

The assistance of the members of the workshop and of the Van de Graaff group and in particular that of the late G. Lang is thankfully acknowledged.

The author is deeply grateful to Dr. J.B. Warren for extending a scholarship to the University of British Columbia.

To Dr. Ian McTaggart-Cowan, Dean of Graduate Studies, and other authorities of the University of British Columbia who made possible the transfer of my studies to the Ph.D. program of this University.

Al Consejo Nacional de Investigaciones Cientificas y Tecnicas de la Republica Argentina que posibilito mi viaje a esta Universidad.

A mis padres por su constante apoyo durante el transcurso de mis estudios.

To my wife and Miguelito.

PUBLICATIONS

"Low Cost Deuterated Polyethylene Targets of Controlled Thickness for High Current Accelerators",

M.A. Olivo and G.M. Bailey,
Nucl. Instr. and Meth., 57 (1967) 353.

"Use of the Maximum Likelihood Technique for Fitting Counting Distributions. Part II. Application to Angular Distributions",

P.H.R. Orth and M.A. Olivo,
Nucl. Instr. and Meth., (to be published).

CHAPTER I

INTRODUCTION

1.1. General Introduction

Direct radiative capture reactions in nuclear physics involve a one-step transition between continuum and bound states of a particle where the energy difference is transferred to the electromagnetic field and no intermediate compound state is formed.

These reactions provide a relatively simple way of obtaining information about the bound state wave functions, since the properties of the continuum states can be inferred from scattering data and the properties of the relatively weak electromagnetic interaction are well known. Another direct capture process known as a stripping reaction occurs when the neutron or proton from an incident deuteron is transferred from the continuum to a bound state in the final nucleus, while the energy difference is taken up by the other particle (proton or neutron) from the deuteron. Similar information concerning the properties of bound states can be inferred from stripping and from direct radiative capture processes, however, the radiative capture is in practice more direct since it is mediated by the well understood electromagnetic interaction. On the other hand stripping depends on the much less well known strong nuclear interaction, not only in forming the continuum and bound states but also in the transfer process between them. It might be noted however, that because

of the relative weakness of the electromagnetic coupling, the probability for direct radiative capture is in general several orders of magnitude smaller than that for stripping.

There is a correlation between the structure of the bound state wave functions and specific properties of the nuclear forces. For few-nucleon systems many theoretical studies have been carried out to specify the nature of these correlations in a quantitative way. Therefore, knowledge about the bound state wave functions should in principle provide some understanding of the fundamental interaction between nucleons.

The reaction $D(p,\gamma)^3He$ is particularly useful in obtaining this kind of information because:

1. The continuum states can be determined from proton-deuteron scattering data.
2. The continuum and bound states are coupled by the electromagnetic field which is known exactly, and
3. Due to the weakness of the electromagnetic interaction first-order perturbation theory can be used with some confidence in computing transition probabilities, or cross sections.

Further, the fact that the bound state of ^3He has both singlet and triplet two-nucleon spin configurations and is more tightly bound than the two body system (deuteron) indicates that the study of this reaction could reveal properties of the nucleon-nucleon force to which the deuteron is insensitive, such as short

range components of the nuclear force or components sensitive to singlet spin configurations.

The study of the reaction $D(p,\gamma)^3He$ is also of interest in a number of astrophysical processes. In the hydrogen-burning stage of small main sequence stars, the main energy supply comes from a series of reactions known as the p-p chain in which the reaction $D(p,\gamma)^3He$ is the second step:

$$p + p \longrightarrow D + \beta^+ + \nu$$
$$p + D \longrightarrow {}^3He + \gamma$$
$${}^3He + {}^3He \longrightarrow {}^4He + 2p$$

The rate of energy release in the p-p chain is controlled by the first reaction since the β interaction is much weaker than the electromagnetic and nuclear interactions. However, the reaction $D(p,\gamma)^3He$ may have a significant effect on the rate of condensation of a star towards the main sequence, depending on the initial amount of deuterium, since it is the first reaction to supply nuclear energy as the star condenses.

Furthermore, the $D(p,\gamma)^3He$ competes with the reaction $D(d,n)^3He$ thus influencing the number of neutrons available from a given initial amount of deuterium. Although the latter reaction has a cross section of a several order of magnitude greater than the $D(p,\gamma)^3He$ cross section the very much larger density of protons compared with deuterium would place the $D(p,\gamma)^3He$ in a competitive position. The neutron yield is of interest, because it is believed that the neutron captures have influenced heavy elements

isotope ratios in the early stages of the solar system.

1.2. Review of Previous Work

The existence of the weak capture gamma radiation from the proton bombardment of deuterium was first reported by Curran and Strothers in 1939 (CU 39). Further investigations of this reaction were performed ten years later by Fowler, Lauritsen and Tollestrup (FO 49). It was found that the angular distribution at a bombarding energy of 1.4 MeV was nearly pure $\sin^2\theta$. This implies that the radiation involved emanates from an electric dipole aligned with the direction of the incident proton. From the yield, obtained at 90°, as a function of the bombarding energy from 0.5 to 1.5 MeV it was also shown that the cross section was non-resonant in character indicating a direct capture process.

In 1952 Wilkinson (WI 52) measured the polarization of the emitted gamma radiation showing that at 90° the gamma-rays were plane polarized with the electric dipole in the reaction plane, therefore, confirming the suggestion of Fowler et. al. that the capture resulted from the emission of E1 radiation as the proton made a transition from a continuum p-wave to the ground s-state of ^{3}He. He also suggested that the spin-orbit coupling must be small since the $\sin^2\theta$ distribution was very pure, while spin-orbit coupling would induce transitions in which $\Delta J_z = \pm 1$, with a distribution proportional to $(1 + \cos^2\theta)$. The main transitions correspond to $\Delta J_z = 0$, with a $\sin^2\theta$ distribution. A significant amount of spin-orbit coupling would then give rise to gamma-ray yield at 0°.

In 1955, with the advent of the scintillation detectors, Griffiths and Warren (GR 55) measured the angular distribution between 0.5 and 2.0 MeV using heavy ice targets. They found that the distribution was proportional to $(a + b \sin^2\theta)$ where $\underline{a}$ was small but not zero, and therefore put particular emphasis on the region around 0° in order to determine the amount contributed by the spin-orbit interaction. They found however, that the energy dependence of the yield at 0° was different from that at 90°. This suggested the possibility that the isotropic component might arise from magnetic dipole transitions following the capture of s-wave protons. Such transitions may arise from non-central components in the nuclear force (VE 50). These authors also obtained an approximate value for the absolute cross section at $E_p = 1.0$ MeV, of $4 \times 10^{-30} (\pm 50\%)$ cm^2.

Measurements on the reaction $D(p,\gamma)^3He$ were later repeated by Griffiths et. al. (GR 62), who measured the cross section and the angular distribution for proton energies from 275 KeV to 1.75 MeV with more accuracy using both heavy ice and gas targets. Their results confirmed the assumption that the radiation observed at 0° is due to s-wave capture.

Because the s-wave capture should be more predominant with respect to the p-wave capture at low energies, Griffiths et. al. (GR 63) measured the yield and angular distribution of this reaction in the energy range from 24 to 48 KeV using heavy ice targets confirming once more the previous arguments. Assuming a

simplified energy dependence for the cross section they analized the results to give separate cross section for p-wave and s-wave captures. At 25 KeV in the laboratory frame the cross sections are:

$$\sigma_p = (2.9 \pm 0.3) \times 10^{-32} \text{ cm}^2$$
$$\sigma_s = (1.3 \pm 0.3) \times 10^{-32} \text{ cm}^2$$

Recently Wölfli et. al. (WO 66) have measured the capture cross section between 2 MeV and 12 MeV including angular distributions for several energies up to 5.25 MeV.

1.3. Present Work

This work was originally undertaken in order to obtain more accurate data on the absolute cross section at low energies both because this reaction is of interest in astrophysics, and because more detailed theoretical calculations were becoming available.

Recent theoretical studies on the three body system, in particular this reaction, indicate that an accurate determination of the angular distribution and of the absolute cross section including its energy dependence, would, in principle, provide information about the fundamental interaction between the particles.

An early group theoretical classification of the permutation symmetries of the states of the three nucleon system was made by Verde (VE 50) for the purpose of calculating transition probabilities between continuum and bound states. A more detailed

classification was considered by Derrick and Blatt (DE 58) for the ground states. In this work the relation between the wave function and the central, tensor and spin dependent parts of the nucleon-nucleon force was considered. Recently a more detailed discussion of the radiative transitions on the basis of better wave functions has been given by Eichmann (EI 63), and a more complete classification of all possible radiative transitions has been presented by Davis (DA 67). More complete lists of references are given in these two papers.

The data obtained from the present work is compared with somewhat empirical theoretical calculations of direct radiative capture cross sections in three nucleon systems given by Donnelly (DO 67) and Bailey, Griffiths and Donnelly (BA 67) in which a two body approximation to the three nucleon system was used. Donnelly's theory has been used as a basis for comparison, because at the present time it provides numerical results in the energy range of interest which are based on accurate Coulomb penetrabilities. More extensive comparisons with theory will be made after the absolute cross section has been measured.

The ^{3}He ground state is known to have total angular momentum $J = 1/2$. The ground state wave function may then contain any one of, or a linear combination of the following components (SA 55):

$$^2S_{\frac{1}{2}} \qquad ^2P_{\frac{1}{2}} \qquad ^4P_{\frac{1}{2}} \qquad ^4D_{\frac{1}{2}}$$

Furthermore, the functions corresponding to each component can be classified according to their permutation symmetry properties. For three particles the individual space, spin and isospin parts of the wave function can be decomposed into symmetric, antisymmetric and mixed-symmetry parts. If the spatial part of the wave function is symmetric then the spin-isospin part must be antisymmetric to satisfy the Pauli Exclusion Principle.

A brief summary is given here of how these various components of the ground state wave function arise and how they contribute to the structure of the ground state of the ^{3}He. The space-symmetric ^{2}S state must be the main contribution to the ground state since it has the lowest kinetic energy of all three nucleon states. Further, it would be the only component of the ground state if the nuclear force were central and spin-independent. The other components are then present only because they are coupled to the ^{2}S state by additional parts of the two nucleon interaction.

Derrick (DE 60) has shown that the mixed-symmetry $^2S_{(m)}$ state is coupled to the symmetric ^{2}S state due to the difference between the central triplet even and singlet even forces, and that the ^{4}D state is coupled in by the tensor-even force component. Derrick (DE 60) has also shown that the amplitudes of the ^{2}P and ^{4}P components, which would be coupled in by the $\vec{L}.\vec{S}$ interaction, are negligible. Recently, however, Davis (DA 67) has partially refuted Derrick's arguments.

In order to obtain an estimate of the effect that admixtures of mixed symmetry $^2S_{(m)}$ state and ^4D state have on the radiative capture process Donnelly (DO 67) has introduced arbitrary amplitudes for states which approximate the character of these admixtures into the ground state symmetric ^2S wave function.

The wave functions were generated for a square well potential representing the interaction of a proton and a deuteron in both bound and free states. In this model many of the specific three body aspects of the problem have been neglected so that the amplitude factors introduced cannot be directly related to the properties of the nucleon-nucleon forces coupling the three particles. However, there is reason to believe that the functions generated by Donnelly are approximately correct outside the range of the specifically nuclear part of the force and should therefore lead to reasonable cross sections at low energies, for which most of the cross section arises from parts of the nuclear wave function outside the conventional nuclear radius. In this model square well parameters for the ground state were adjusted to fit the binding energy of the proton in ^3He (5.49 MeV) assuming it is predominantly a symmetric ^2S state, and parameters for the continuum states were adjusted as a function of energy to fit scattering data. Donnelly calculated angular distributions and cross sections to be expected on this model as a function of energy for a range of values for the arbitrary amplitude parameters.

In this thesis the angular distribution is determined

at two bombarding energies 90 and 160 KeV in the laboratory frame, and the results compared with Donnelly's predictions.

A brief description of the technique to be used, in the future, to determine the absolute cross section is outlined in Chapter IV.

CHAPTER II

EXPERIMENTAL APPARATUS

This chapter is concerned with the design parameters and the technical problems associated with the development of the apparatus used to measure the angular distribution of the radiation from the reaction $D(p,\gamma)^3He$.

2.1. Angular Distribution Table

A schematic drawing of the angular distribution table, designed by the author, is shown in Fig. II-1. Two aluminium "I" beams (A) are supported by ball bearings on an aluminium table so they can rotate about the centre post (B). The centre post has a concentric hole which locates the target chamber on the rotation axis. The detectors with a hundred pounds of lead for shielding and collimation were mounted on trolleys (C) so they roll in the radial direction on the "I" beams (A). A disc graduated in one degree steps was mounted on the centre post to define the angles between both detectors and the incident beam. The whole assembly is sufficiently rigid that rotating the heavy detector assemblies does not effect target-detector centering or distance.

The system was aligned using a theodolite. The collimator, which defined the direction of the beam, was adjusted until its axis met the tip of a pointed spindle inserted in the centre post in place of the target chamber. The axes of the detectors were defined by fine wires placed on the detector's collimator.

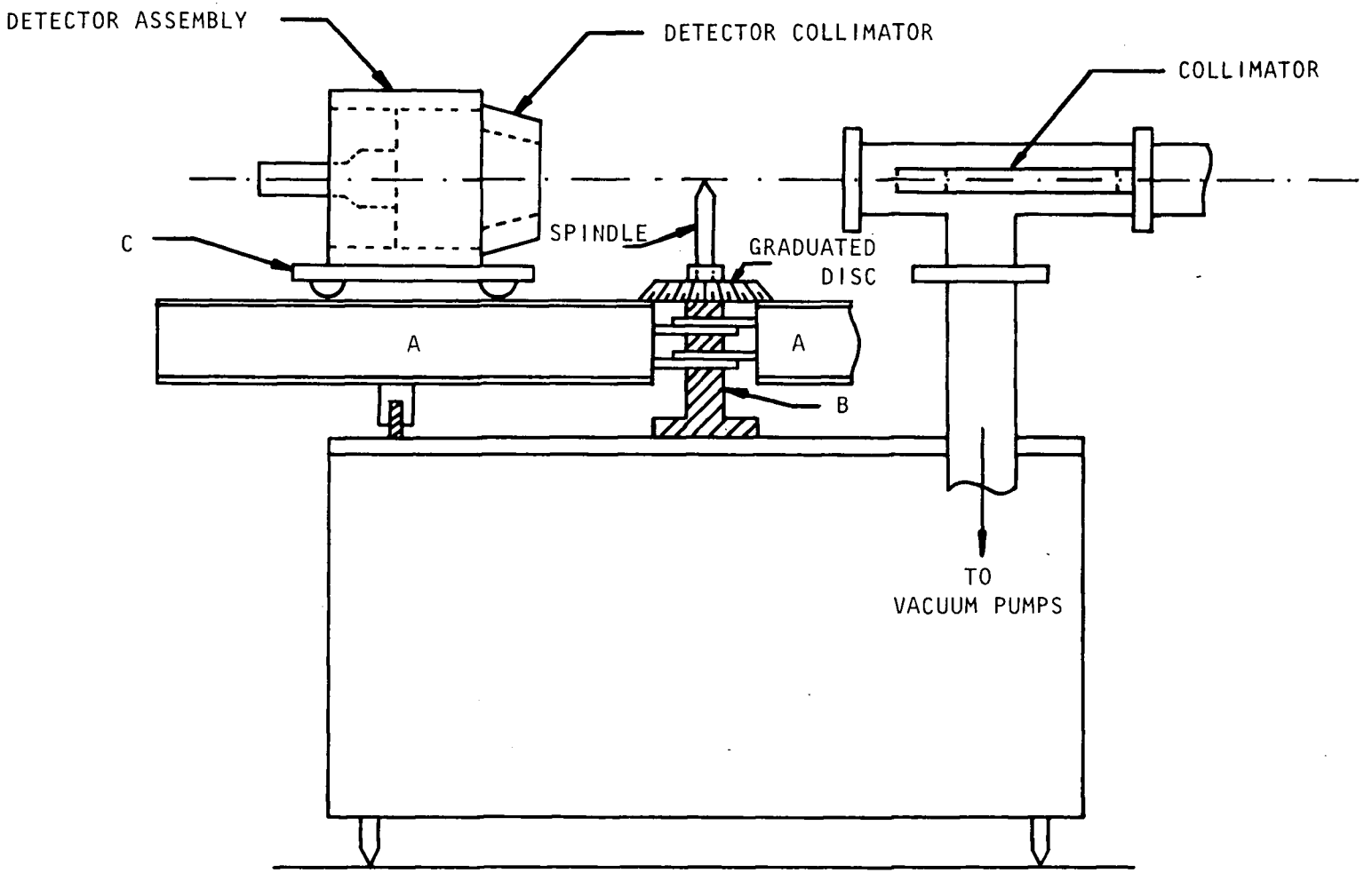

Fig. II-1 : Schematic diagram of the angular distribution table. Alignment of the detector and collimator with respect to the center of rotation is shown.

These axes were aligned to intersect at the tip of the spindle. The theodolite was also used to locate the degree disc so that the collimator axis passed through the zero degree mark. All adjustments are believed to have been made within one degree.

2.1.1. Target Chamber

The brass target chamber six inches high and three inches in diameter is shown in Fig. II-2. The 1/16 inch wall thickness was machined to a thickness of 0.021 inch over the centre region in order to reduce gamma-ray absorption. The bottom of the chamber was screwed through an insulator to a brass disc. The disc has a concentric cylindrical rod which fits in the centre post of the table, locating the target chamber on the detector rotation axis.

Two different target assemblies shown in Fig. II-3 were used in this experiment.

The target holder "TA" (used throughout the 160 KeV runs) consists of a copper plate, with 0.082 inch diameter holes drilled lengthwise through the copper every 0.10 inches, attached to a stainless steel rod by means of brass tubes. Cooling water flows through these tubes, and through the holes in the copper plate.

The target holder "TB" (used throughout the 90 KeV runs) consists of a solid 1/16 inch thick copper plate screwed to the water cooled copper tip of a stainless steel rod. In this case the copper plate can be displaced sideways. Both rods "TA" and

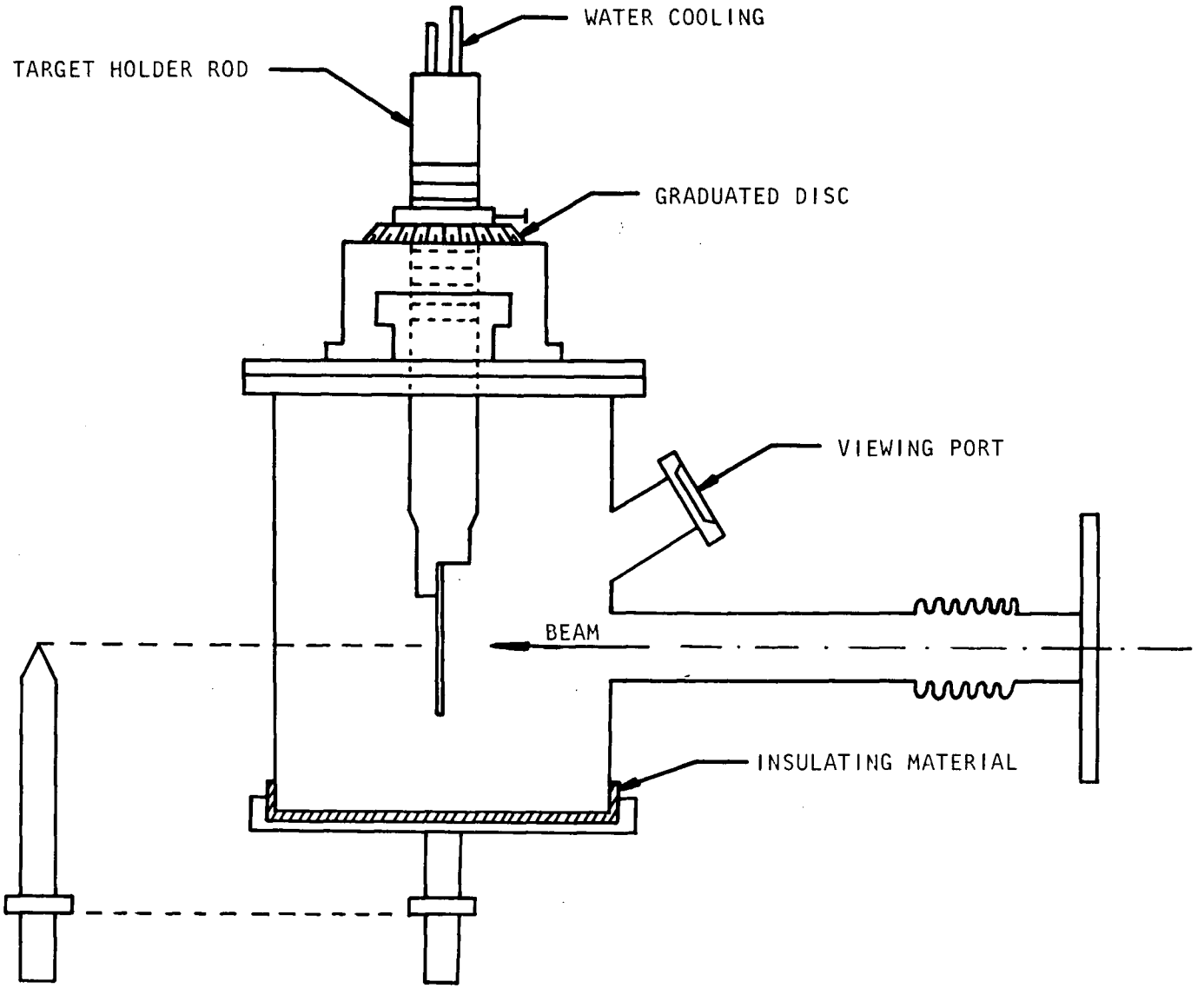

Fig. II-2 : Schematic diagram of the target chamber. The target chamber is located in the angular distribution table in place of the pointed spindle shown here for comparison.

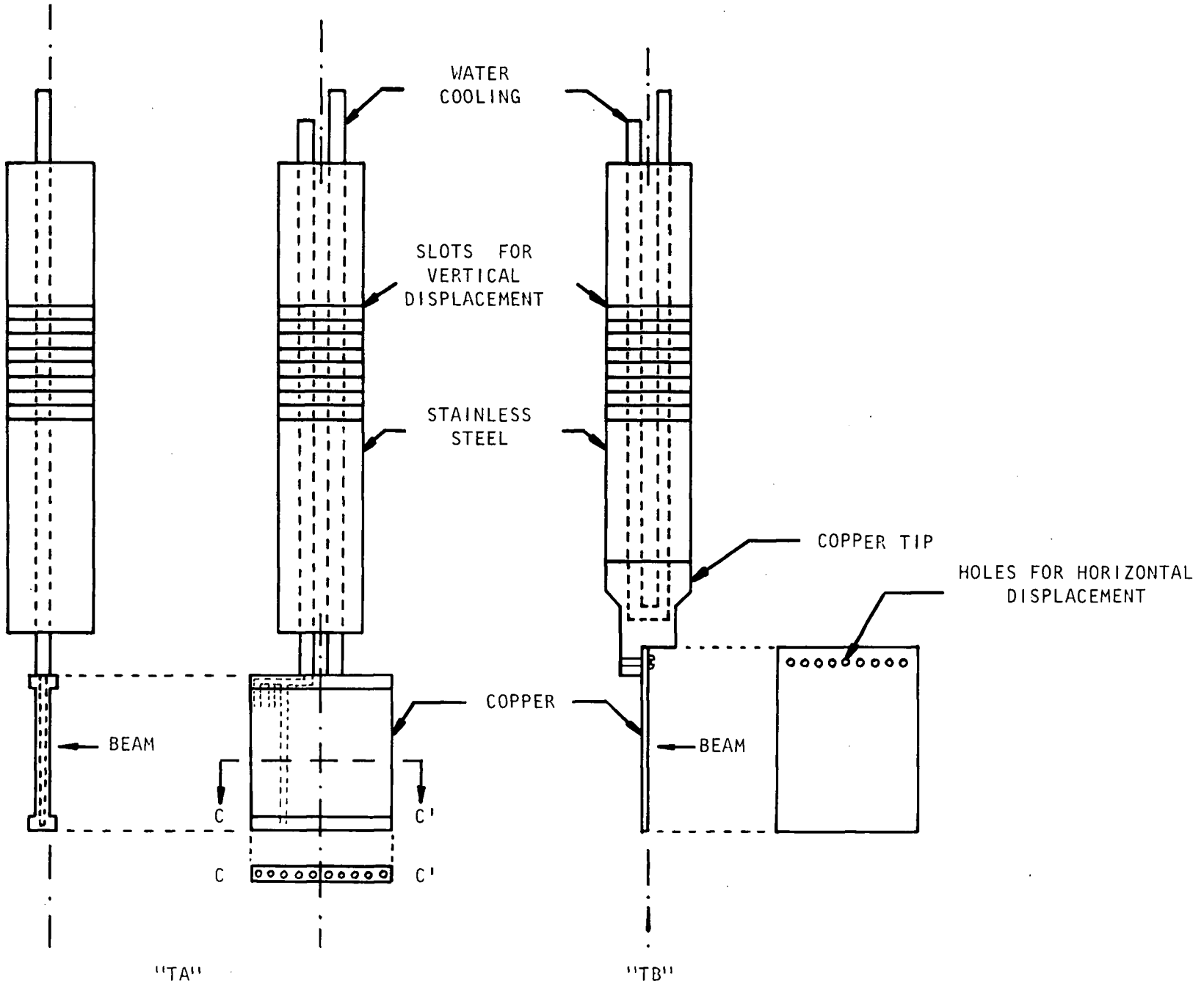

Fig. II-3 : Schematic diagram of the target holder rods.

"TB" have slots which allow the rods to be located in several different vertical positions. The "TA" target holder was originally made to be used with solid deuterated targets as for example deuterium occluded in zirconium since these targets need to be well cooled. The final 160 KeV runs were done using deuterated polyethylene targets and it was found that these targets could be adequately cooled by conduction through the copper backing. Therefore, the "TB" rod was adopted for the 90 KeV runs since it allows sideways displacement.

In both holders the targets, made on 0.012 inch copper backings, were clamped to the target holders. Once everything was assembled the face of the target remained in the plane containing the axis of the rod which is the same as the axis of rotation for the detectors.

2.1.2. The Collimator

The collimator consists of two defining apertures and a skimmer. The first two have defining holes 0.100 ± 0.005 inches in diameter and the second has a 0.120 ± 0.005 inch hole. The discs were mounted inside a machined stainless steel pipe and separated by two aluminium cylinders which are also used to conduct the heat to the supporting water cooled flange.

The whole assembly was electrically isolated from the beam pipe. Although the angular distribution measurements did not require knowledge of the charge collected by the target, (Chapter III), provisions were made for future measurements of

the absolute cross section. Fig. II-4 shows the potentials which will be applied to the target chamber and to the collimator for such measurements.

2.1.3. The Vacuum System

The angular distribution table has its own vacuum system so that the target chamber can be pumped independently of the accelerator vacuum system. It consists of a 100 l/sec (@ 10^{-5} mm of Hg) oil diffusion pump, a water cooled chevron ring baffle and a liquid nitrogen trap. DOW CORNING DC-705 oil was chosen because of its good backstreaming characteristics. To provide the fore-pressure a 30 l/min (@ 10^{-3} mm of Hg) mechanical pump is used.

The collimator, because of its small defining holes, isolates the vacuum in the target region from that of the accelerator. This arrangement should prevent dirt contamination in the accelerator region from depositing on the target. It also helps to maintain a good vacuum in the target area, thus reducing ionization due to the beam in the residual gas and making measurements of the total beam-charge collected in the target more reliable. With the beam "ON" the pressure in the target chamber, under normal operating conditions, averages approximately 9×10^{-7} mm of Hg. Fig. II-5 shows photographs of the angular distribution table and the detectors mounted on the trolleys.

2.2. <u>The Targets</u>

The choice of a suitable deuterium target was one of the main problems that had to be solved in order to measure the

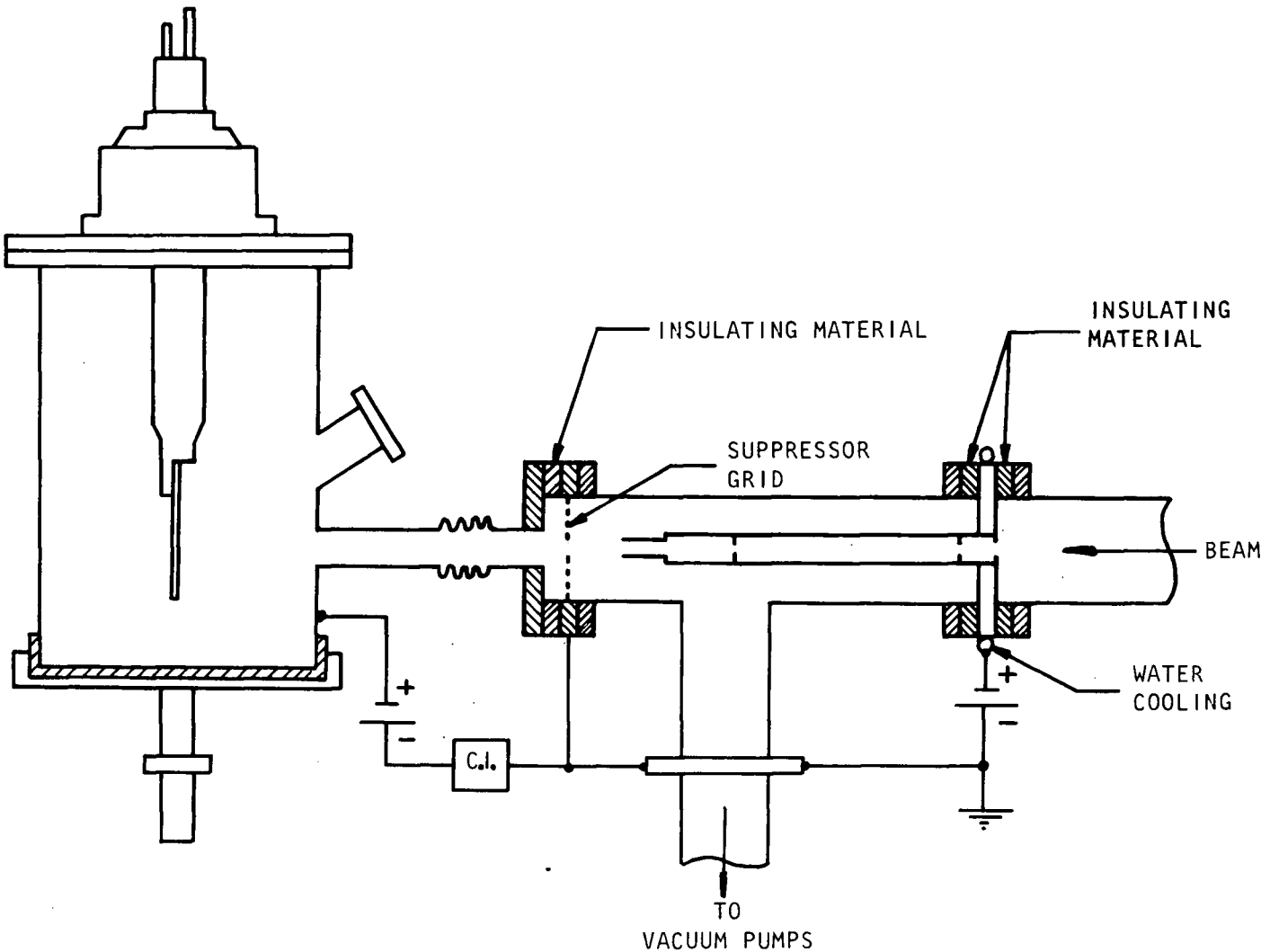

Fig. II-4 : Biasing voltage configuration and schematic diagram of the target chamber-collimator assembly.

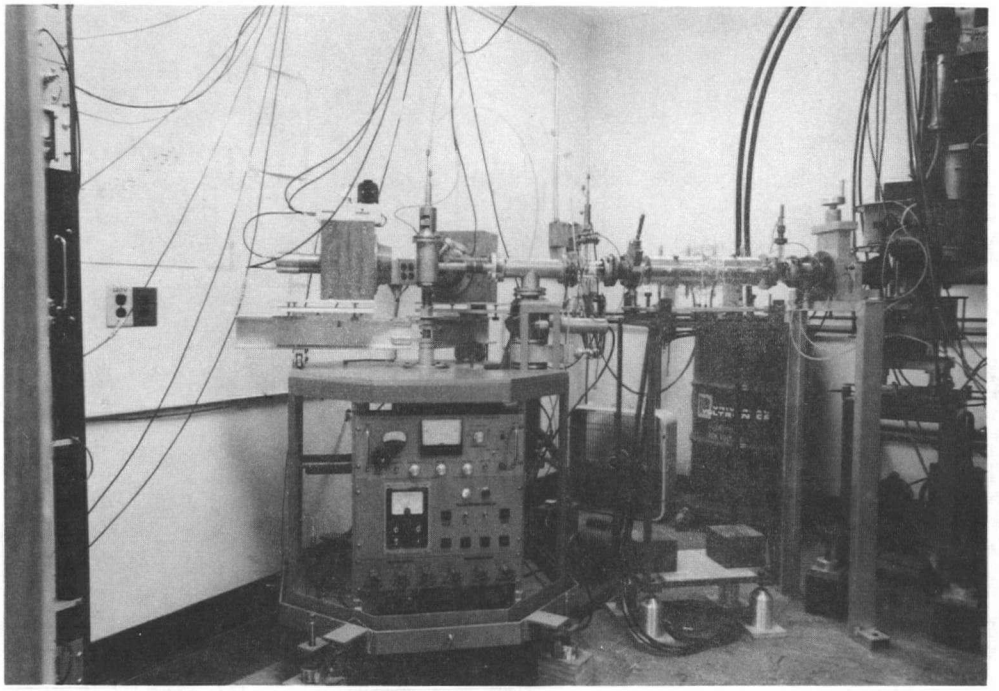

(a)

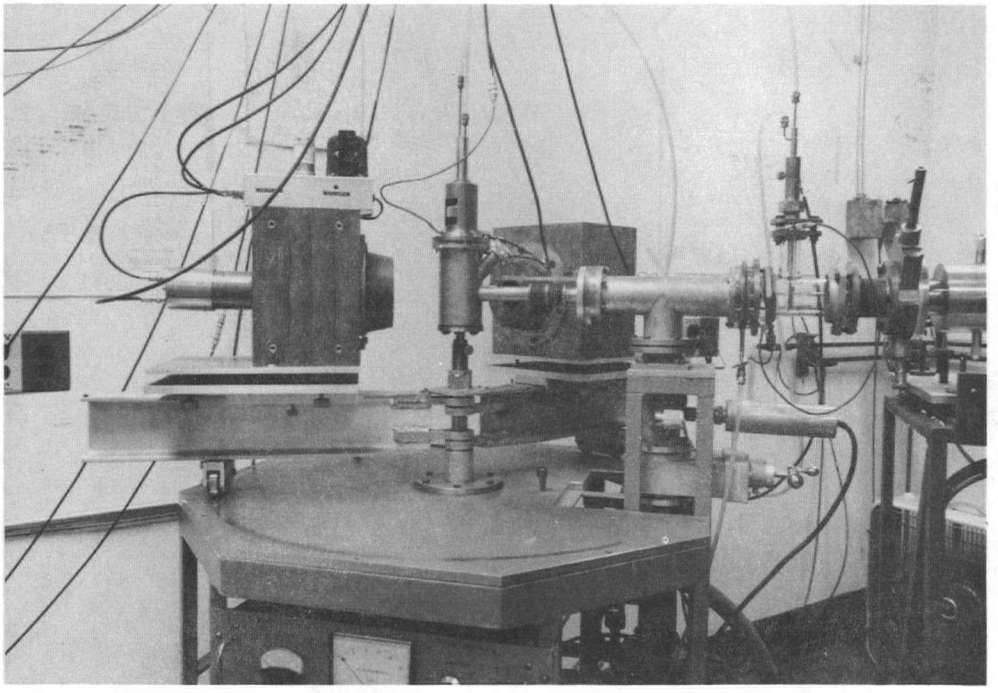

(b)

FIG. II–5 : (a) VIEW OF THE ANGULAR DISTRIBUTION TABLE AND AUXILIARY EQUIPMENT AND (b) CLOSE-UP VIEW OF THE ANGULAR DISTRIBUTION TABLE.

angular distribution to a higher accuracy than had been achieved in previous work.

It was difficult to find a target material that contained enough deuterium atoms to make it possible to observe the low cross section reaction in a reasonable time, which at the same time was rugged enough to withstand the large beam current and did not involve a large fractional energy loss for the low energy incident beam. On the basis of previous data (GR 62 ; GR 63) it can be estimated that for a bombarding energy of 160 KeV in the laboratory frame the cross section for the reaction considered here is about 0.08 μb for the isotropic component and 0.6 μb for the non-isotropic component.

The experiment requires a target with enough deuterium to provide a yield at least comparable to the background. Yet, the target must be thin enough so as to be able to discriminate between angular distribution measurements at 90 KeV and 160 KeV. A target thickness was chosen so as to produce a maximum energy loss of 35 KeV for 160 KeV protons. It is also desirable to have a beam spot on the target as small as possible in order to avoid solid angle corrections, due to the finite size of the source. At the same time it is desirable to be able to work with as much beam current as possible, in order to shorten the length of the runs and to keep the yield higher than the background.

Multiple scattering of the incoming beam in the target was also considered. The R.M.S. scattering angle should be kept

as small as possible, otherwise the angular distribution becomes difficult to analyze, particularly because no reliable theoretical analysis or experimental data is available on multiple scattering for massive charged particles for the low energies considered here. Deuterium targets can be classified into four different kinds: deuterium gas, heavy ice, deuterium absorbed in solid elements, and deuterated compounds.

2.2.1. Deuterium Gas Targets

Gas targets were discarded because no physical window was available that would hold a reasonable pressure of gas and admit a small diameter beam of the required current (about 100 μA). Differentially pumped gas targets were also impractical for this experiment, for apart from the very large gas flow required, the gamma-ray source could not be accurately defined in position.

2.2.2. Heavy Ice Targets

The main difficulty with these targets is that they would evaporate quickly under bombardment by the beam densities needed for this work. Further, the determination of the thickness is difficult. Previous low energy work with heavy ice targets was done with thick targets that completely stopped the beam. It should be pointed out here that for angular distribution measurements one does not need to know exactly the amount of target material as long as its thickness is kept below a certain value. An estimate of the thickness could be made by letting the vapor from a heavy water dispenser condense on a ^{11}B target attached to a liquid nitrogen cooled copper plate. The shift in

the 163 KeV resonance, in the reaction $^{11}B(p,\gamma)^{12}C$, would give direct evidence of the thickness of the heavy ice target. However, this is difficult to do, because the boron in the beam spot tends to flake off, thus making a bad thermal contact between the ice and the copper plate. Some tests were done using "thin" targets. A 100 KeV proton beam of 30 μA was collimated to give a target spot of 40 mm^2 on a thin heavy ice layer laid onto a liquid air cooled plate. The targets under these conditions did not last longer than a few seconds and so this method was discarded.

2.2.3. Deuterium Absorbed in Solid Elements

Some elements have the property of absorbing and retaining large quantities of hydrogen at relatively high temperature. Among those which absorb the most are palladium, tantalum, zirconium, and titanium. It was recently found that erbium and in general most of the rare earth elements are also good absorbers. Deuterium targets of this kind have been used for many years for neutron production. It is essential that the gas once absorbed is retained in the target while under bombardment by a beam in a vacuum. Targets of deuterium in Zr and Ti were obtained from the Oak Ridge National Laboratory. They were made as follows:
A known amount of, say, zirconium was evaporated onto a suitable, and previously outgassed backing such as copper, platinum or tungsten. The deposit was outgassed under vacuum at high temperatures and placed in a deuterium atmosphere at a suitable temperature. Absorption begins after the heat is interrupted and the

system is allowed to cool off. Angular distribution measurements at a proton energy of 160 KeV were done using Zr-D targets ranging from 80 $\mu g/cm^2$ to 143 $\mu g/cm^2$ and Ti-D targets ranging from 47 $\mu g/cm^2$ to 58 $\mu g/cm^2$. The results contained uncertainties arising from the rather large angular spread of the incoming particles in the target, due to the multiple coulomb scattering. Thinner targets would have overcome this difficulty however they would have given too low a gamma-ray yield.

2.2.4. The Deuterated Compounds

There are several hundred commercially available deuterated compounds. Most of these compounds are, however, in gaseous or liquid form or they have two or more different elements, besides deuterium in their molecular structure.

A simple compound is deuterated polyethylene $(CD_2)_n$. Using this compound as a target the R.M.S. multiple scattering angle is reduced considerably, compared with the Zr-D and Ti-D due to the lower Z in the target components. Although the $^{12}C(p,\gamma)^{13}N$ and $^{13}C(p,\gamma)^{14}N$ reactions compete with $D(p,\gamma)^3He$, the first produces gamma-rays of lower energy which can be eliminated by a high enough discrimination level and the second has a negligible yield. Both reactions are discussed in Appendix F.

Self-supporting deuterated polyethylene targets are being used satisfactorily in this laboratory (TR 67 ; MC 68). These targets, however, can withstand only small beam densities at most of the order of 10 $\mu A/cm^2$. Furthermore, if an energy loss

in the target of only 35 KeV for a 160 KeV incident proton beam is required, the polyethylene layer will be, physically, extremely thin and thus very difficult to handle. Consequently such targets were ruled out.

It was found that if the polyethylene is deposited on a metal backing, the target so formed, can withstand large beam currents of the order of 200 to 300 $\mu A/cm^2$, without rapid loss of target material. Furthermore, thin targets (of the order of 30 KeV for incident protons of 160 KeV) could easily be made in this way. Therefore, these targets were utilized for the angular distribution measurements of the $D(p,\gamma)^3He$ reaction. The technique followed in the preparation of the targets is described in Appendix D. A comparison between these targets and Zr-D targets, normalized to the same deuterium content is also shown.

The targets used throughout this experiment were prepared by depositing 364 $\mu g \pm 10\%$ and $364/\cos 45^\circ = 515\ \mu g \pm 10\%$ of polyethylene on a 3.7 cm by 3.7 cm copper plate 0.03 cm thick. Both targets are equivalent because of the two different detector-target configurations used in performing the angular distribution measurements, (Chapter III), so that only one will be considered here. The 515 μg when deposited on 13.69 cm^2 gives a target thickness ρt (CD_2) of 37.60 $\mu g/cm^2$. This corresponds to $N_C t = 1.416 \times 10^{18}$ carbon atoms/cm^2 and $N_D t = 2.832 \times 10^{18}$ deuterium atoms/cm^2. The characteristics of this target are shown in Table II-1.

Table II-1 : Characteristics of the Deuterated Polyethylene Targets.

E_p (KeV)	$[\theta]_{E_p}$	ε_C (10^{-15} eV-cm^2)	ε_D (10^{-15} eV-cm^2)	ΔE (KeV)	$[\theta]_{\bar{E}_p}$	$\bar{E}_p$ (KeV)
160	1° 10'	14	4.5	32.6 ± 3.3	1° 18'	144
90	2° 6'	16	6	39.7 ± 4.0	2° 43'	70

E_p is the incident proton energy; ε_C and ε_D the stopping cross section for protons in carbon and deuterium, respectively; ΔE the energy lost by the beam in the target and $[\theta]_{E_p} = \sqrt{\langle\theta^2\rangle_{E_p}}$ and $[\theta]_{\bar{E}_p}$ are the R.M.S. multiple scattering angle for protons of energies E_p and $\bar{E}_p = E_p - \Delta E/2$ respectively.

The energy loss was calculated, (using the following expression), assuming the stopping cross sections remained the same as the beam traversed the target:

$$\Delta E = \varepsilon_C N_C t + \varepsilon_D N_D t$$

The values for the stopping cross sections were obtained from Whaling (WH 58). The stopping cross section for protons on carbon reaches its maximum at about 90 KeV, while the maximum for protons on deuterium occurs at 50 KeV with a value of 6.6×10^{-15} eV-cm^2. Therefore, if the variation of the stopping cross section with energy were taken into account the energy loss in the target will be at the most 4.5% higher than the value 39.7 KeV given in Table II-1. At 90 KeV the energy loss is somewhat higher than the

35 KeV referred to previously as the maximum. The targets were made thicker than 35 KeV to compensate for the loss of deuterium which occurs when the beam initially hits the target. (See Appendix D). From the observed initial decrease in the gamma-ray yield, which is attributed to the loss of deuterium, it was estimated that these targets were thinner than 35 KeV throughout most of their run. The same effect applies for the targets used at 160 KeV.

Multiple scattering calculations are discussed in Appendix E, so only the basic idea is introduced here. Assume that a parallel beam is incident on a target. The angular distribution of the particles emerging from the target will clearly have cylindrical symmetry around the axis defined by the incident beam. Based on statistical considerations (SE 53) which are in agreement with the experimental results obtained from the scattering of fast electrons (WI 39) one can expect the particles to be Gaussian distributed around this axis. Thus statistically after traversing a certain thickness of target 68% of the incident particles lie in a region defined by a cone whose half-angle, with respect to that axis, is called the R.M.S. multiple scattering angle. The results of the calculation discussed in Appendix E are shown in Table II-1. Because of the small multiple scattering angle produced by this target, its smearing effect in the angular distribution of the gamma-rays was negligible.

2.3. The Detector, Collimator and Shielding

The gamma-ray detector (HARSHAW Type 20MBS16/B) consists of a 5 inch diameter by 4 inch deep cylindrical NaI(Tl) crystal

coupled to a 3 inch (RCA 8054) photomultiplier. Two identical detectors mounted in identical lead shields and collimators were used in this experiment. A schematic drawing is shown in Fig. II-6.

The Detector Half-Angle β: The angular distribution of the gamma-rays from the reaction $D(p,\gamma)^3He$ can be expressed approximately by $W(\theta) = a + b \sin^2\theta$ (Chapter I). Because a is small compared to b, β was chosen so that when the detector was placed at 0° most of the gamma radiation in the solid angle subtended by the counter arose from the isotropic component.

The total cross section is expressed by $\sigma = \sigma_a + \sigma_b$ where σ_a and σ_b are the total cross section for the isotropic and non-isotropic components respectively. Thus

$$\sigma = \int_\Omega \frac{d\sigma}{d\Omega} d\Omega = \frac{3}{8\pi} \sigma_b \int_\Omega \sin^2\theta \, d\Omega + \frac{1}{4\pi} \sigma_a \int_\Omega d\Omega$$

Thus the above condition is given by

$$\sigma_a \int_0^\beta \sin\theta \, d\theta \quad >> \quad 3 \sigma_b \int_0^\beta \sin^3\theta \, d\theta$$

For $\beta = 12^\circ$ and $\sigma_a/\sigma_b = 0.13$ the isotropic component contribution amounts to 80.4% when the detector is at 0°.

The Source Distance R: The distance R was chosen such that the cone defined by β contains the back of the crystal. That is

$$S + P = \frac{D}{2 \tan\beta} - L$$

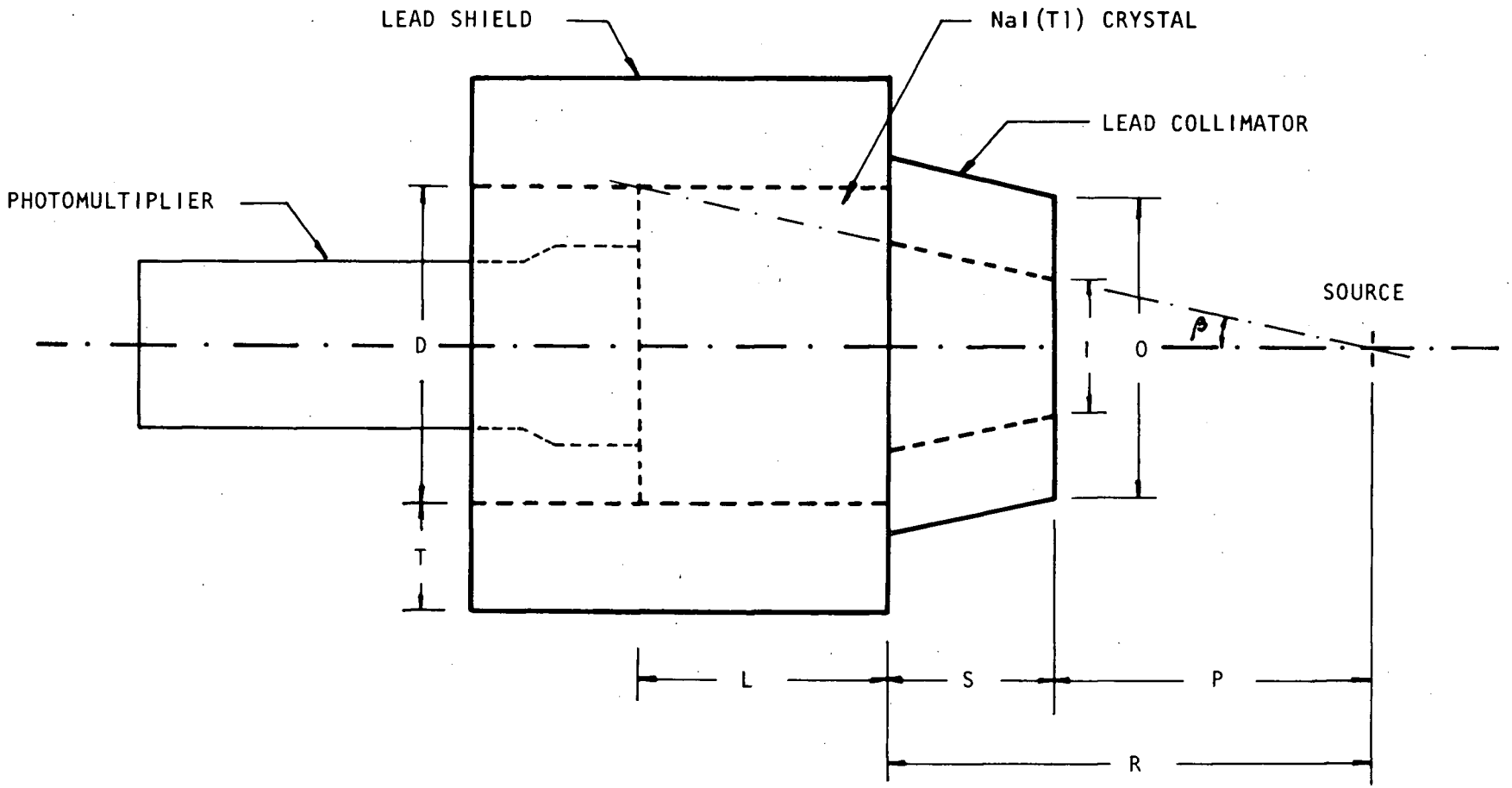

Fig. II-6 : A schematic diagram of the detector assembly. The dimensions are given in Table II-2

A tapered collimator was placed in front of the crystal. In this way a half-angle of 12^{o} was defined and the corners of the crystal remained shielded. This collimator has the following results:

1. The background counting rate is reduced, since the crystal "looks" only at the source.
2. The edge effects of the crystal are reduced with two useful consequences:
   a. It improves the photopeak to tail ratio. Thus the ratio of information to background is improved. Fig. II-7 shows the effect of the collimator on the shape of the spectra obtained using a ^{60}Co source. The spectra were normalized to equal kicksorter live times of 40 minutes. The background was not substracted. Without the collimator the photopeak is higher than with it because the detector subtends a larger solid angle.
   b. The angular distribution measurements have to be corrected for the effect of the finite solid angle of the detector (RO 53). As a result of reducing the edge effects the estimation of the correction factors, usually referred to as smoothing factors, is made more reliable. This involves the evaluation of integrals of the form:

$$J_\ell = \int_0^\beta P_\ell(\cos\xi)\left(1 - e^{-\sigma x(\xi)}\right)\sin\xi \, d\xi$$

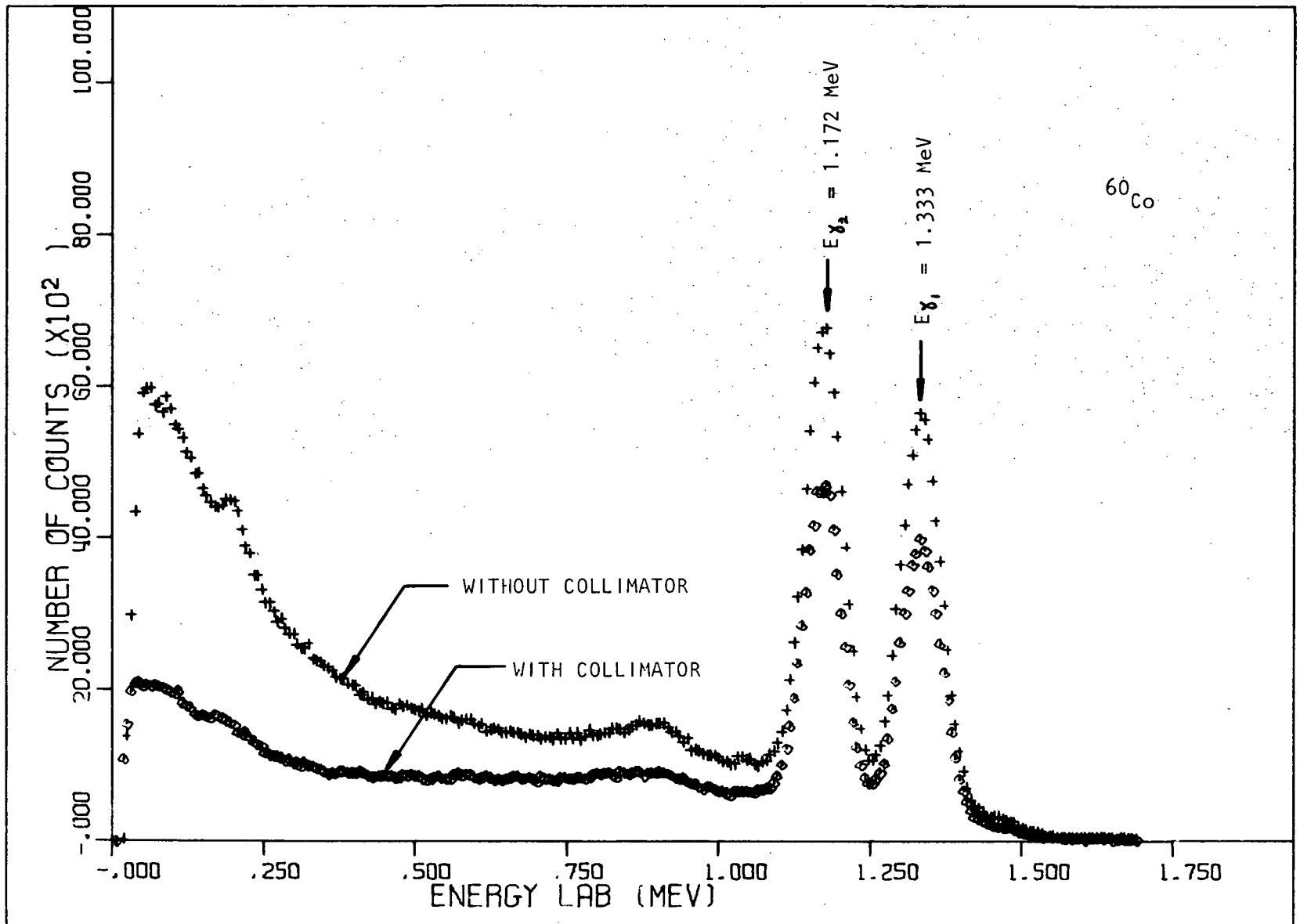

Fig. II-7 : ^{60}Co gamma-ray spectra taken with and without the detector collimator

where μ is the linear attenuation coefficient, $x(\xi)$ is the distance traversed by the radiation incident on the crystal at an angle ξ with respects to its axis, and P_l are the Legendre polynomials of order l. The smoothing factors are defined by $Q_l = J_l/J_o$. Without the collimators the above integration over the crystal volume becomes less reliable for two reasons. First there will be a larger number of gamma-rays scattered into the crystal from surrounding materials, and second a larger number of gamma-rays will interact near the edges of the crystal where the probability of secondary radiation and electrons escaping from the crystal is much higher. Since the gamma-ray intensity is obtained by integrating the spectrum upwards from approximately half the full energy, many of these events will not be counted.

The Collimator Thickness S: The gamma-ray intensity at the corners of the crystal depends on the thickness S of the collimator. For S = 6.5 cm the attenuation factor was found to be equal to 0.041 for 5.58 MeV gamma-rays in lead.

Finally we have to consider the contribution of those gamma-rays which are scattered towards the crystal by the front edge of the collimator. A rough estimate was made of the number

of gamma-rays that leave the source at an angle greater than the half-angle β of the collimator and scatter into the crystal from the edge of the collimator with the detector at 0°. Only Compton scattering is relevant to this estimate and since the final gamma-ray intensity is based on the number of counts in the spectrum between 2.95 MeV and 6.1 MeV, only those gamma-rays scattered with energies greater than 2.95 MeV need be considered. This corresponds to scattering through angles less than 23°. It was assumed that all the electrons in a layer of collimator one half radiation length thick were located in a ring at the inner front part of the collimator and that the gamma-rays that entered the front of the collimator were scattered by these electrons. If one half of the gamma-rays scattered between 0° and 23° entered the crystal then the collimator scattering could contribute at most 0.8% of the total number of gamma-rays that enter the crystal.

The size of this crystal is considered to be optimum. A smaller crystal is undesirable because for the same solid angle and collimator shape the detector must be placed closer to the source with the result that:

a. the size of the source becomes critical
b. the scattering at the edge of the front collimator increases
c. variations in the source to crystal distance are more critical.

A bigger crystal is also undesirable in the spite of

the advantage of a decreased edge effect for the same solid angle, because of the increase in the background and increase in the neutron induced activity which may be present for some bombarding energies. In general crystals longer than one or two radiation lengths are undesirable, because the back part has a low gamma-ray flux but contributes background counts roughly proportional to its volume. For 5.5 MeV gamma-rays in NaI the radiation length is approximately 8 cm.

Neutrons may arise from the reaction $D(d,n)^3He$ caused by deuterons in the target which have picked up energy by collisions with incident protons (GR 55). The neutrons are not counted directly by the crystal but they are captured by ^{127}I which results in the prompt emission of gamma-rays in the energy range from 2 to 6 MeV. This is followed by β^- emission of 2.02 MeV or 1.59 MeV followed by gamma-rays of 0.428 MeV. The beta decay transitions do not, however, interfere with the $D(p,\gamma)^3He$ spectrum since they are below the 2.95 MeV integration bias level. Table II-2 shows the exact dimensions of the detector assembly.

2.4. The Electronics

A block diagram of the electronics used in the experiment is shown in Fig. II-8. A list of the electronic units used is given in Table II-3. The output from the photomultipliers were sent to two identical preamplifiers with 50 Ω output impedance. The photomultiplier and preamplifier circuit diagrams are shown in Fig. II-9 and II-10. The phototubes were operated

Table II-2 : Dimensions of the Detector Assembly #1 and #2

Collimator Half-Angle	β	12.0 ± 0.2	degrees
Source to Crystal Face	R	19.52 ± 0.05	cm
Source to Collimator Face	P	12.46 ± 0.05	cm
Collimator Thickness	S	6.54 ± 0.05	cm
Crystal Diameter	D	12.70 ± 0.02	cm
Crystal Thickness	L	10.16 ± 0.02	cm
Collimator Face Inner Diameter	I	5.30 ± 0.05	cm
Collimator Face Outer Diameter	O	11.6 ± 0.1	cm
Thickness of Lead Shielding	T	4.0	cm

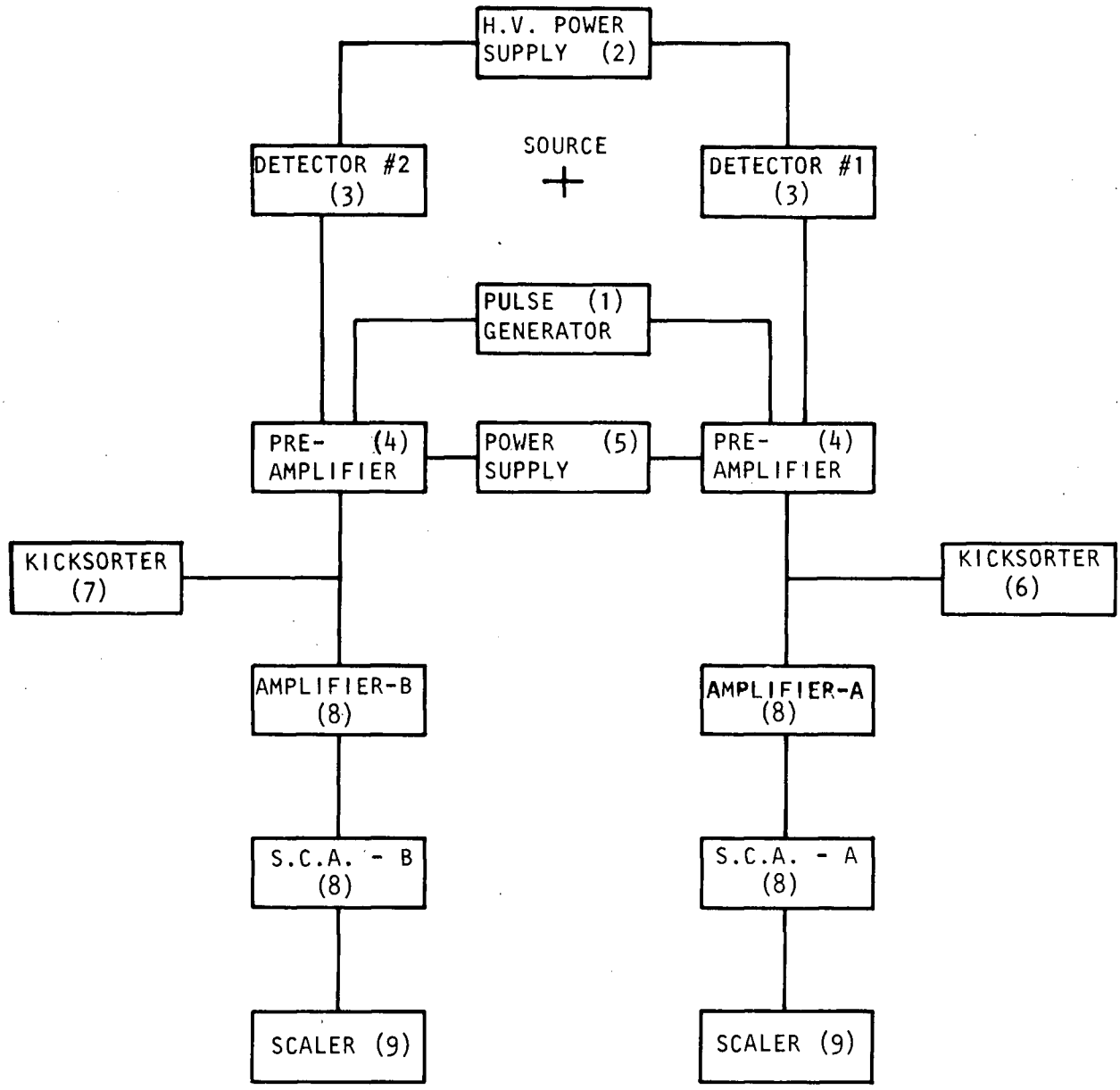

Fig. II-8 : Block diagram of the electronic arrangement. The units are listed in Table II-3.

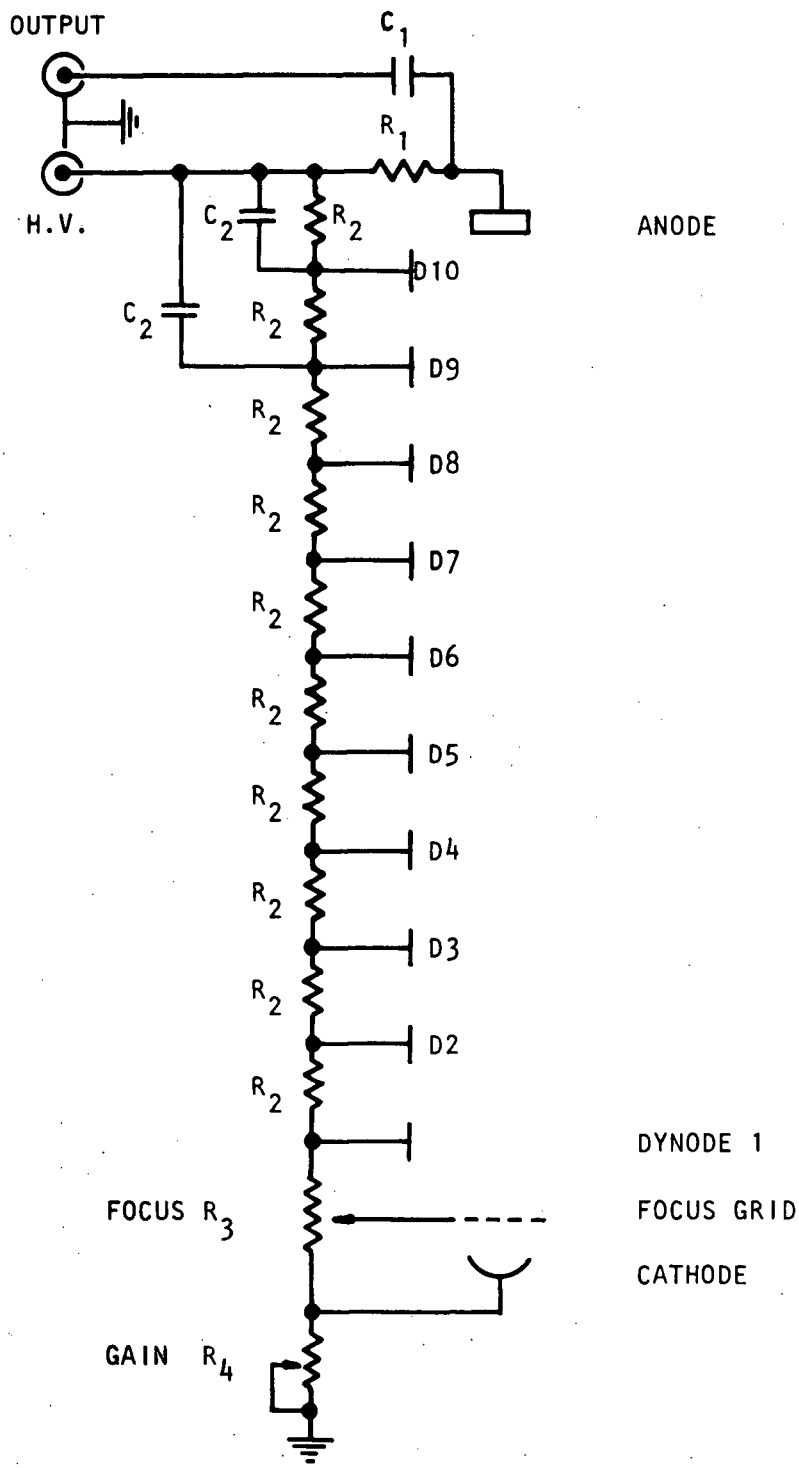

RCA 8054	
R_1	100 K ½W 5%
R_2	470 K ½W 5%
R_3	1.5 M Pot.
R_4	2 M Pot.
C_1	0.001 µF 3 KV
C_2	0.01 µF 600 V

Fig. II-9 : Photomultiplier circuit

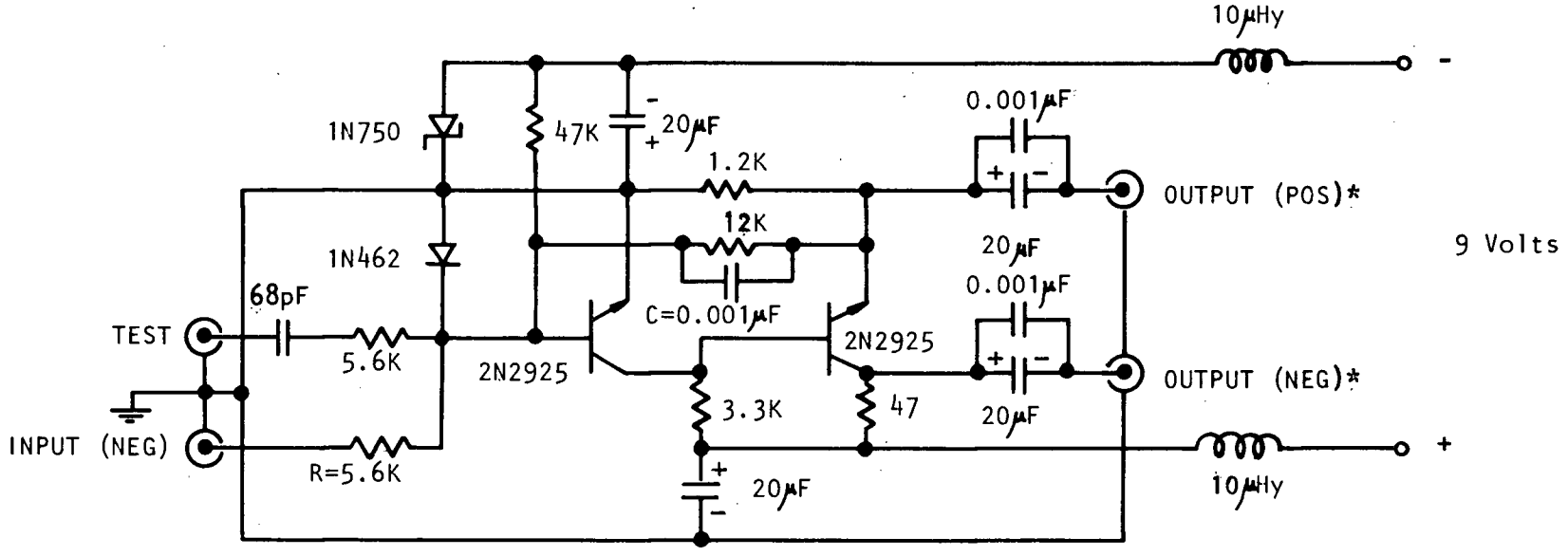

Fig. II-10 : Pre-amplifier circuit. * For negative pulse output the positive output must be grounded (and vice-versa)

at 1100 Volts and the focus control was adjusted to obtain the best resolution. The measured pulse height resolution for 662 KeV gamma-rays was found to be 7.4% for detector #1 and 7.8% for detector #2.

The shape of the pulses at the output of the preamplifiers was adjusted by means of the resistor R and capacitor C to satisfy the low level input requirements of the ND-160 and ND-120 kicksorters. The 2.614 MeV pulses, from a RaTh source, across a 50 Ω resistor connected at the output of the preamplifier (with R = 5.6 KΩ and C = 0,001 μF) have a rise-time of 0.6 μs and a fall-time of 18 μs.

The pulse remains at nearly its maximum voltage level for approximately 0.5 μs with the maximum occuring at 1.2 μs, from the start. The preamplifiers have a voltage gain of approximately 0.08. They were built from a circuit designed by G. Jones (JO 65). A power supply was built to supply d.c. power to both preamplifiers. The circuit diagram is shown in Fig. II-11.

The signals from the preamplifiers besides going to the kicksorters were also sent to two identical scalers through a dual linear amplifier - single channel analyzer system. An initial estimate of the angular distribution could then be obtained while the experiment was under way. An estimate of the rate of deterioration of the targets could also be obtained in this way.

The electronic system was checked for linearity using

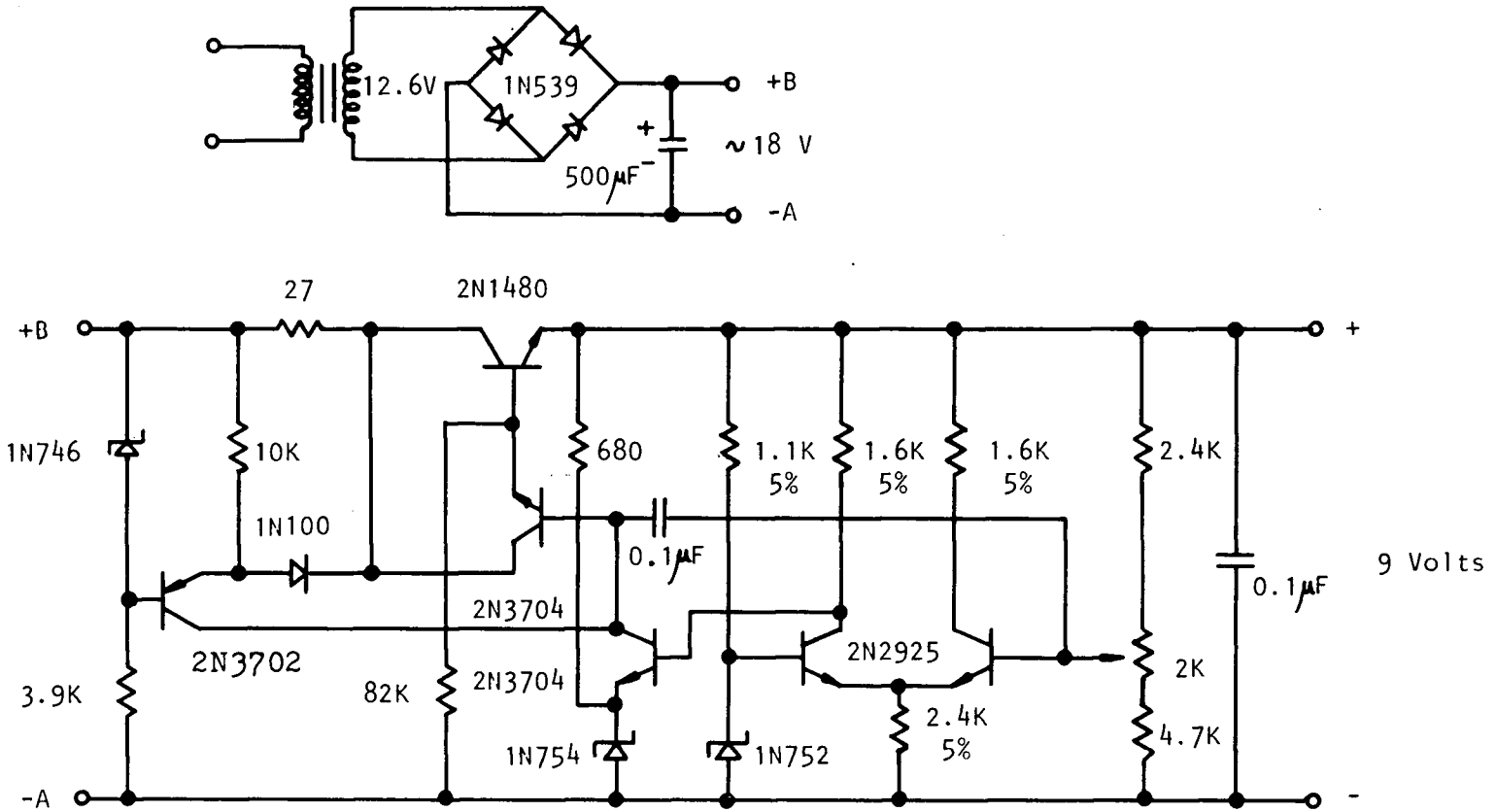

Fig. II-11 : Pre-amplifier's regulated power supply circuit.

a pulse generator. It was built using a mercury switch driven at 60 Hz. The circuit, shown in Fig. II-12, was designed to give a pulse whose shape after the 68 pF capacitor (test input of the preamplifier) was identical to the one produced by the detector at the input of the preamplifier. The linearity of the HELIPOT potentiometer was checked using a FLUKE differential voltmeter, and it was calibrated in energy units using standard radioactive sources. The pulse generator was also used to make periodic checks of the windows of the single channel analyzers.

Table II-3 : List of the Electronic Units used in this Experiment.

1. U.B.C. Pulse generator. Circuit diagram Fig. II-12.
2. FLUKE Model 412-B High Voltage Power Supply.
3. HARSHAW Type 20MBS16/B. Detector Assembly NaI(Tl) 5" x 4" crystal coupled to an RCA 8054 3 inch photomultiplier. Circuit diagram Fig. II-9.
4. U.B.C. Preamplifier. Circuit diagram Fig. II-10.
5. U.B.C. Power Supply. Circuit diagram Fig. II-11.
6. NUCLEAR DATA ND-160 Dual Parameter Analyzer.
7. NUCLEAR DATA ND-120 Pulse Height Analyzer.
8. NUCLEAR DATA ND-500 Dual Amplifier and Single Channel Analyzer.
9. ORTEC Model 430 Scaler.

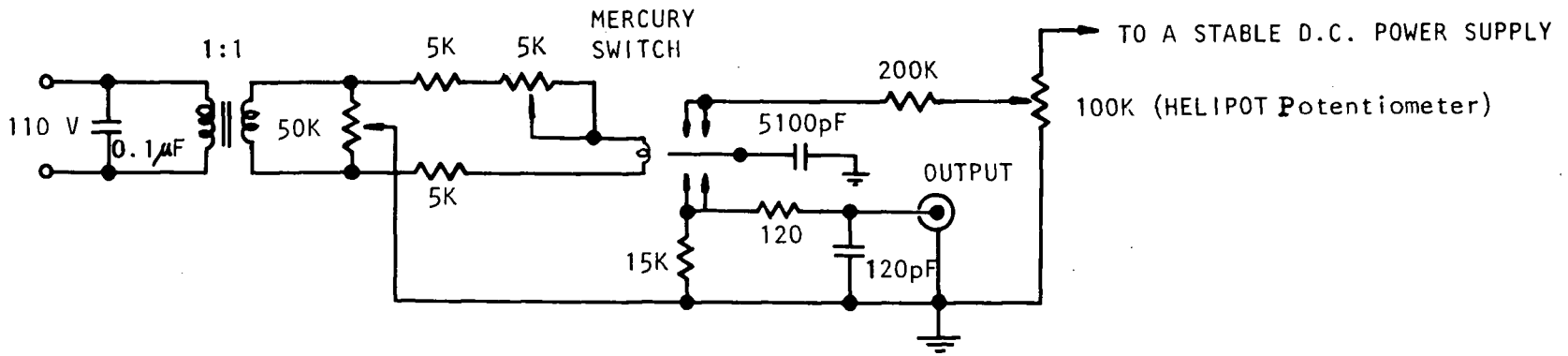

Fig. II-12 : Pulse generator circuit.
Negative pulse output: r.t.= 80 ns , f.t.=350 μs.

CHAPTER III

EXPERIMENTAL METHODS AND RESULTS.

The technical problems involved in the measurements and the apparatus parameters chosen are discussed in the previous chapter. In the present chapter the measurements and methods of data analysis are described.

3.1. Procedure

Since a number of different targets were used and the targets tended to deteriorate during bombardment it was not possible to relate one run to another in terms of the integrated charge delivered to the target. Individual runs were therefore normalized in terms of the counts recorded by monitor counter #2 placed at a fixed angle. For all runs the beam spot on the target was 4 mm in diameter which is sufficiently small compared to the 19.5 cm distance from the target to the detector so that the target can be considered as a point source of gamma-rays.

The targets were laid down on a 3.7 cm x 3.7 cm copper backing and the average number of runs made on each target was 72. Due to the deterioration of the target when subjected to a beam of 80 to 90 μA the beam was kept on the same target spot for approximately five minutes, and then moved to a new spot.

Two detector-target configurations shown in Fig. III-1 were used for the angular distribution measurements. For configuration "A" the target plane was placed at 90^{o} to the incident

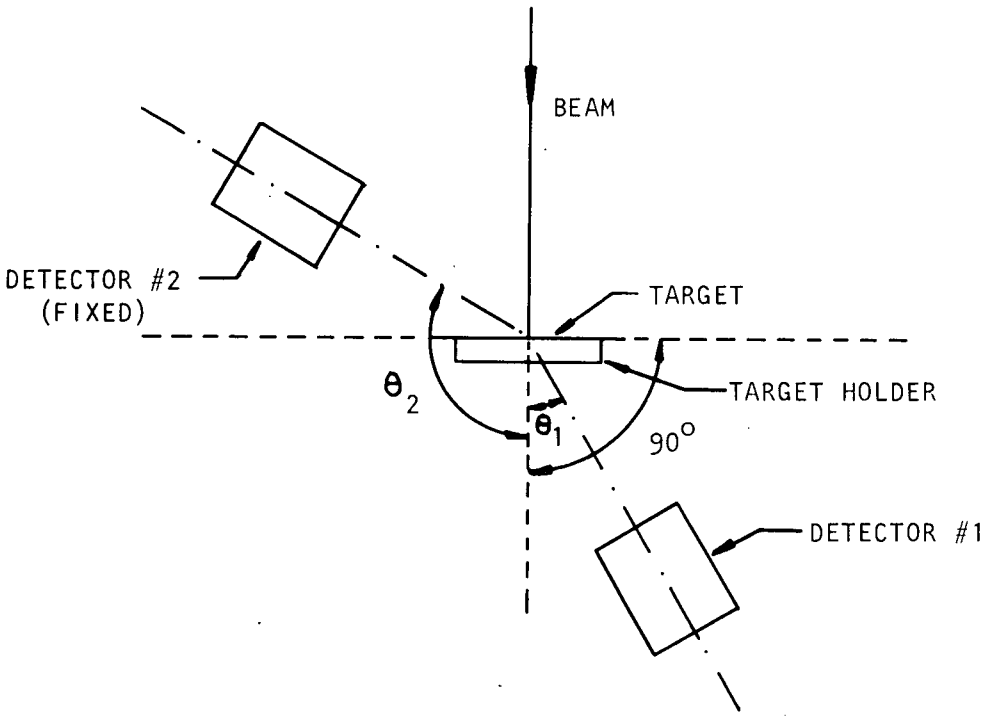

CONFIGURATION "A"

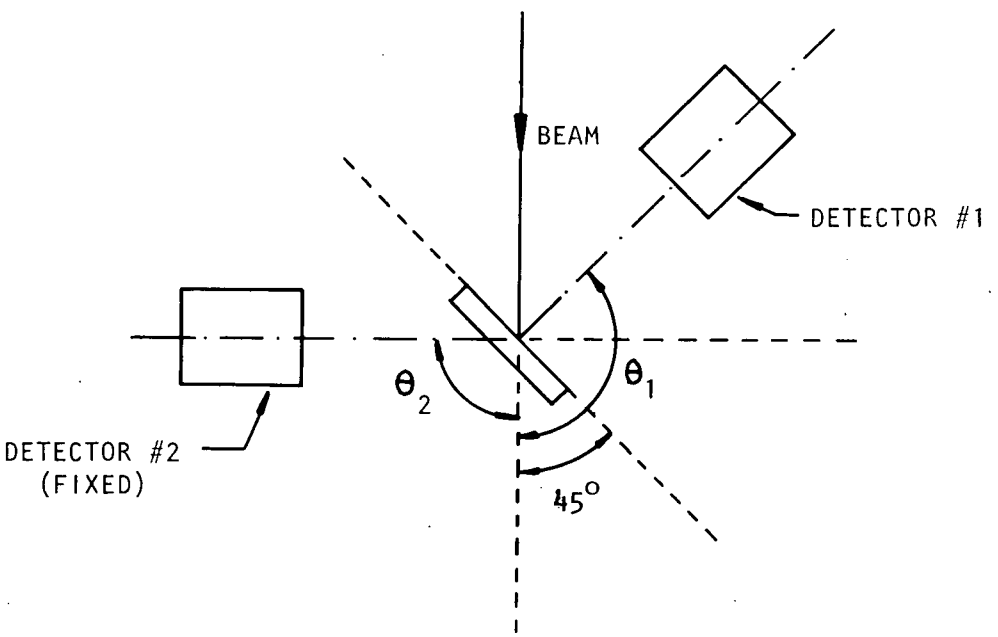

CONFIGURATION "B"

Fig. III-1 : Detector target configurations

beam while the fixed monitor was placed at -120°. Although a higher count would have been obtained with the monitor at 90° the target absorption at that angle would have been large and uncertain. For this geometry the moving detector angle θ_1 was varied from -30° to $+60^{\circ}$ where the minus sign corresponds to being on the same side of the beam axis as the monitor detector. For geometry "B" the target plane was at 45° to the beam and the monitor was at -90° so it observed gamma-rays coming through the target backing. The moving detector was rotated from 60° to 135° the maximum backward angle that could be reached with the apparatus used.

As mentioned in Chapter II, two different target thicknesses were used throughout this experiment. The target of configuration "A" was $1/\cos 45^{\circ}$ thicker than that of configuration "B" so that the beam passed through the same thickness of target material for both cases.

The spectra obtained from both multichannel analyzers were integrated from 2.95 MeV to 6.1 MeV, the lower limit being chosen to lie above the RaTh full energy photo peak, while the upper limit was chosen to lie above the peak corresponding to the maximum gamma-ray energy of 5.65 MeV expected from the reaction $D(p,\gamma)^3He$. Because the gain of the electronic system changed slightly over a long period of time, each spectrum was shifted to a standard gain and integrated using the IBM 7040/7044 computer. The final measurements at 90 KeV and 160 KeV took between seven and eight days to complete.

The energy calibration for each spectrum was obtained from the 2.614 and 1.462 MeV peaks from RaTh and ^{40}K which arise as part of the room background. The walls of the room contain significant amounts of RaTh and ^{40}K. Fig. III-2 shows a typical background run taken over a period of 69.5 hours. The background count above the 2.614 MeV peak arises principally from the μ-meson component of the cosmic rays. In the region of interest from 3 MeV to 6 MeV this counting rate averages 370 counts per hour per MeV. A typical gamma-ray spectrum from the reaction $D(p,\gamma)^3He$ is shown in Fig. III-3. It was taken for a bombarding energy of 160 KeV with the detector #1 placed at $\theta = 90^\circ$. The total charge delivered to the target was approximately 300 mC. (A spectrum taken at 0° is shown in Fig. H-2 (Appendix H); here the total charge delivered was approximately 420 mC). The spectra obtained from detector #1 with the ND-160 kicksorter were put on paper tape and transferred to the computing centre where they were converted to magnetic tape and punched on IBM cards. The monitor spectra collected by the ND-120 kicksorter were printed out and manually punched on IBM cards. The gain shifts and integrations were then carried out on the computer.

The angular distribution results are shown in Table III-1 for the 90 KeV run and in Table III-2 for the 160 KeV run. A and B are the integrated number of counts including the background from detectors #1 and #2 respectively. θ_1 and θ_2 are the angular positions of detectors #1 and #2 as shown in Fig. III-1. The first row (i=0) shows the integrated number of counts due to the background taken when the machine was not in operation.

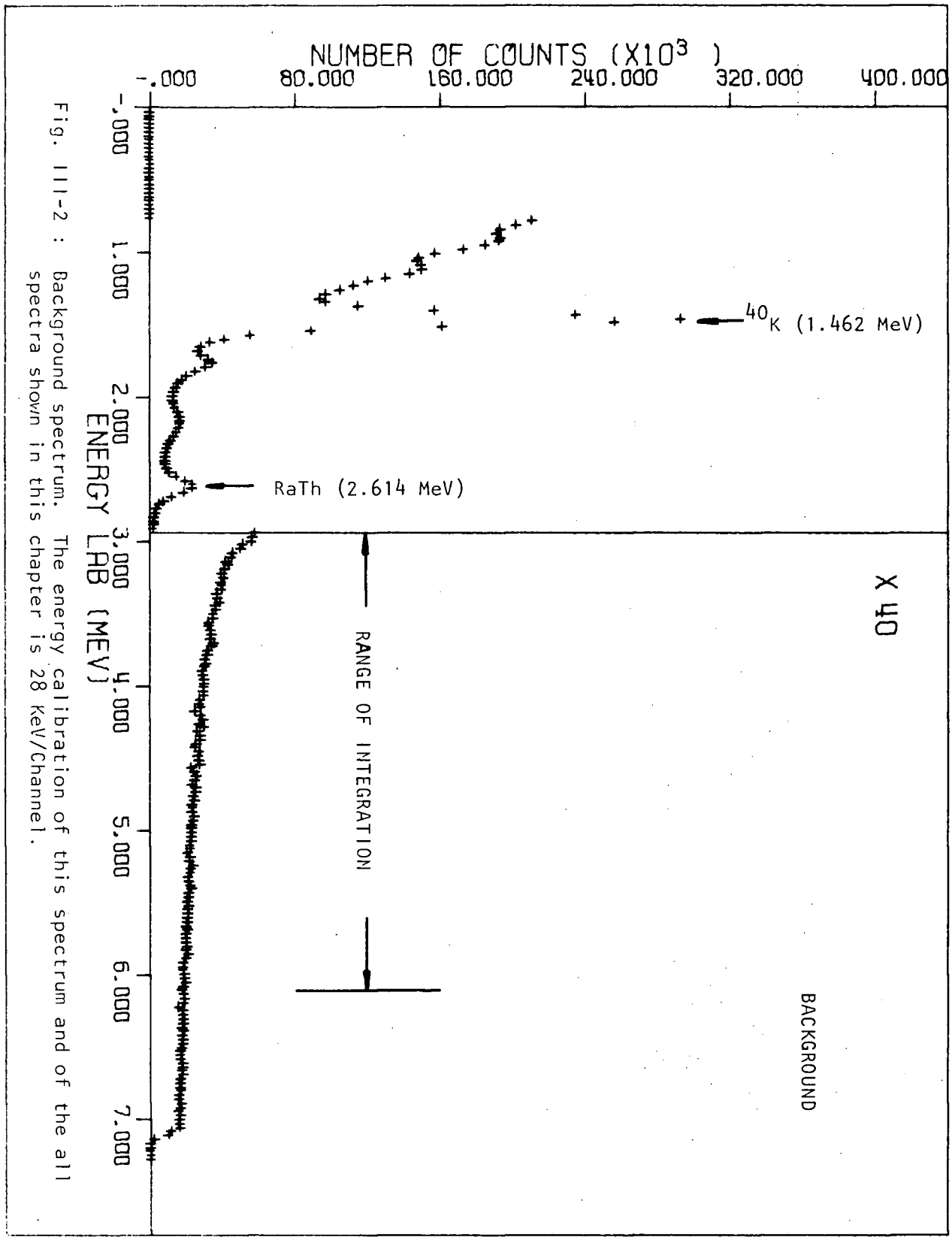

Fig. III-2 : Background spectrum. The energy calibration of this spectrum and of the all spectra shown in this chapter is 28 KeV/Channel.

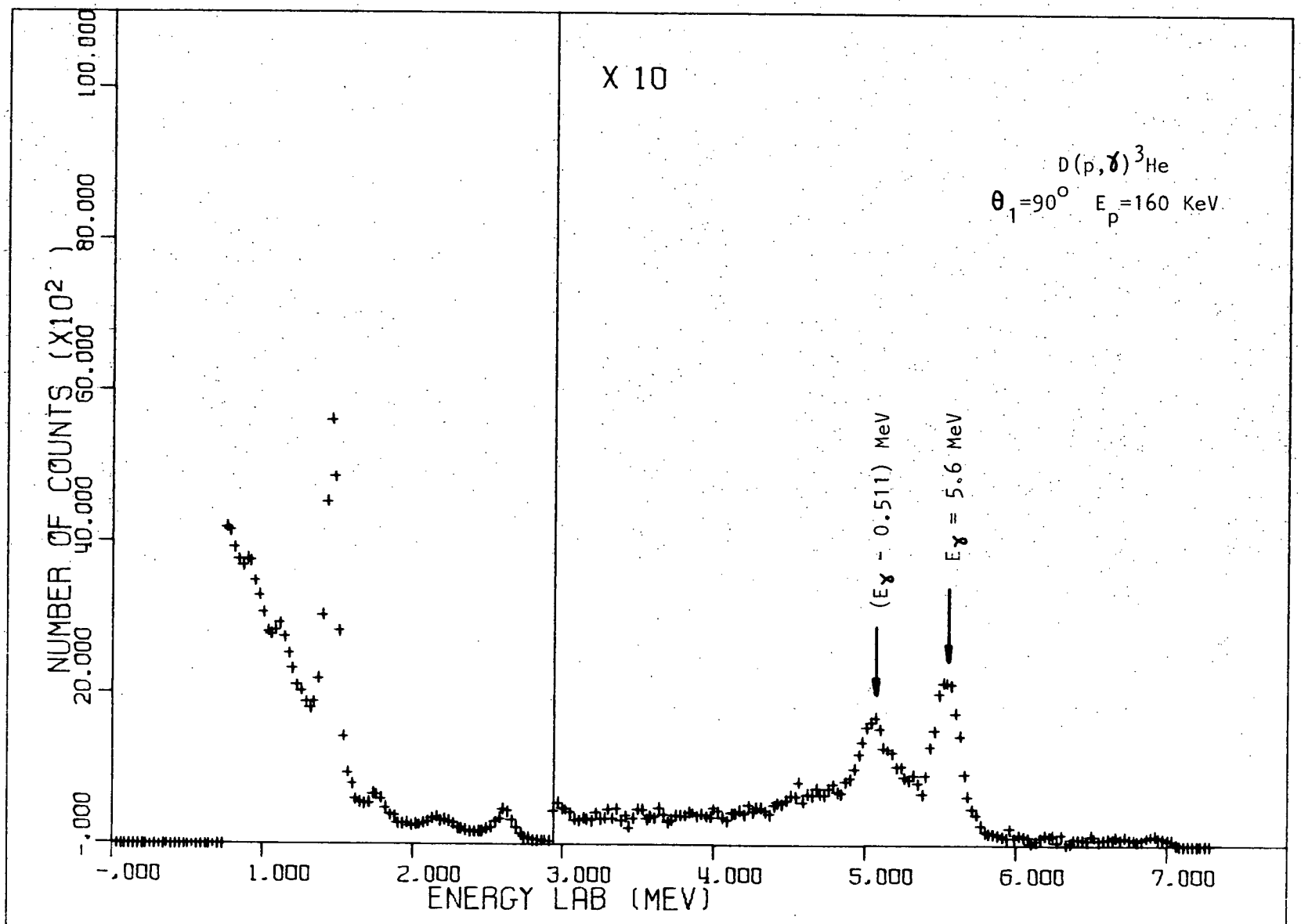

Fig. III-3 : $D(p,\gamma)^3He$ gamma-ray spectrum.

i	θ_1	A	θ_2	B	T(sec)	C	D	E	F	G	$_G\sigma^2$	H	$_H\sigma^2$
0	----	101535	----	99282	315000	----	----	----	----	----	----	----	----
1	-30	1793	-120	2734	3360	1083	1059	710	1675	1076	5272	1147	5996
2	-22	1760	-120	3160	3840	1238	1210	522	1950	679	3389	721	3822
3	-15	1502	-120	2807	3840	1238	1210	264	1597	420	4025	445	4518
4	-8	1461	-120	2880	3840	1238	1210	223	1669	339	3528	358	3948
5	0	2792	-120	5252	7680	2476	2421	317	2831	284	2344	300	2621
6	8	2995	-120	5996	7680	2476	2421	519	3575	368	1603	390	1794
7	15	1600	-120	2898	3840	1238	1210	362	1687	544	3952	576	4436
8	22	1627	-120	2724	3840	1238	1210	389	1514	652	5121	693	5775
9	30	1855	-120	2730	3360	1083	1059	772	1671	1173	5655	1251	6432
10	45	2255	-120	2692	3840	1238	1210	1017	1482	1741	10391	1884	12166
11	60	4222	-120	4201	5280	1702	1664	2520	2537	2520	8423	2817	10527
12	60	718	-90	792	960	309	303	409	490	409	1272	----	----
13	67	1484	-90	1531	1920	619	605	865	926	456	792	----	----
14	75	1629	-90	1646	1920	619	605	1011	1041	476	706	----	----
15	82	1689	-90	1623	1920	619	605	1070	1017	515	809	----	----
16	90	4141	-90	3860	5040	1625	1589	2517	2272	543	415	----	----
17	95	1598	-90	1595	2160	696	681	902	915	483	906	----	----
18	100	1513	-90	1503	1920	619	605	894	898	488	896	----	----
19	105	1491	-90	1573	1920	619	605	872	968	441	711	----	----
20	112	1641	-90	1792	1920	619	605	1022	1187	422	507	----	----
21	120	1467	-90	1713	1920	619	605	848	1108	375	484	----	----
22	127	1035	-90	1305	1680	542	530	494	775	312	627	----	----
23	135	622	-90	948	960	309	303	313	646	237	487	----	----

Table III-1 : $D(p,\gamma)^3He$ gamma-ray angular distribution data (90 KeV Run)

Table III-2 : $D(p,\gamma)^3He$ gamma-ray angular distribution data (160 KeV Run)

i	θ_1	A	θ_2	B	T(sec)	C	D	E	F	G	$_G\sigma^2$	H	$_H\sigma^2$
0	----	101535	----	99282	315000	----	----	----	----	----	----	----	----
1	-30	2125	-120	3851	3227	1040	1017	1085	2834	1832	7701	1989	9278
2	-15	1444	-120	3962	2528	815	797	629	3165	950	3670	1023	4253
3	0	3094	-120	10602	6957	2242	2193	852	8409	485	1053	520	1214
4	8	1689	-120	4628	3695	1191	1165	498	3463	688	3432	739	3963
5	15	1797	-120	4690	3225	1040	1016	758	3674	987	3404	1062	3944
6	22	1780	-120	3901	2992	964	943	816	2958	1320	5460	1425	6366
7	30	2295	-120	4134	3151	1016	993	1279	3141	1948	6940	2115	8180
8	45	3058	-120	3824	2647	853	834	2205	2990	3527	13179	3901	16119
9	60	6078	-120	6293	4789	1544	1509	4534	4783	4534	11777	5229	15658
10	60	5350	-90	5787	3191	1029	1006	4321	4781	4321	10096	----	----
11	67	1877	-90	1899	1049	338	331	1539	1568	4690	34443	----	----
12	75	3973	-90	3898	3382	1090	1066	2883	2832	4867	22904	----	----
13	79	4563	-90	4245	2553	823	805	3740	3441	5198	18527	----	----
14	82	4300	-90	3989	3266	1053	1029	3247	2960	5245	23806	----	----
15	86	1602	-90	1494	1029	332	324	1270	1169	5194	56284	----	----
16	90	7282	-90	6692	4962	1599	1564	5682	5128	5298	13520	----	----

(Continuation)

17	95	8752	-90	8310	5322	1715	1677	7037	6633	5072	9438	----	----
18	97	7277	-90	7038	4915	1584	1549	5692	5489	4958	11303	----	----
19	101	7882	-90	7439	4519	1457	1424	6425	6015	5107	10372	----	----
20	105	6736	-90	6809	4747	1530	1498	5206	5313	4685	10785	----	----
21	108	4849	-90	4985	2982	961	940	3888	4045	4595	13230	----	----
22	112	2568	-90	2776	1606	518	506	2050	2270	4319	21464	----	----
23	120	3652	-90	4341	3609	1163	1137	2489	3204	3714	14012	----	----
24	127	2178	-90	2818	1564	504	493	1674	2325	3442	15402	----	----
25	135	1561	-90	2677	1666	537	525	1024	2152	2274	10704	----	----

There was no appreciable beam dependent background that could affect the angular distribution measurements. This is discussed in Appendix H.

The separate runs are listed in order of increasing θ_1. However, the actual order in which runs were done was alternated. Column T indicates the total running time at each angle.

The dead time for both kicksorters was less than 0.5% and was determined primarily by the background counting rate. No correction has been applied for this dead time and the time T was taken to be the actual running time for both detectors.

For configuration "A" a correction was applied to account for the changing gamma-ray absorption in the target holder as a function of counter angle. (See Appendix G). The corrected number of counts is found in column H. Absorptions in the wall of the chamber and in the crystal's container were not taken into account because these did not depend on the angular position of the detector.

A summarized explanation of the Tables III-1 and III-2 is given below.

A_i = Integrated number of counts in detector #1.

B_i = Integrated number of counts in detector #2.

T_i = Total running time for each angle.

C_i = Number of background counts in detector #1 normalized to time T_i.

D_i = Number of background counts in detector #2 normalized to time T_i.

E_i = Number of counts A_i less number of background counts C_i.

F_i = Number of counts B_i less number of background counts D_i.

G_i = Number of counts E_i normalized to number of counts F_i.

H_i = Number of normalized counts G_i in detector #1 corrected due to target holder absorption.

$A(i = 0)$ = Integrated number of background counts in detector #1.

$B(i = 0)$ = Integrated number of background counts in detector #2.

$T(i = 0)$ = Total time in which the background run was performed.

The following expressions show the tabulated quantities with their standard deviations:

$$A_i \pm \Delta A_i = A_i \pm \sqrt{A_i} \qquad B_i \pm \Delta B_i = B_i \pm \sqrt{B_i}$$

$$C_i \pm \Delta C_i = \left(A_o \frac{T_i}{T_o}\right) \pm \frac{T_i}{T_o}\sqrt{A_o}$$

$$D_i \pm \Delta D_i = \left(B_o \frac{T_i}{T_o}\right) \pm \frac{T_i}{T_o}\sqrt{B_o}$$

$$E_i \pm \Delta E_i = (A_i - C_i) \pm \sqrt{(\Delta A_i)^2 + (\Delta C_i)^2} = \left(A_i - A_o\frac{T_i}{T_o}\right) \pm \sqrt{A_i + \frac{T_i^2}{T_o^2}A_o}$$

$$F_i \pm \Delta F_i = (B_i - D_i) \pm \sqrt{(\Delta B_i)^2 + (\Delta D_i)^2} = \left(B_i - B_o\frac{T_i}{T_o}\right) \pm \sqrt{B_i + \frac{T_i^2}{T_o^2}B_o}$$

$$G_i \pm \Delta G_i = \frac{E_i}{F_i} V \pm \sqrt{{}_G\sigma_i^2}$$

$${}_G\sigma_i^2 = \left(\frac{\partial G}{\partial E_i}\right)^2 (\Delta E_i)^2 + \left(\frac{\partial G_i}{\partial F_i}\right)^2 (\Delta F_i)^2 = \frac{\left(A_i + \frac{T_i^2}{T_o^2}A_o\right)V^2}{F_i^2} + \frac{\left(B_i + \frac{T_i^2}{T_o^2}B_o\right)E_i^2 V^2}{F_i^4}$$

where V is an arbitrary constant chosen to provide a convenient scale, and

$$H_i \pm \Delta H_i = \frac{G_i}{Z_i} \pm \sqrt{{}_H\sigma_i^2} \qquad {}_H\sigma_i^2 = \frac{{}_G\sigma_i^2}{Z_i^2}$$

where Z_i is the absorption correction factor discussed in Appendix G. It was assumed that Z_i has no statistical error. This correction applies only to the target detector configuration "A".

3.2. The Angular Distribution Function

It is convenient to express the results of an angular distribution measurement as a Legendre polynomial series:

$$W(\theta) = \sum_{\ell=0}^{2} B_\ell P_\ell (\cos\theta) \qquad (3.2 - 1)$$

This is particularly useful because it simplifies the solid angle corrections. Rose (RO 53) has shown that, if the data is fitted to a function of the form (3.2 - 1) then, the corrected angular distribution function is simply given by

$$W(\theta) = \sum_{\ell=0}^{2} A_\ell P_\ell (\cos\theta)$$

where $A_1 = B_1/Q_1$. The smoothing factors Q_1 can be obtained by an integration over the volume of the detector (See Chapter II). The calculated smoothing factors for the detector assembly used in this experiment are shown in Table III-3.

Table III-3 : Smoothing Factors Calculated at $E\gamma$ = 5.58 MeV for the Detector Geometry Shown in Fig. II-6.

1	0	1	2	3	4
Q_1	1.00000	0.98839	0.96546	0.93174	0.88803

3.3. The Fitting Procedure

For each angle θ_i the probability of observing N_i counts

is given by the Poisson distribution

$$P_i = (W_i)^{N_i} e^{-W_i} / N_i!$$

where $W_i = W(B;\theta_i)$ is the curve to be fitted where B stands for the set of angular distribution coefficents B_l.

The joint probability of getting a particular arrangement of experimental results $N_1,\ldots,N_i,\ldots,N_p$ at the angles $\theta_1,\ldots,\theta_i,\ldots,\theta_p$ is the likelihood function $L = \prod_{i=1}^{p} P_i$ providing the events N_i are independent.

The problem here is to find the set of B_l say B_l^* which maximize the function L. The best fit curve is then given by $W = W(B^*;\theta)$. If we take the logarithm of L, then

$$S = \ln L = \sum_{i=1}^{p} \ln P_i = \sum_{i=1}^{p} [N_i \ln W_i - W_i - \ln(N_i!)]$$

the solutions are then obtained from the r simultaneous equations

$$\frac{\partial S}{\partial B_l} = 0 \qquad l = 0, r$$

that is:

$$\sum_{i=1}^{p} \left(\frac{N_i - W_i}{W_i}\right) \frac{\partial W_i}{\partial B_l} = 0 \qquad l = 0, r \qquad (3.3 - 1)$$

These equations are non-linear in B_l, but the problem can be simplified as indicated below:

If W_i in the denominator of equation (3.3 - 1) is replaced by N_i, that is, if the following approximation $W_i \simeq N_i$ is made then the solutions can be found from

$$\sum_{i=1}^{p} \frac{(N_i - W_i)}{N_i} \frac{\partial W_i}{\partial B_l} = 0 \qquad l = 0, r$$

where this set of r equations is now linear in B_l.

This result can also be shown to be a direct consequence of the principle of minimum variance which says that the best estimate for the set B_l can be obtained by a least squares method; i.e.

$$\sum_{i=1}^{P} m_i \left(N_i - W_i \right)^2 = \text{minimum}$$

if the weights m_i are inversely proportional to the variance N_i. If we define M as

$$M = \sum_{i=1}^{P} \frac{\left(N_i - W_i \right)^2}{N_i}$$

then the solutions $B_l = B_l^*$ can be obtained from the r simultaneous equations

$$\frac{\partial M}{\partial B_\ell} = 0 \qquad \ell = 0, r$$

The standard deviations in the parameters B_l^* are given by the error matrix (OR 58)

$$\overline{(B_l - B_l^*)(B_k - B_k^*)} = (H^{-1})_{l,k} \qquad l,k = 0,r$$

where

$$H_{\ell,k} = \frac{1}{2} \frac{\partial^2 M}{\partial B_\ell \partial B_k}$$

The square root of the diagonal elements of the matrix H^{-1} are the standard deviations in the parameters B_l^* and the off-diagonal elements $\overline{\Delta B_l \, \Delta B_k}$ define the degree of correlation between them.

As was stated earlier in this chapter the readings at the different angles were taken using two different configurations. In order to procede with the fitting analysis the experimental data obtained from these two configurations have to be related to each other. This could be done as follows. At both 90 KeV and 160 KeV the discontinuity occurs at $\theta_1 = 60^\circ$ as shown in Fig. III-4. Therefore, if we call R the factor which when multiplied by the configuration "B" data would make it fit smoothly to the configuration "A" data, then from Fig. III-4 and Tables III-1 and III-2

$$R = H(\theta_1=60^\circ)_{"A"} \;/\; G(\theta_1=60^\circ)_{"B"}$$

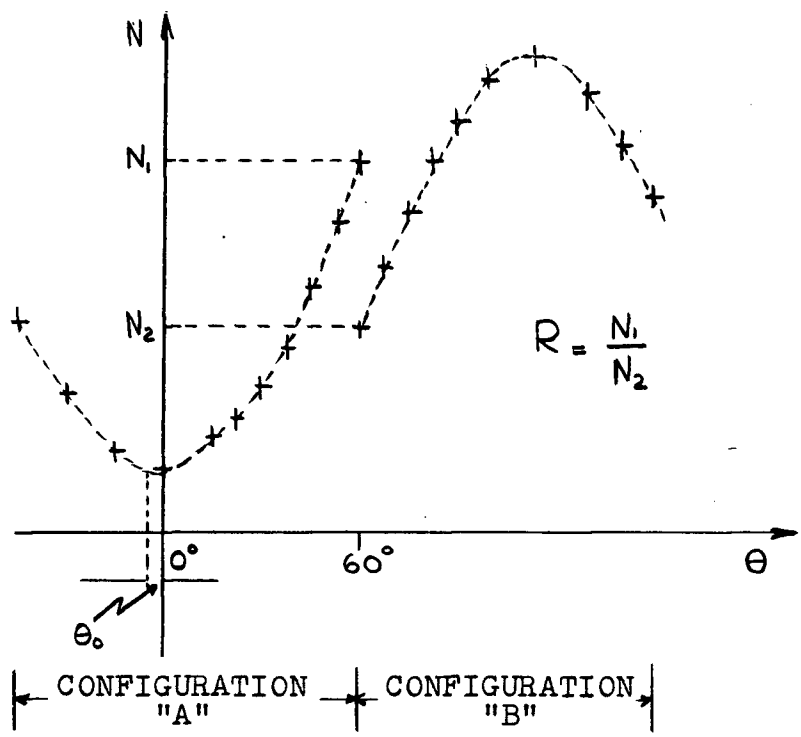

Fig. III-4 : Experimental angular distribution. N is the relative number of counts taken in both configurations as a function of the angle θ in the laboratory frame. θ_0 denotes the shift in the experimental angular scale. The points shown here were arbitrarily drawn.

The application of the least squares method will then give the solution sought.

There is, however, an important difficulty with this approach. The set of data in the configuration "B" may be affected by a systematic error, that is, all the points may lie above or below the actual value unless the data at 60° in both configurations are taken to a high degree of accuracy. Assuming that this is done it still will not be the proper procedure because all the data points in the configuration "B" will be weighted according to what happened at one particular angle.

The approach chosen to overcome this difficulty is outlined below. The data is to be fitted to a function of the following type:

$$W = \left[\sum_{\ell=0}^{\lambda} B_\ell P_\ell (\cos\theta) \right] (1 + \varepsilon K)$$

where

$$\varepsilon = \begin{cases} 0 & \text{(configuration "A")} \\ 1 & \text{(configuration "B")} \end{cases}$$

K is then treated as a new parameter to be determined by the least squares fit. K corresponds to $\left(\frac{1}{R} - 1\right)$; however, it must be pointed out that R is a constant determined by the ratio between two experimental data points taken at one particular angle while K is a parameter determined by the least squares fit which depends on all of the experimental data.

Finally the uncertainty in the zero of the angular scale

must be considered. Although the 1^{o} graduations in the angle scale of the angular distribution table (Chapter II) were machined to better than 0.2 degree, its orientation with respect to the incoming beam could not be determined better than 1^{o}. This is in itself small. However, because a small asymmetry around 90^{o} is to be expected (DO 67) it is important to eliminate experimental factors which might contribute to such an asymmetry. Therefore, the experimental data, was finally fitted to a function of the following type:

$$W = \left\{ \sum_{\ell=0}^{r} B_\ell \; P_\ell \left[\cos(\theta + \theta_o) \right] \right\} \left(1 + \varepsilon K \right) \qquad (3.3 - 2)$$

where θ_o was treated as another parameter to be determinated from the experimental data. Because this function is no longer linear in all the parameters an iterative method devised by Falk (FA 65) and Orth (OR 67) was used to fit this function to the experimental data. Briefly the method consists in the expansion of $\frac{\partial M}{\partial B_\ell}(\ell=0,r)$, $\frac{\partial M}{\partial K}$ and $\frac{\partial M}{\partial \theta_o}$ in the first order Taylor series about initial values of the parameters B_1, K and θ_o to be determined. For convenience we rename the parameters $\theta_o = B_{r+1}$ and $K = B_{r+2}$. Then

$$\frac{\partial M}{\partial B_\ell} = \left.\frac{\partial M}{\partial B_\ell}\right|_{B_\ell = B_{\ell_o}} + \sum_{j=0}^{r+2} \left.\frac{\partial^2 M}{\partial B_\ell \, \partial B_j}\right|_{\substack{B_\ell = B_{\ell_o} \\ B_j = B_{j_o}}} \Delta B_j \qquad l = 0, r+2$$

We have here a set of r+2 equations which are linear in the increments B_j in the parameters. If we apply the least squares method to find the minimum value of M then

$$0 = \left.\frac{\partial M}{\partial B_\ell}\right|_{B_\ell = B_\ell^*} = \left.\frac{\partial M}{\partial B_\ell}\right|_{B_\ell = B_{\ell_o}} + \sum_{j=0}^{r+2} \left.\frac{\partial^2 M}{\partial B_\ell \, \partial B_j}\right|_{\substack{B_\ell = B_{\ell_o} \\ B_j = B_{j_o}}} \Delta B_j \qquad l = 0, r+2$$

If one starts with arbitrary initial values $B_{j,o}$ of the parameters B_j one can calculate the first and second derivatives of M using its definition. The above r+2 equations can then be solved for the r+2 increments ΔB_j in the parameters to give a new set of parameters $B_{j,1} = B_{j,o} + \Delta B_j$ which satisfy the above conditions. These new values of the parameters B_j will differ from the best values B_j^* in the first iteration because we are considering only the first term in the Taylor series.

Then the procedure is to repeat the operation again, now using $B_{j,1}$ as the new initial values of the parameters. This operation is repeated until $\frac{\Delta B_j}{B_{ji}} = \frac{B_{ji} - B_{j(i-1)}}{B_{ji}}$ $j = 0,r+2$ is less than some chosen value. A computer program written by Orth (OR 67A) to fit a sum of two exponentials was modified to accept the function (3.3 - 2).

These iterative calculations must start with initial values of the parameters which should be chosen reasonably close to the correct values if the process is to converge quickly or at all. The initial value given to θ_o was obtained by plotting the yield around 0^o for the 160 KeV and 90 KeV runs. A zero shift of approximately 2^o was noted and this value was chosen for θ_o. The initial estimate for K was obtained from the value of R, estimated for 60^o data that is $K = 1/R - 1$.

The initial estimates for the parameters B_1 were obtained by fitting the data to the function (3.2 - 1). A least squares fitting program for linear functions was used in this

case. Here the data from both configurations were related using the factor R and θ_o was assumed to be zero.

3.4. The Results

Experimental results from previous work (Chapter I) indicate that the angular distribution of the gamma-rays from the reaction $D(p,\gamma)^3He$ at low energies (24 KeV to 1.75 MeV) has, at least in first approximation, the form $W(\theta) = a + b \sin^2\theta$ (or if expressed in terms of Legendre polynomials $W(\theta)=A_oP_o+A_2P_2$) However, recent theoretical calculations (DO 67) indicate that terms higher than P_2 may be present in the angular distribution of this reaction even at energies below 200 KeV.

Therefore, the function chosen in the present analysis includes terms up to P_4 in the Legendre polynomial series. Table III-4 shows the results of the fitting for the 90 KeV and 160 KeV runs. Fits were obtained for several different sets of Legendre polynomial parameters B_1.

In rows 1 and 6 the experimental data was fitted to the following Legendre polynomial series

$$W(\theta) = \left\{ \sum_{\ell=0}^{4} B_\ell \, P_\ell \left[\cos(\theta+\theta_o)\right] \right\} (1+\varepsilon K)$$

with

$$\varepsilon = \begin{cases} 0 & -30^\circ \leqslant \theta \leqslant 60^\circ \quad \text{(configuration "A")} \\ 1 & 60^\circ \leqslant \theta \leqslant 135^\circ \quad \text{(configuration "B")} \end{cases}$$

in which the parameters B_1, B_3, and B_4 were set identically equal

to zero. Similarly, rows 2 and 7 show the result obtained when the parameters B_1 and B_3 were set equal to zero. Rows 3 and 8 correspond to the case in which all the parameters were left free. In rows 5 and 10 the experimental points were fitted to the same function in which all the parameters but B_3 were set free. The particular restrictions imposed here are discussed in Chapter IV. The condition imposed on this parameter was that the angular distribution obtained from the fit must give the same value at 0° and 180° when the solid angle correction was applied. That is, $A_3 = -A_1$ which means that the condition imposed on the parameters B_1 was $B_3 = -Q_3/Q_1\ B_1^{-1}$ where Q_1 and Q_3 are the smoothing factors. The function used for this case was

$$W(\theta) = \left[B_0 P_0 + B_1\left(P_1 - \frac{Q_3}{Q_1} P_3\right) + B_2 P_2 + B_4 P_4\right]\ (1 + \varepsilon K)$$

Finally in rows 4 and 9 the results are shown for the case when all the parameters but A_4 were set free. Here however, the condition imposed on that parameter was that the corrected angular distribution must be equal to zero at $\theta_1 = 180^\circ$. This condition follows if the value of A_4 is restricted to

$$A_4 = -A_0 + A_1 - A_2 + A_3$$

In this case the function used was

$$W(\theta) = \left[B_0\left(P_0 - \frac{Q_4}{Q_0} P_4\right) + B_1\left(P_1 + \frac{Q_4}{Q_1} P_4\right) + B_2\left(P_2 - \frac{Q_4}{Q_2} P_4\right) + B_3\left(P_3 + \frac{Q_4}{Q_3} P_4\right)\right](1 + \varepsilon K)$$

The same program includes the usual Chi-squared test. The test was made on each fit and the results are shown in Table III-4. The number of degrees of freedom corresponding to

each fit are shown in the column denoted by ν .

The normalized probability of obtaining a value of χ^2 greater than or equal to the value obtained in each particular fit was found from the χ^2 tables and is shown in column denoted by p. (1 - p) gives then the probability of obtaining a better fit to the function already determined if the experiment is repeated under the same experimental conditions. The best values obtained for θ_o and K in each fit and the square root of the variance for all parameters (ΔB_1, $\Delta\theta_o$ and ΔK) are shown in Table III-4. For each fit the iteration was carried on until the ratio of the parameters for successive steps was less than 0.001 (0.1%) for all parameters. On the average four iterations were needed to achieve this ratio.

The angular distribution parameters shown in Table III-4 were calculated for the centre of mass system. The input data were transformed to the centre of mass in the same program using equations given in Appendix C before the fitting procedure was carried out.

	B_o	ΔB_o	B_1	ΔB_1	B_2	ΔB_2	B_3	ΔB_3	B_4	ΔB_4
# 1	2438	103	0	0	-2142	117	0	0	0	0
# 2	2583	175	0	0	-2369	251	0	0	109	105
# 3	2288	298	185	173	-2138	300	-25	229	-15	207
# 4	2313	223	166	78	-2133	304	-53	79	7	104
# 5	2367	227	123	81	-2123	302	-116	76	57	111
# 6	4596	106	0	0	-4069	115	0	0	0	0
# 7	4805	134	0	0	-4396	177	0	0	157	76
# 8	4238	232	451	151	-4110	232	91	186	-158	163
# 9	4438	182	300	76	-4110	240	-100	74	14	80
#10	4549	187	219	77	-4111	245	-206	73	106	89

Table III-4a : $D(p,\gamma)^3He$ angular distribution least squares fit parameters for 90 KeV and 160 KeV runs.

	θ_o (rad)	$\Delta\theta_o$ (rad)	K	ΔK	χ^2	ν	p	$\bar{E}_p$ (KeV)
# 1	0.020	0.011	-0.856	0.007	12.79	18	0.79	
# 2	0.016	0.011	-0.865	0.010	11.64	17	0.83	
# 3	0.012	0.012	-0.847	0.019	9.53	15	0.84	70
# 4	0.012	0.012	-0.848	0.016	9.54	16	0.89	
# 5	0.011	0.012	-0.851	0.016	9.70	16	0.88	
# 6	0.029	0.007	-0.216	0.020	35.14	20	0.02	
# 7	0.026	0.007	-0.255	0.023	31.72	19	0.03	
# 8	0.012	0.008	-0.166	0.043	22.22	17	0.18	144
# 9	0.012	0.008	-0.193	0.037	23.31	18	0.19	
#10	0.012	0.008	-0.208	0.037	24.76	18	0.12	

Table III-4b : $D(p,\gamma)^3He$ angular distribution least squares fit parameters and Chi-squared test for 90 KeV and 160 KeV runs.

CHAPTER IV

DISCUSSION

In the previous chapter the measurement of the angular distribution for the reaction $D(p,\gamma)^3He$ and its description in terms of a Legendre polynomial series is described. In this chapter the experimental results are discussed and compared with the theoretical calculations made by Donnelly (DO 67). A brief description of a technique to be used in the future to determine the absolute cross section of this reaction as a function of energy is also presented.

4.1. Discussion of the Results

In table III-4 the Legendre polynomial coefficients B_1 were shown for the 90 KeV and 160 KeV runs without corrections for the finite solid angle of the detector. In order to correct the angular distributions for the finite solid angle of the detector (Chapter III), it is necessary to divide the Legendre polynomial coefficients by the smoothing factors Q_1 given in Table III-3. This could have been done by including the smoothing factors directly in the Legendre polynomial fitting program before the fit was carried out. This would have led directly to the same corrected coefficients, as the present approach in which the uncorrected coefficients are determined first.

Since the absolute cross section has not been measured it is convenient to remove the arbitrary intensity factor B_o and

express the other coefficients as a ratio B_1/B_o.

The final corrected results are shown in Table IV-1. F_1 is the expectation value of $B_1Q_o/B_oQ_1 = A_1/A_o$ and ΔF_1 is the square root of its variance. The percentage error $\eta = \Delta F_1/F_1 \times 100$ and the χ^2 percentage probability P (defined in Chapter III) are also included.

The expectation value F_1 and ΔF_1 were obtained as follows:

$$F_\ell = E\left(\frac{A_\ell}{A_o}\right) = E\left(\frac{B_\ell Q_o}{B_o Q_\ell}\right) = \frac{Q_o}{Q_\ell}\left[\frac{B_\ell}{B_o} - \frac{(H^{-1})_{o\ell}}{B_o^2} + \frac{B_\ell}{B_o^3}(H^{-1})_{oo}\right] \qquad \ell \neq 0$$

and

$$\Delta F_\ell = \sqrt{VAR(F_\ell)} = \frac{Q_o}{Q_\ell}\sqrt{\frac{(H^{-1})_{\ell\ell}}{B_o^2} - 2\frac{B_\ell}{B_o^3}(H^{-1})_{o\ell} + \frac{B_\ell^2}{B_o^4}(H^{-1})_{oo}} \qquad \ell \neq 0$$

where H^{-1} is the error matrix defined in Chapter III.

For the 144 KeV results if we accept the usual confidence level of 5%, the Chi-squared test eliminates case #6 with only A_o and A_2 coefficients as well as case #7 with coefficients A_o, A_2, and A_4. These cases are shown in Fig. IV-1 and Fig. IV-2, respectively. The functions plotted for comparison with the experimental data are evaluated not with the coefficients in Table IV-1 but with the coefficients in Table III-4 which contain the effect of the finite solid angle of the detector. In the remaining cases, #8, #9, and #10, all the coefficients were included with the constraints described in Chapter III.

	F_1	ΔF_1	η_1	F_2	ΔF_2	η_2	F_3	ΔF_3	η_3	F_4	ΔF_4	η_4	P	$\bar{E}_p$ (KeV)
# 1	0	0	0	-0.910	0.014	1.5	0	0	0	0	0	0	79	
# 2	0	0	0	-0.948	0.039	4.1	0	0	0	0.05	0.04	95	83	
# 3	0.091	0.085	93	-0.976	0.110	10.9	-0.005	0.1	1980	0.02	0.1	536	84	70
# 4	0.075	0.038	51	-0.951	0.049	5.1	-0.027	0.04	141	0.003	0.05	1472	89	
# 5	0.055	0.038	69	-0.025	0.047	5.1	-0.055	0.038	69	0.023	0.05	216	88	
# 6	0	0	0	-0.917	0.007	0.8	0	0	0	0	0	0	2	
# 7	0	0	0	-0.947	0.015	1.5	0	0	0	0.037	0.017	47	3	
# 8	0.109	0.040	37	-1.010	0.048	4.8	0.024	0.05	196	-0.044	0.045	103	18	144
# 9	0.069	0.019	27	-0.959	0.020	2.0	-0.025	0.018	75	0.004	0.02	570	19	
#10	0.049	0.018	37	-0.935	0.020	2.1	-0.049	0.018	37	0.026	0.021	83	12	

Table IV-1 : Legendre polynomial coefficients corrected for finite solid angle of the detector. F_i is the expectation value of A_i/A_o $[F_i=E(A_i/A_o)]$, η the percentage error $\Delta F_i/F_i$, and P the χ^2 test as defined in the text.

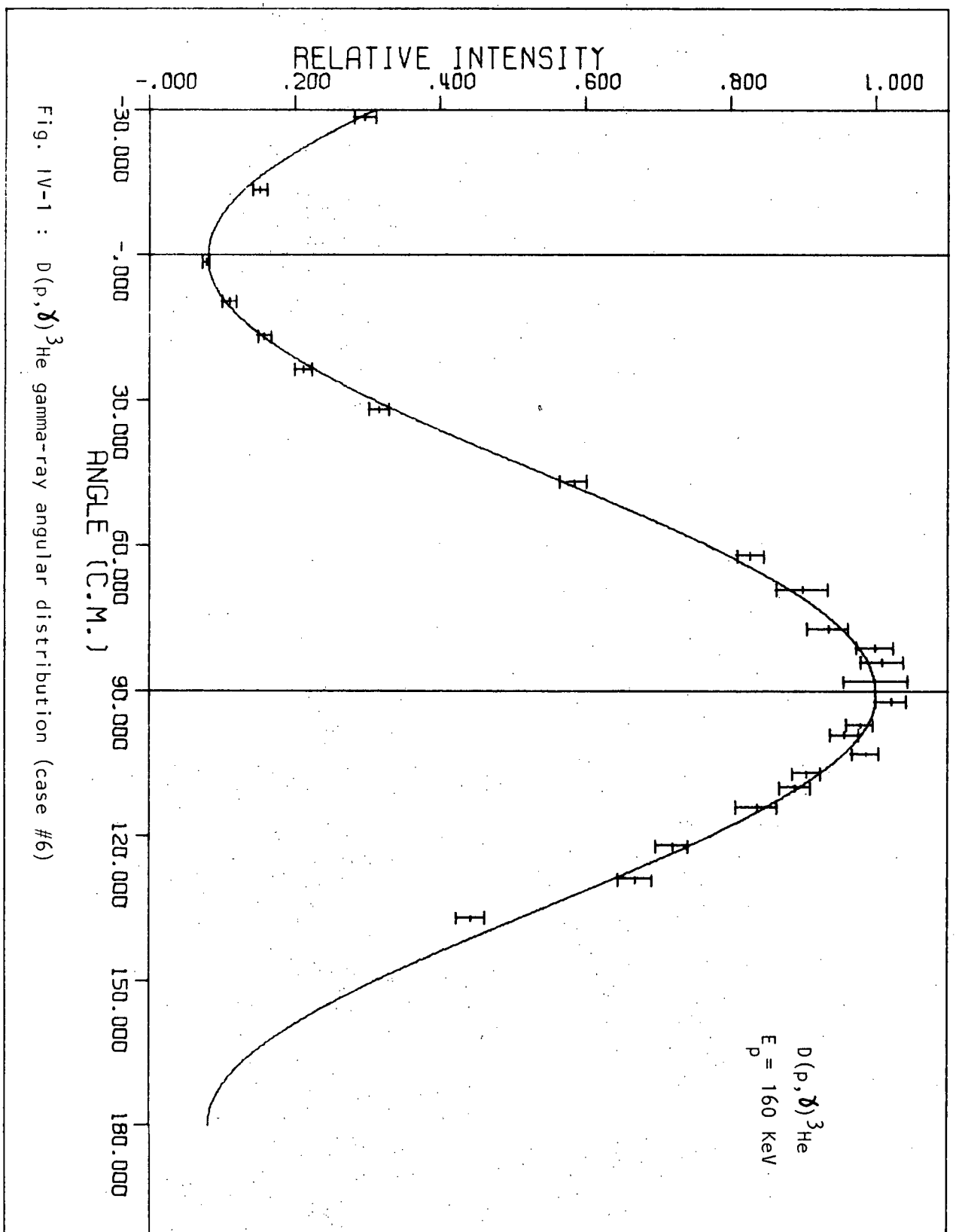

Fig. IV-1 : D(p,γ)^{3}He gamma-ray angular distribution (case #6)

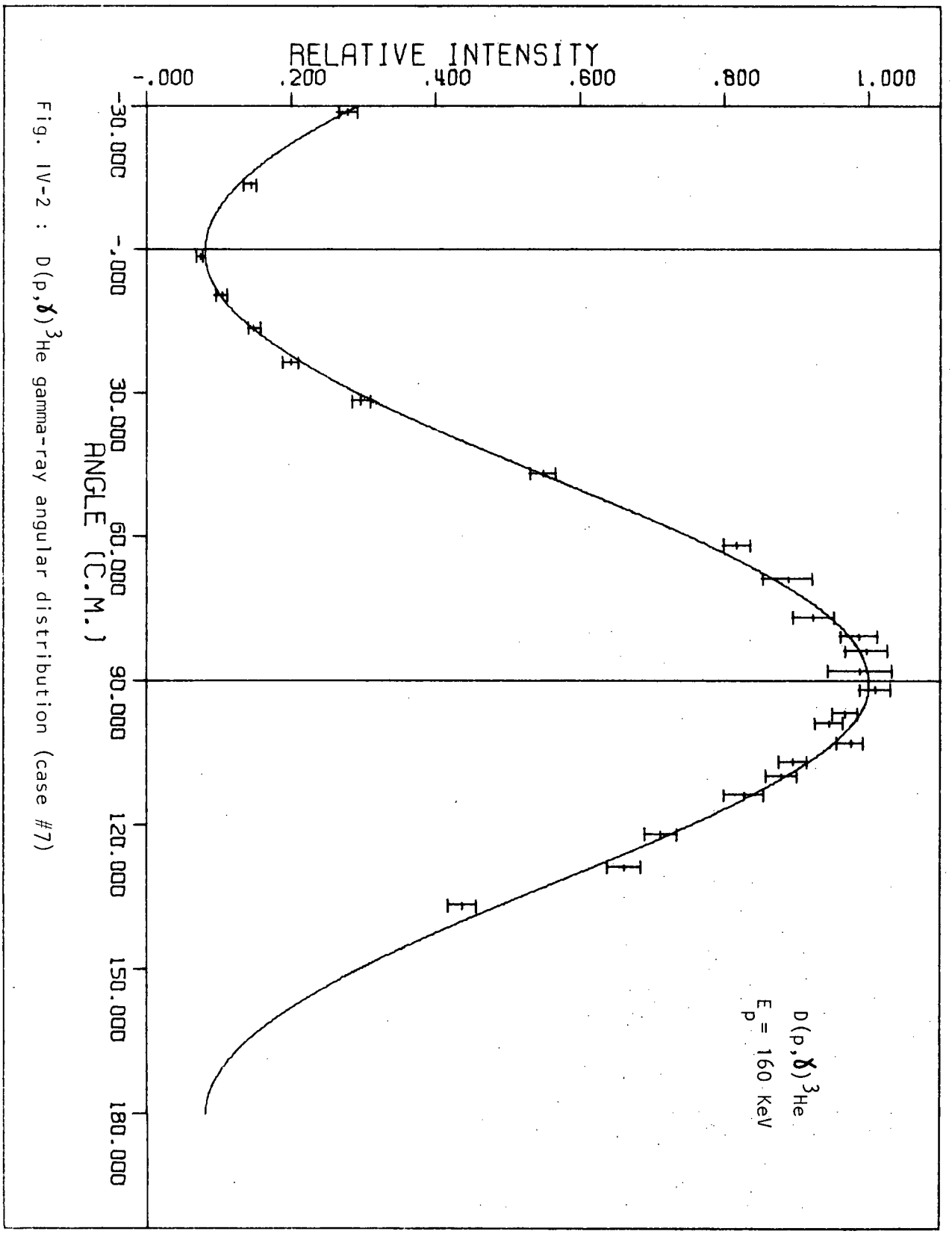

Fig. IV-2 : $D(p,\gamma)^3He$ gamma-ray angular distribution (case #7)

Consider case #8 for which no restrictions were imposed on any of the coefficients. The result of this fit is shown in Fig. IV-3. It is obvious that this case can not represent a physical situation because the angular distribution becomes negative for angles greater than approximately 165°. Although this fit represents the general case, because all the coefficients were free in the fitting process, it is not surprising to have obtained this type of result. This is because for angles greater than 135° there was no experimental data.

The least restriction that we can introduce so the results have physical significance is that the intensity function must be positive for all angles. It is clear from the shape of the curve that this condition can be met by making the function zero at 180°. This corresponds to case #9 shown in Fig. IV-4. Note that the function shown corresponds to the experimental curve including the effect of the finite solid angle of the detector so that it is not zero at 180°. Finally for case #10 the angular distribution was forced to have the same value at 0° and 180°. This is justified for physical reasons to be discussed later. The result is shown in Fig. IV-5.

Without biasing the interpretation of the data by a priori knowledge of theoretical calculations one can say that the cases #9 and #10 (Fig. IV-4, Fig. IV-5) represent good fits to the data and from the statistical point of view it is not possible to distinguish between them.

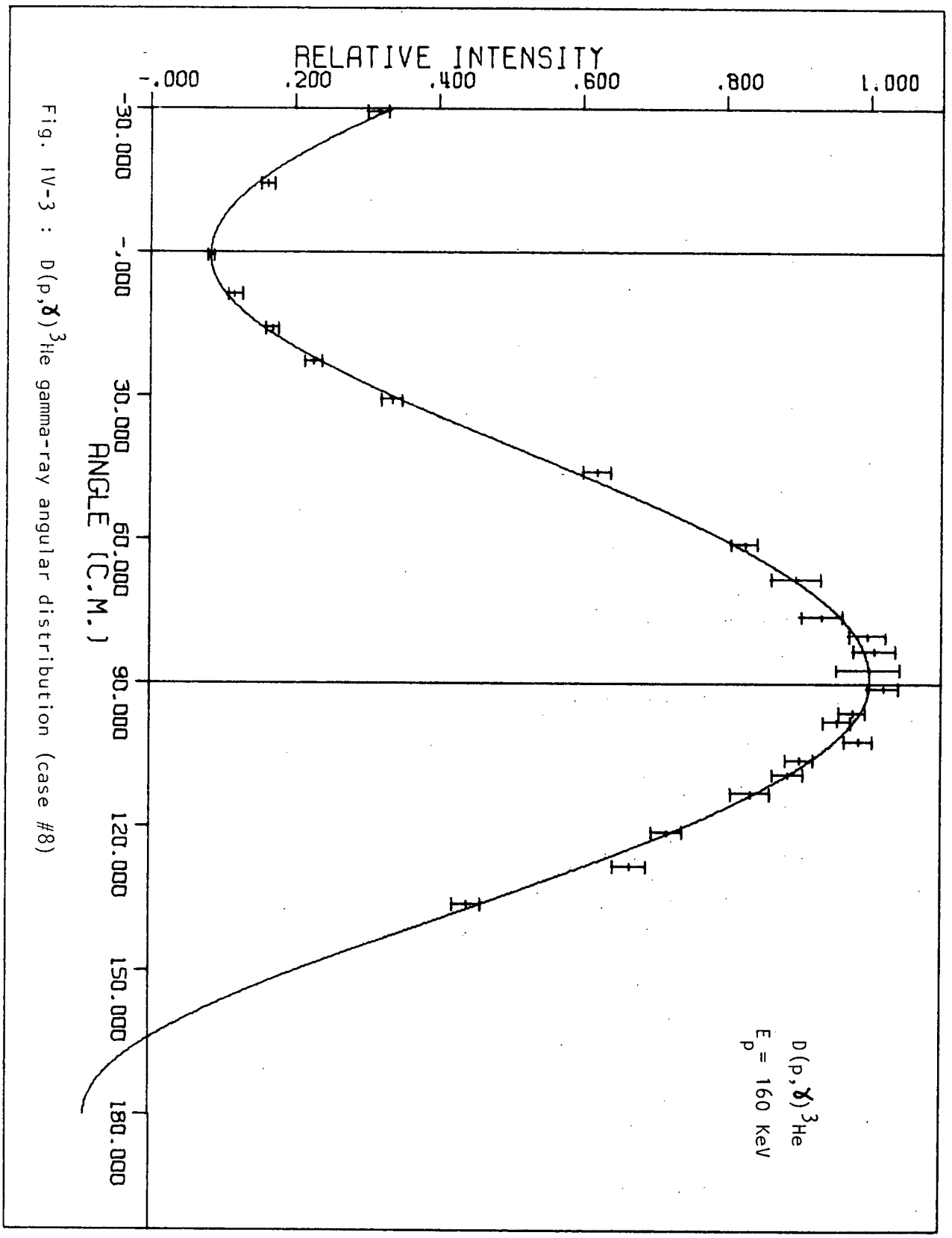

Fig. IV-3 : $D(p,\gamma)^3He$ gamma-ray angular distribution (case #8)

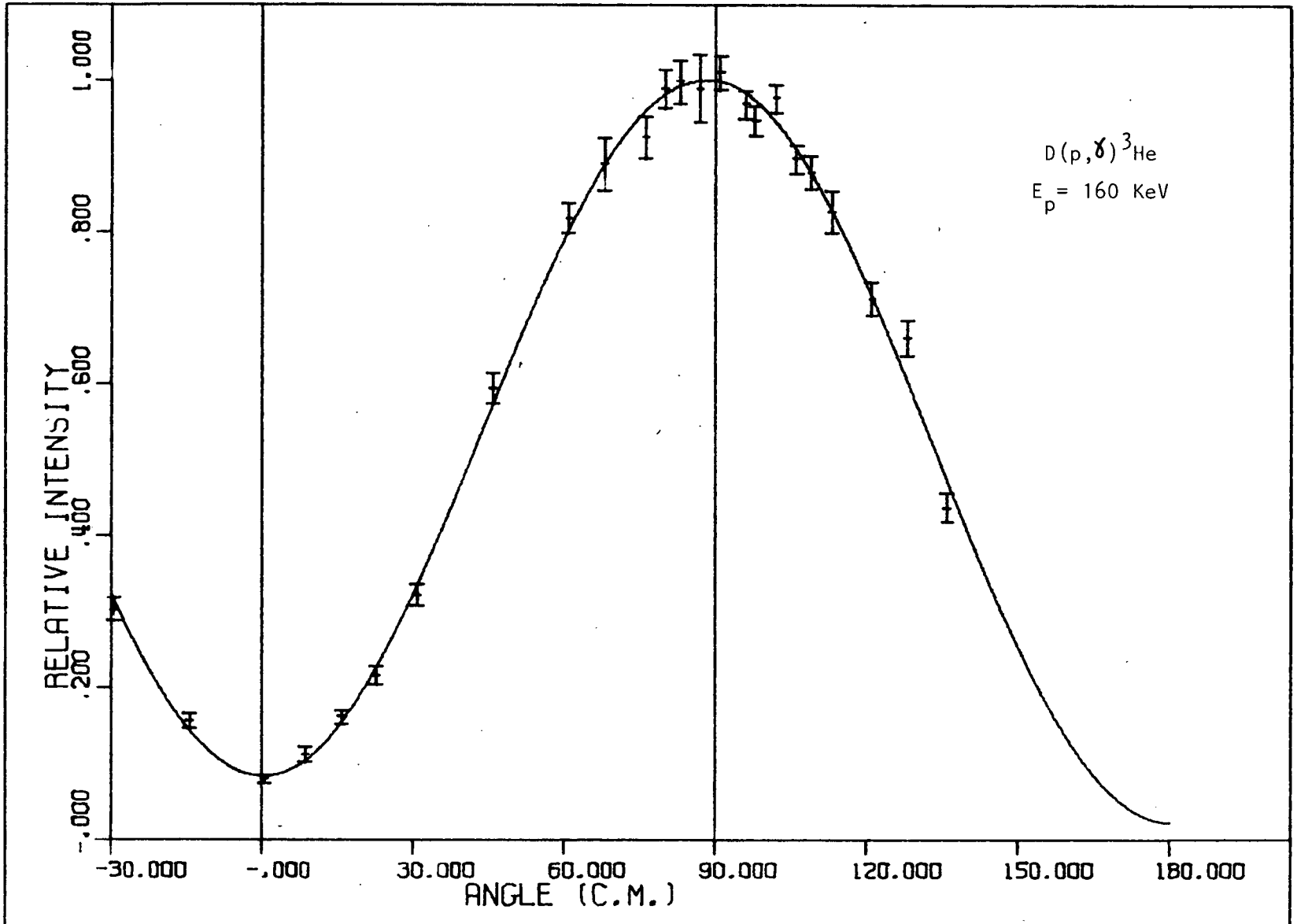

Fig. IV-4 : $D(p,\gamma)^3He$ gamma-ray angular distribution (case #9)

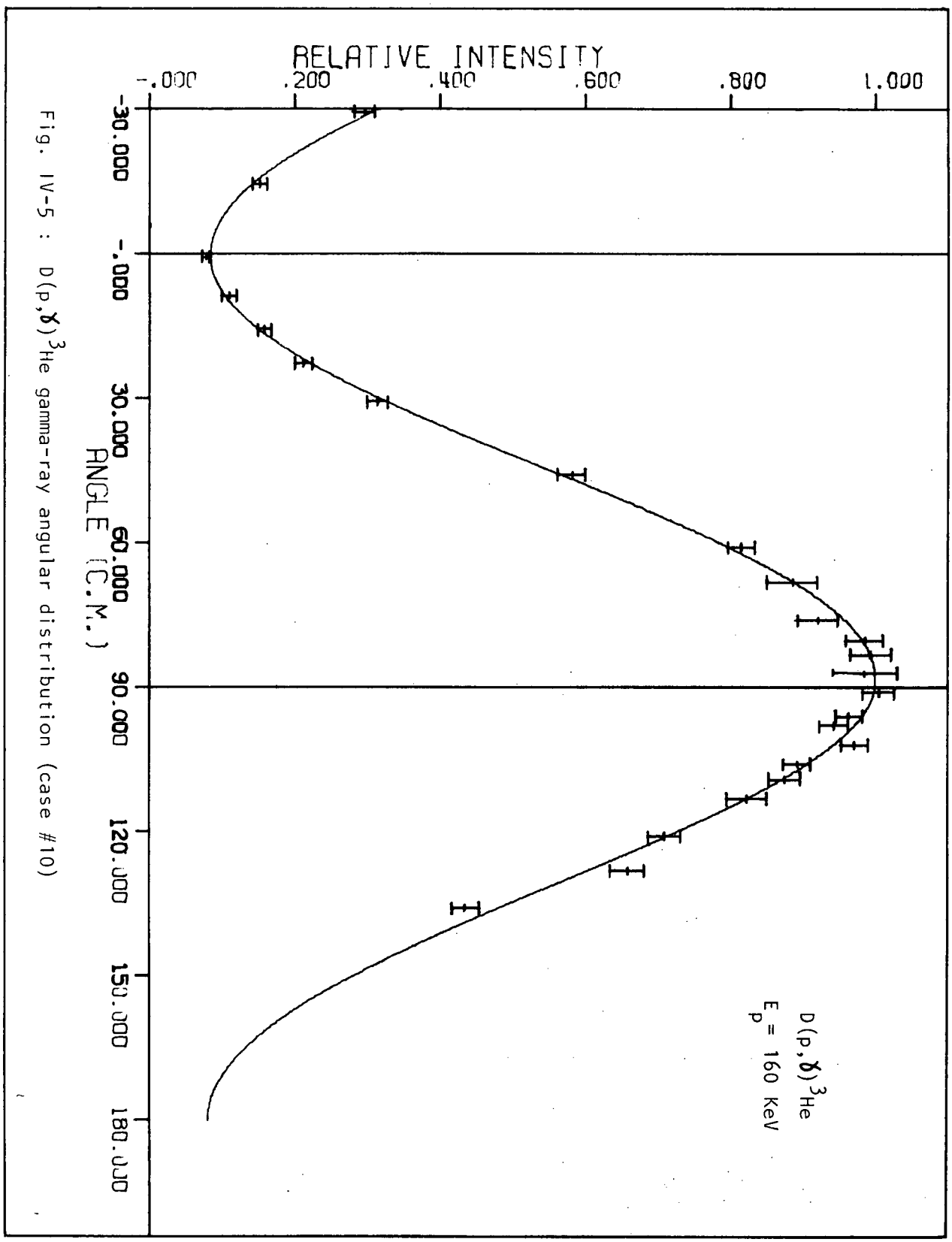

Fig. IV-5 : $D(p,\gamma)^3He$ gamma-ray angular distribution (case #10)

The angular distributions after correcting for the effect of the finite detector size are shown in Fig. IV-6, corresponding to the case where the function is zero at 180°, and Fig. IV-7 corresponding to the case where the value of the function at 0° equals the value at 180°.

For the 70 KeV data the situation is not as clear as for the 144 KeV. The Chi-squared test gives similar answers for all five fits to the data. Nevertheless if it is assumed that the angular distribution function at 70 KeV has the same form as that at 144 KeV then the first two cases can be rejected since they contain no odd Legendre polynomials while the third can be rejected as before since it leads to a negative value of the intensity function at backward angles. The final two cases are statistically indistinguishable; one corresponds to the requirement that the distribution go to zero at 180° while the other requires the same value at 0° and 180°. These distributions are of the same form as was required to fit the 144 KeV data and they do lead to a defined, although not very accurate, value for the coefficient of the first odd Legendre polynomial. Fig. IV-8 and Fig. IV-9 show the fit to the experimental data taken at 70 KeV for the parameters given in Table III-4, cases four and five.

4.2. Comparison with the Theoretical Calculations

As indicated in Chapter I the transition scheme for this reaction can be represented in the following way:

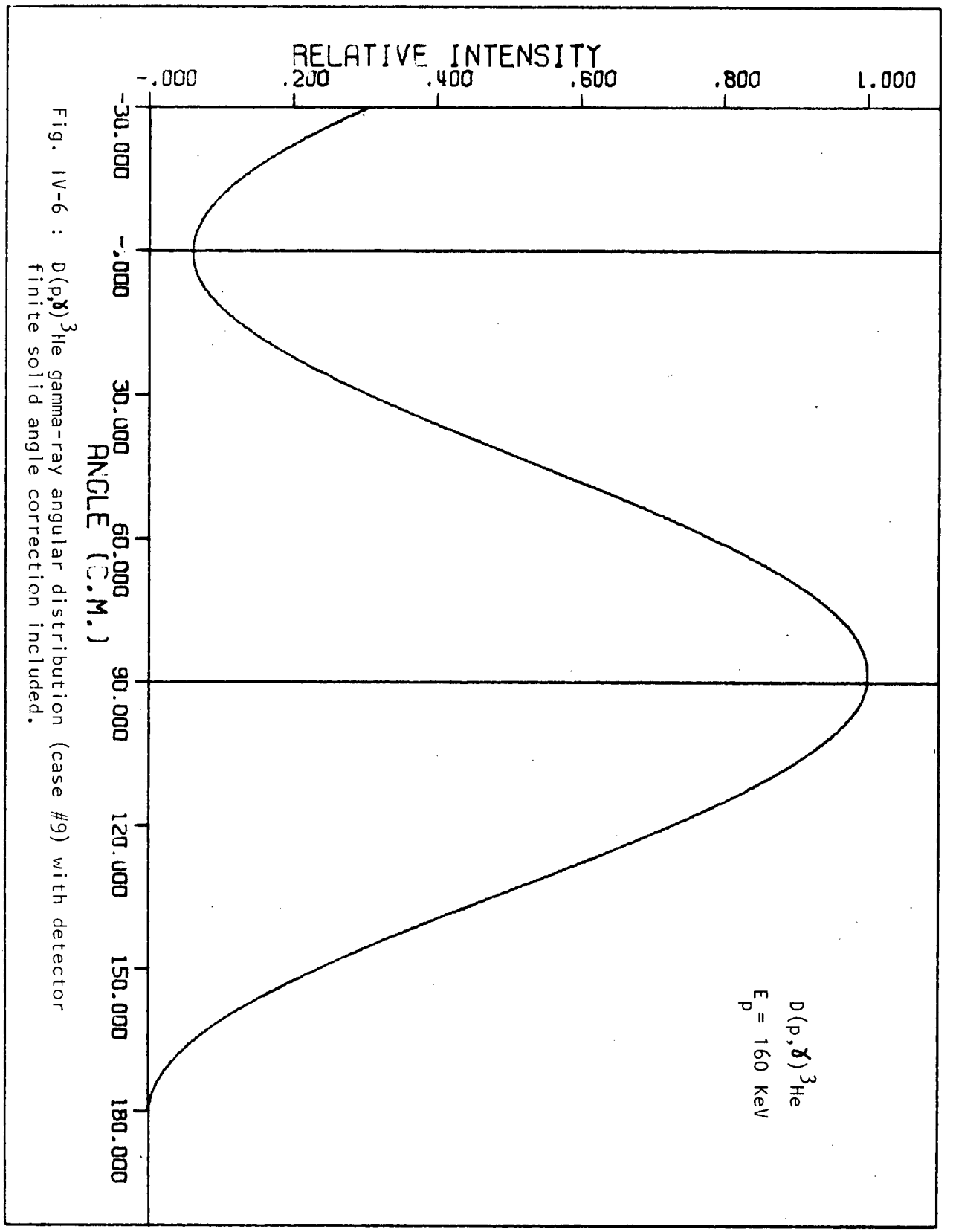

Fig. IV-6 : D(p,γ)^{3}He gamma-ray angular distribution (case #9) with detector finite solid angle correction included.

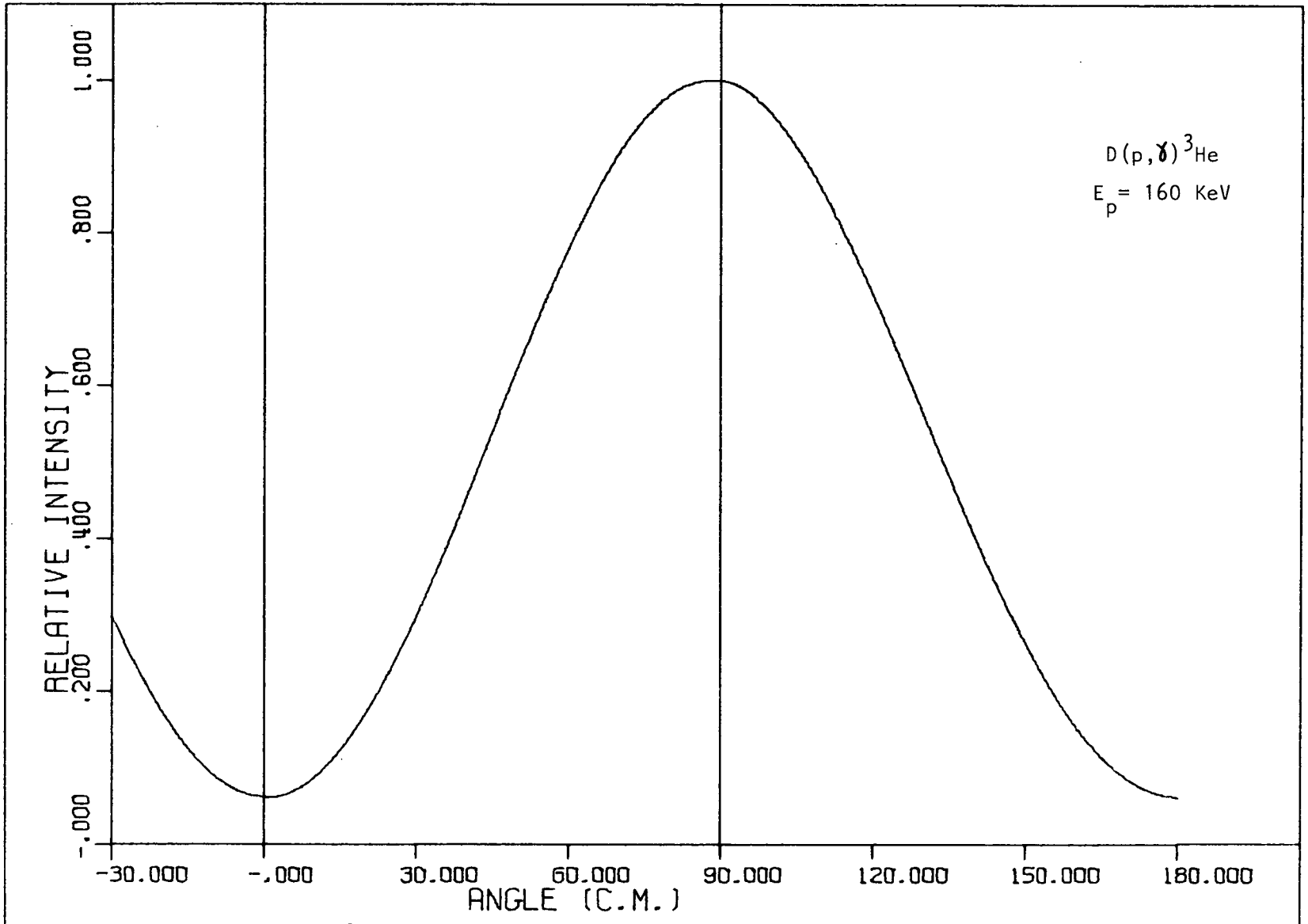

Fig. IV-7 : $D(p,\gamma)^3He$ gamma-ray angular distribution (case #10) with detector finite solid angle correction included.

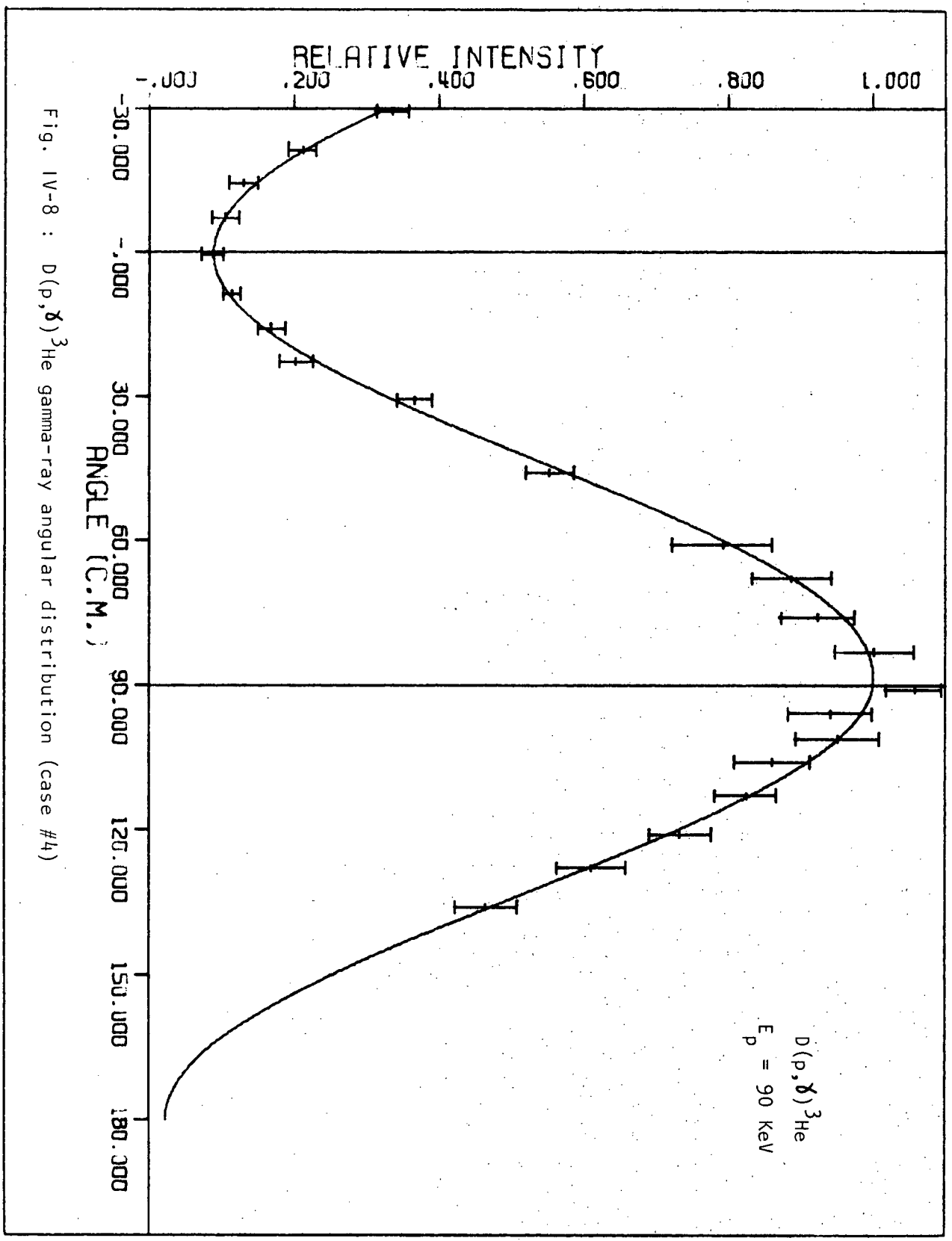

Fig. IV-8 : $D(p,\gamma)^3He$ gamma-ray angular distribution (case #4)

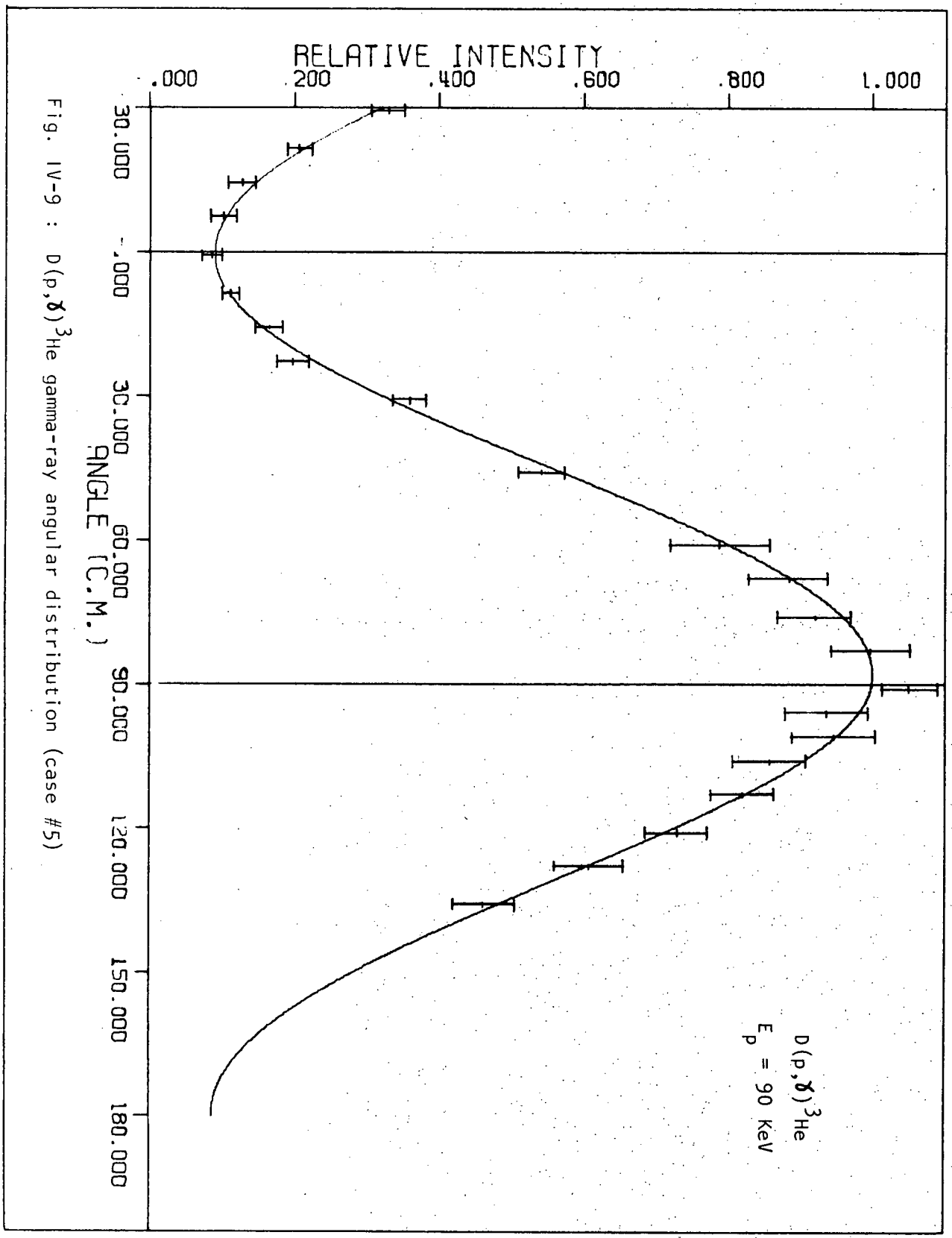

Fig. IV-9 : D(p,γ)^{3}He gamma-ray angular distribution (case #5)

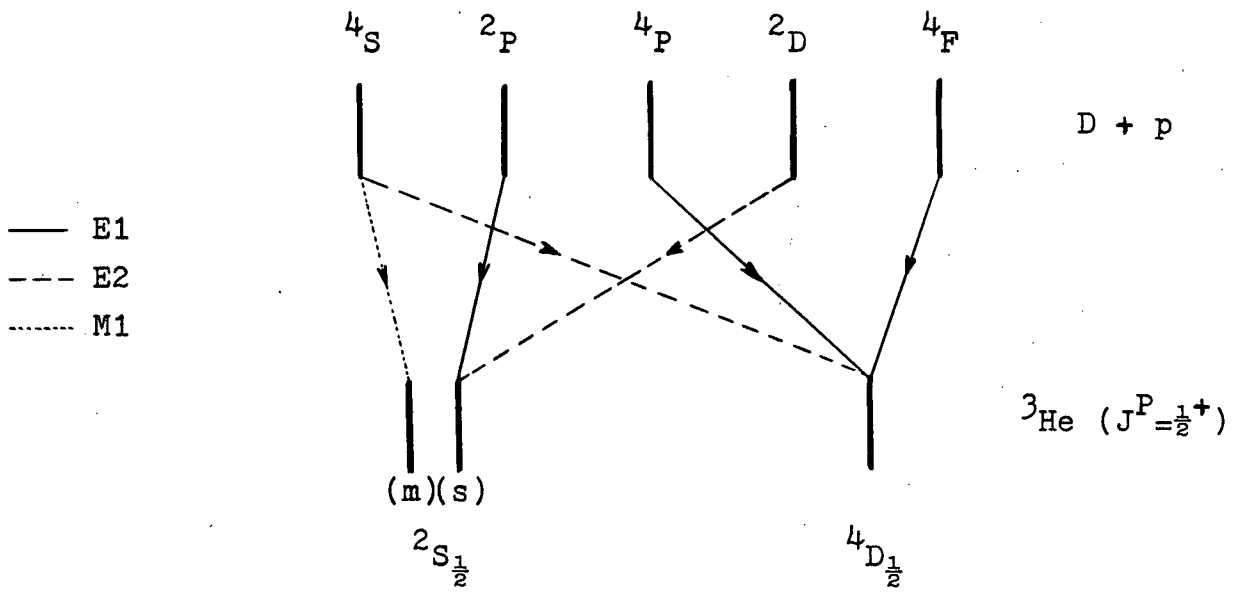

In the upper part of the figure the vertical lines represent the components that have been considered in the continuum state wave function of the D + p system. Similarly, the lower vertical lines represent the components that have been considered in the ground state wave function of the ^{3}He (D + p bound system).

The direct capture transitions between the continuum and bound states are summarized below where the form of the angular dependence of the differential cross section is indicated:

(1) $E1(^2P-^2S)$ $\quad \frac{d\sigma}{d\Omega} \sim \sin^2\theta$

(2) $E2(^2D-^2S)$ $\quad \frac{d\sigma}{d\Omega} \sim \sin^2 2\theta$

(3) $M1(^4S-^2S)$ $\quad$ isotropic

(4) $E1(^4P-^4D)$ $\quad \frac{d\sigma}{d\Omega} \sim \left(1 - \frac{1}{7}\cos^2\theta\right)$

(5) $E1(^4F-^4D)$ $\quad \frac{d\sigma}{d\Omega} \sim \left(1 - \frac{1}{2}\cos^2\theta\right)$

(6) $E2(^4S-^4D)$ $\quad$ isotropic

and the interferences:

(7) E1/E2 $(^2P-^2S/^2D-^2S)$ $\quad \frac{d\sigma}{d\Omega} \sim \sin\theta \sin 2\theta$

(8) E1/E1 $(^4P-^4D/^4F-^4D)$ $\quad \frac{d\sigma}{d\Omega} \sim P_2(\cos\theta)$

(9) E1/E2 $(^4P-^4D/^4S-^4D)$ $\quad \frac{d\sigma}{d\Omega} \sim P_1(\cos\theta)$

(10) E1/E2 $(^4F-^4D/^4S-^4D)$ $\quad \frac{d\sigma}{d\Omega} \sim P_3(\cos\theta)$

(11) E1/M1 $(^4P-^4D/^4S-^2S)$ $\quad$ zero

(12) E1/M1 $(^4F-^4D/^4S-^2S)$ $\quad$ zero

(13) E2/M1 $(^4S-^4D/^4S-^2S)$ $\quad$ zero

The differential cross section can be expanded in a Legendre polynomial series

$$\frac{d\sigma}{d\Omega} = \sum_{\ell=0}^{4} A_\ell P_\ell(\cos\theta)$$

where the transitions which contribute to the various Legendre

coefficients are shown below:

A_o $M1(^4S-^2S)$; $E1(^2P-^2S)$; $E1(^4P-^4D)$; $E1(^4F-^4D)$; $E2(^2D-^2S)$; $E2(^4S-^4D)$; $E1(^4P-^4D)/E1(^4F-^4D)$

A_1 $E1(^2P-^2S)/E2(^2D-^2S)$; $E1(^4P-^4D)/E2(^4S-^4D)$

A_2 $E1(^2P-^2S)$; $E2(^2D-^2S)$; $E1(^4P-^4D)$; $E1(^4F-^4D)$; $E1(^4P-^4D)/E1(^4F-^4D)$

A_3 $E1(^2P-^2S)/E2(^2D-^2S)$; $E1(^4F-^4D)/E2(^4S-^4D)$

A_4 $E2(^2D-^2S)$

After making a number of assumptions, which are discussed briefly below, about the relative amplitudes of various components in the wave functions, Donnelly calculated the cross sections for centre of mass energies between 16 KeV and 4 MeV. Approximate cross sections obtained by Donnelly for a centre of mass bombarding energy of 100 KeV for the different transitions are given below:

	Transition	$\sigma(\mu b)$
(1)	$E1(^2P-^2S)$	0.6
(2)	$E2(^2D-^2S)$	0.003
(3)	$M1(^4S-^2S)$	0.08
(4)	$E1(^4P-^4D)$	0.08
(5)	$E1(^4F-^4D)$	0.01
(6)	$E2(^4S-^4D)$	$< 10^{-6}$

Donnelly's model does not incorporate the complete three body symmetry properties of the wave function, however, he introduced some of these properties in an empirical way by including components of arbitrary amplitude for the ^4D state and the $^2S_{(m)}$ state of mixed symmetry in the ground state wave function, since these components are shown to be present for realistic nuclear forces (DE 60).

The ^4D state was introduced with an arbitrary probability P_D so that the ground state radial wave function was assumed to have the form

$$U(r) = \sqrt{1-P_D}\ \ U_S(r) + \sqrt{P_D}\ \ U_D(r)$$

where $U_S(r)$ and $U_D(r)$ are the radial functions for the ^2P and ^4D components each normalized to unity. In previous work (BA 67) it was shown that the calculated total cross section for the yield at 0^o fitted the rather limited experimental data from low energies up to 1.5 MeV with 1% ($P_D = 0.01$) ^4D state. This value was used in Donnelly's calculations.

For the ^4S continuum state the proton and deuteron have their spins aligned. Since the total wave function must be anti-symmetric and the spin function is symmetric, while the iso-spin function is of mixed symmetry, the spatial wave function of the ^4S state must be of mixed symmetry. Because the magnetic dipole operator is space-symmetric this transition can only proceed to the mixed symmetry spatial component in the ^2S ground

state of ^{3}He, thus the overall M1 transition is inhibited by selection rules. In computing the M1 cross section for the ^{4}S state to $^2S_{(m)}$ state of mixed symmetry it was assumed that the radial form of the $^2S_{(m)}$ state was the same as the radial form of the symmetric ^{2}S state. Further it was assumed to have an arbitrary amplitude which would need to be determined by experiment. Previous work (BA 67) has shown that a $^2S_{(m)}$ state amplitude of 0.33 times the ^{2}S state amplitude gives good agreement between theory and experiment for the low energy 0° cross section.

It is important to note here that the calculations of Donnelly and Bailey et. al. have been devised to give a reasonably good energy dependence for the cross sections, particularly at low energies. However, due to the approximations made the absolute values of the amplitudes of the $^2S_{(m)}$ and ^{4}D states contain arbitrary factors that make it unrealistic to expect them to be accurate or to agree with amplitudes obtained by other workers. The ^{4}D amplitude introduced here is smaller than the 4% usually found necessary to fit the magnetic moments of the three body nuclei (SP 50) (subject to considerable uncertainties due to the neglect of exchange moments). The $^2S_{(m)}$ state amplitude is much larger than the value required to fit electron scattering data (GI 67).

Table IV-2 shows a comparison between the experimental results described here for cases 5 and 10, for which it was assumed that $A_3 = -A_1$, and results obtained for Donnelly's

$\overline{E}_p$ (KeV)		A_1/A_o	A_2/A_o	A_3/A_o	A_4/A_o
$70^{+}_{-}20$	Exp. (case # 5)	0.06 ± 0.04	-0.93 ± 0.05	-0.06 ± 0.04	0.02 ± 0.05
	Theory	0.18	-0 84	-0.18	-0.007
$144^{+}_{-}16$	Exp. (case #10)	0.05 ± 0.02	-0.94 ± 0.02	-0.05 ± 0.02	0.03 ± 0.02
	Theory	0.15	-0.88	-0.15	-0.007

Table IV-2 : Comparison between present experimental results (case # 5 and case #10) and Donnelly's calculations.

calculations (DO 67).

As seen in Table IV-2 the theoretical values of A_1/A_o and A_3/A_o are equal and of opposite sign. In the theoretical calculation there are small contributions from interference terms involving the ^4D state which can produce a difference between A_3 and $-A_1$ however, the theory suggests that this difference is less than 0.1%. The analysis, case #9 (Table IV-1), of the experimental data suggests that there may be a small difference between A_3 and $-A_1$ but, it is at the limit of statistical significance. If we assume then that $A_3 = -A_1$ as was done for case #10 then the value of A_1/A_o which results is 0.05 ± 0.02, which is one third of the value given by the Donnelly calculation for this energy range. The A_1 (and A_3) terms arise from interference between $E2(^2D-^2S)$ and $E1(^2P-^2S)$ transitions and the calculated angular distribution coefficients depend on a model dependent ^2P phase shift which is not in agreement with the Christian and Gammel (CH 53) phase shift analysis of the low energy proton-deuteron scattering data. Furthermore, the disagreement noted here suggests that either one or both of the extrapolations of the phase shifts of ^2P and ^2D continuum wave functions to low energies may be significantly in error.

Although, the term A_2/A_o is, as far as the sign and order of magnitude concerned, in agreement with the theory, the difference between the experimental value and theoretical calculation is beyond the statistical error. This suggests that 1% ^4D state in the ground state wave function is too high since

the transitions involving the ^4D state contribute more strongly to A_o then to A_2 as can be seen from the angular distributions. Bailey (BA 67) has shown that the 0^o yield is very sensitive to the ^4D state probability and his tentative suggestion that this probability was 1%, was based on the analysis of data of low statistical accuracy. The data could be fitted equally well by a smaller ^4D state probability as suggested by the present results.

It is not surprising that the A_4/A_o term remains undefined since only the E2(^2D-^2S) transition can contribute to this term and it has a relatively low cross section at these energies.

The A_o coefficient is not defined by the present work since it requires the measurement of the absolute cross section which is the object of future work.

4.3. Future Work

As shown above the main contributions to the isotropic cross section are the M1(^4S-^2S) transition and the E1(^4P-^4D) term plus its interference with the smaller E1(^4F-^4D) transition involving the ^4D state. Both the $^2S_{(m)}$ and ^4D state probabilities are of considerable interest since they are related to spin dependent and non-central parts of the nucleon-nucleon force. It is not possible to separate the effects of these contributions by angular distribution measurements in a narrow energy range.

However, because these contributions have quite different energy dependence (DO 67) relative cross sections over a wide energy range, from 30 KeV to 3 MeV say, would provide a basis for separating the M1 and E1 cross sections. Furthermore, absolute cross sections would provide a more stringent test of any theoretical models for the amplitudes of the $^2S_{(m)}$ and ^4D states. In addition the cross section in the energy range from 1 KeV to 25 KeV is of interest in a number of astrophysical processes.

Absolute cross section measurements are to be done in the energy range from 50 KeV to 180 KeV using the low energy accelerator and these results will be combined with measurements at higher energies (400 KeV to 2 MeV) which are at the present time being carried out in this laboratory by G.M. Bailey and R. Helmer using the U.B.C. Van de Graaff accelerator.

In spite of improvements made in the deuterium targets, the deterioration continues to present a problem from the viewpoint of making accurate relative and absolute cross section measurements. One method that has been developed to partly alleviate this difficulty is to produce a target over the surface of a plate which is rotated rapidly in front of the beam so no part of the target is continuously exposed to the beam.

A rotating target holder was developed by G.M. Bailey and the author. It consists of a flat copper disc 5" in diameter and 1/16" thick mounted inside of a vacuum chamber in such a way

that it can be rotated externally by means of an electric motor. The speed at which the disc rotates can be varied in a continuous way up to 600 rpm.

A simplified schematic diagram is shown in Fig. IV-10. The water-cooled disc can be moved up and down with respect to the beam and can also be placed at different angles with respect to the incoming beam.

This target holder has already been tested (BA 68). Deuterated polyethylene was deposited over the area of the disc with a thickness of 100 $\mu g/cm^2$. An 800 KeV proton beam of approximately 5 μA from the Van de Graaff accelerator was used. The spot on the target was approximately 6 mm in diameter.

The test was carried out over a 10 hour period. Although during the first two and a half hours or so there was about 40% decrease in the yield the rate of deterioration in the seven and a half subsequent hours was found to be less than 15%.

For relative cross section measurements the initial loss of target material presents no major problems because one can wait until the target is stabilized to initiate the measurements. For these measurements it is not necessary to know the actual number of deuterium atoms per cm^2 as long as the target thickness is below a chosen value.

For the absolute cross section measurements the sit-

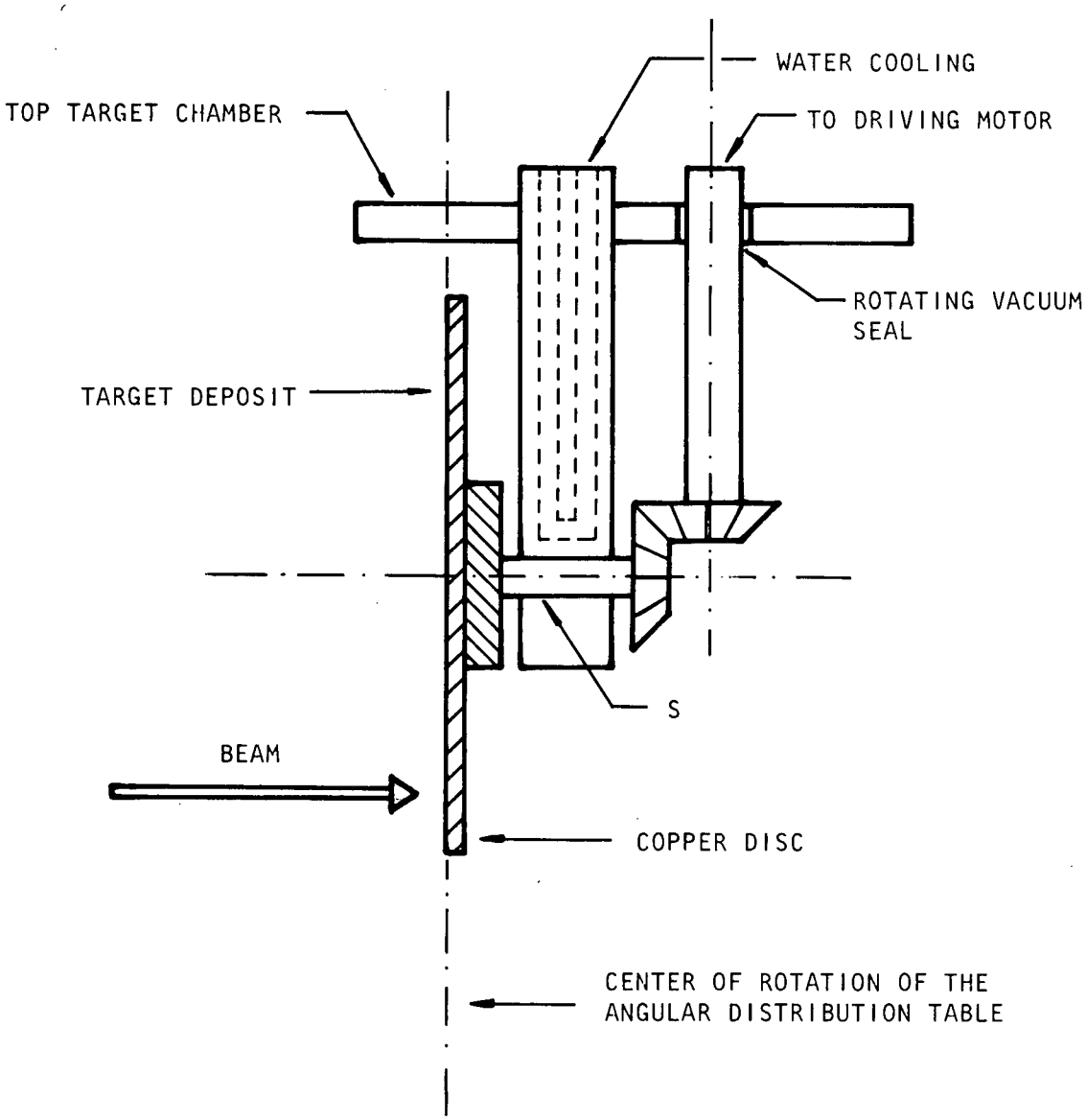

Fig. IV-10 : Rotating target holder. The copper disc is cooled by conduction through the axis S.

uation is different because one cannot use the initial thickness as determined by weight to estimate the number of deuterium atoms per cm^2.

The target thickness after the equilibrium is reached can be estimated by measuring the neutron flux produced when a deuteron beam is used instead of a proton beam. From the knowledge of the $D(d,n)^3He$ cross section, the total charge collected by the target and the efficiency of the neutron detector one can determine the amount of D present in the target.

These measurements could be checked as follows. Starting with a fresh target the neutron flux is measured using a D beam of say 50 nA. It is believed that the target will not deteriorate using this low beam current. Therefore one could compare the amount of deuterium as determined by the neutron flux with the amount of deuterium as determined by the weight of the polyethylene layer.

Plans are underway to carry out the target testing with the objective of making the absolute cross section measurements in the near future.

When the absolute cross sections have been measured over a range of energies it should be possible to make better estimates of the amplitudes of the $^2S_{(m)}$ and ^4D components of the three body wave function. With continuing development on the theoretical side it should then be possible to relate these

amplitudes to spin-dependent and tensor parts of the two-nucleon force.

BIBLIOGRAPHY

AJ 59 F. Ajzenberg-Selove and T. Lauritsen, "Energy Levels in Light Nuclei", North-Holland Publishing Co. Amsterdam, (1959).

AR 54 W.R. Arnold, J.A. Phillips, G.A. Sawyer, E.J. Stovall Jr. and J.L. Tuck, Phys. Rev., 93 (1954) 483.

AR 56 M. von Ardenne, "Tabellen der Elektronenphysik Ionenphysik und Übermikroskopie", Deutscher Verlag der Wissenschaften, Berlin, (1956).

BA 50 C.L. Bailey and W.R. Stratton, Phys. Rev., 77 (1950) 194.

BA 67 G.M. Bailey, G.M. Griffiths and T.W. Donnelly, Phys. Lett., 24 (1967) 222.

BA 68 G.M. Bailey, private communication, (1968).

CH 53 R.S. Christian and J.L. Gammel, Phys. Rev., 91 (1953) 89.

CR 51 W.G. Cross, Rev. Sci. Instrum., 22 (1951) 717.

CR 56 D.S. Craig, W.G. Cross and R.G. Jarvis, Phys. Rev., 103 (1956) 1414.

CU 39 S.C. Curran and J. Strothers, Proc. Roy Soc., 172 (1939) 72.

DA 67 R.S. Davis, Ph.D. Thesis, Univiersity of British Columbia (1967).

DE 58 G. Derrick and J.M. Blatt, Nucl. Phys., 8 (1958) 310.

DE 60 G. Derrick, Nucl. Phys., 16 (1960) 405.

DO 67 T.W. Donnelly, Ph.D. Thesis, University of British Columbia (1967).

DO 67A T.W. Donnelly, private communication, (1968).

EI 63 U. Eichmann, Z. Physik 175 (1963) 115.

EL 53 M.M. Elkind, Rev. Sci. Instrum., 24 (1953) 129.

FA 65 W.R. Falk, Ph.D. Thesis, University of British Columbia (1965).

FO 49 W.A. Fowler, C.C. Lauritsen and A.V. Tollestrup, Phys. Rev., 76 (1949) 1767.

GI 67 B.F. Gibson, Nucl. Phys. B2 (1967) 501.

GR 54 P.J. Grant, F.C. Flack, J.G. Rutherglen and W.M. Deuchars, Proc. Phys. Soc., A67 (1954) 751.

GR 55 G.M. Griffiths and J.B. Warren, Proc. Phys. Soc., 68 (1955) 781.

GR 57 G.W. Grodstein, "X-ray attenuation coefficients from 10 KeV to 100 MeV", National Bureau of Standards-Circular 583, Washington, (1957).

GR 61 A.G. Gregory, Nucl. Phys., 23 (1961) 518.

GR 62 G.M. Griffiths, E.A. Larson and L.P. Robertson, Can. J. Phys. 40 (1962) 402.

GR 63 G.M. Griffiths, M. Lal and C.D. Scarfe, Can. J. Phys., 41 (1963) 724.

HA 50 R.N. Hall and W.A. Fowler, Phys. Rev., 77 (1950) 197.

HE 68 R.L. Helmer, private communication, (1968).

HU 52 T.P. Hubbard, E.B. Nelson and J.A. Jacobs, Phys. Rev., 87 (1952) 378.

JO 65 G. Jones, private communication, (1965).

KE 51 B.D. Kern, C.D. Moak, W.M. Good and G.P. Robinson, Phys. Rev., 83 (1951) 211.

LA 57 W.A.S. Lamb and R.E. Hester, Phys. Rev., 107 (1957) 550.

MC 68 R.C. McFadden, private communication, (1968).

MO 65 N.F. Mott and H.S.W. Massey, "The Theory of Atomic Collisions", Clarendon Press, Oxford, (1965).

OR 58 J. Orear, "Notes on Statistics for Physicists", UCRL-8417 Report, Berkeley, California, (1958).

OR 67 P.H.R. Orth, Ph.D. Thesis, Univiersity of British Columbia, (1967).

OR 67A P.H.R. Orth, private communication, (1967).

RO 53 M.E. Rose, Phys. Rev., 91 (1953) 610.

SA 55 R.G. Sachs, "Nuclear Theory", Addison-Wesley, Cambridge, Mass., (1955).

SA 64 A. Savitzky and M.J.E. Golay, Anal. Chem., 36 (1964) 1627.

SE 53 E. Segre, "Experimental Nuclear Physics - Volume I", John Wiley & Sons, New York, (1953).

SI 59 P.P. Singh, G.M. Griffiths, Y.I. Ssu and J.B. Warren, Can. J. Phys., 37 (1959) 866.

SM 61 A.J. Stewart Smith, M.Sc. Thesis, University of British Columbia, (1961).

SP 50 L. Spruch, Phys. Rev., 80 (1950) 372.

TR 67 G.E. Tripard and B.L. White, Rev. Sci. Instrum., 38 (1967) 435.

VE 50 M. Verde, Helv. Phys., Acta 23 (1950) 453.

WH 58 W. Whaling, Handbuch der Physik, 34 (1958) 193.

WH 62 B.L. White, L.P. Robertson, K.K. Erdman and J.R. MacDonald, Rev. Sci. Instrum., 33 (1962) 1111.

WI 39 E.J. Williams, Proc. Roy. Soc., 169 (1939) 531.

WI 52 D.H. Wilkinson, Phil. Mag., 43 (1952) 659.

WO 52 E.J. Woodbury and W.A. Fowler, Phys. Rev., 85 (1952) 51.

WO 66 W. Wölfli, R. Bosch, J. Lang, R. Müller and P. Marmier, Phys. Lett., 22 (1966) 75.

YU 67 H.P. Yule, Nucl. Instr. and Meth., 54 (1967) 61.

APPENDIX A

THE ANGULAR DISTRIBUTION OF THE 11.7 MeV GAMMA RAYS FROM THE REACTION $^{11}B(p,\gamma)^{12}C$

As a check on the procedure followed in the determination of the angular distribution of the reaction $D(p,\gamma)^3He$, the angular distribution of the 11.7 MeV gamma-rays from the reaction $^{11}B(p,\gamma)^{12}C$ was measured and the result compared with measurements from previous work.

This measurement checks the behavior of the angular distribution table and the corrections due to the absorption in the target holder as well as the iterative least squares method used in the analysis of the data.

The reaction $^{11}B(p,\gamma)^{12}C$ has a sharp resonance (Γ = 7 KeV) at a proton bombarding energy of 163 KeV. The level in ^{12}C formed at this resonance has an excitation energy of 16.11 MeV and decays by either alpha-particle or gamma-ray emission. The decay scheme is shown in Fig. A-1 which indicates only the levels of interest.

A ^{11}B target 25 $\mu g/cm^2$ thick, deposited on a 0.010 inch thick copper backing (obtained from the Atomic Energy Research Establishment, Harwell, England) was bombarded with 100 μA of 170 KeV protons. The conditions of the beam on the target were similar to the $D(p,\gamma)^3He$ runs. The target was mounted on target holder "TA" (Fig. II-3) and the detector target arrange-

ment used is shown in Fig. III-1. The same target was used in both configurations. At E_p = 170 KeV with the target placed at 45° with respect to the incoming beam, the energy loss by the beam in the target was about 21 KeV and the R.M.S. multiple scattering angle was less than 1.1°.

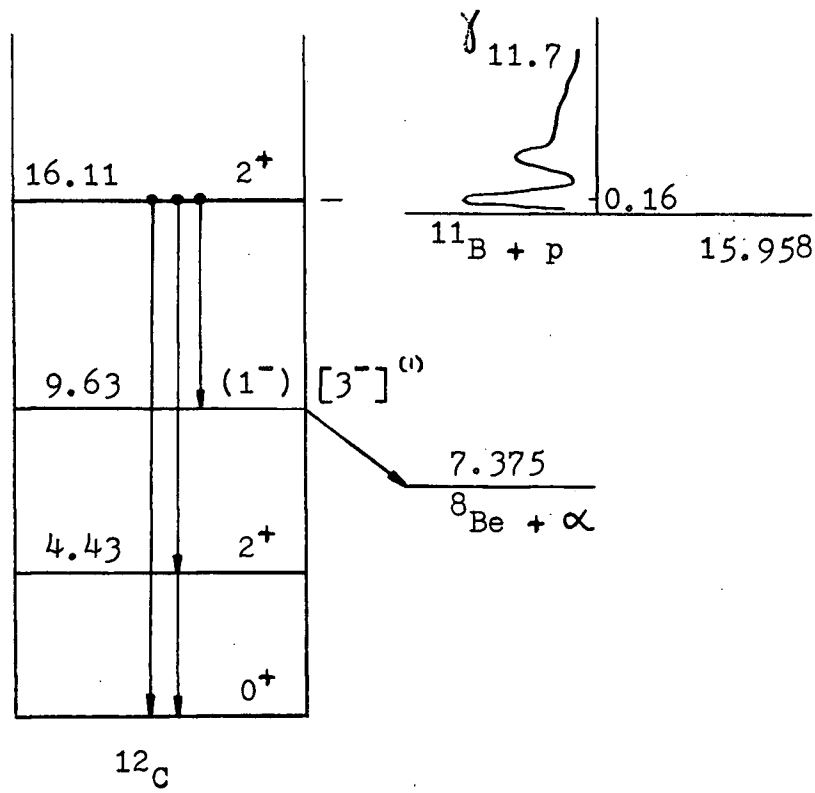

Fig. A-1 : Some energy levels in the ^{12}C nucleus from Ajzenberg-Selove and Lauritsen, (AJ 59) . The 6.5 MeV transition to the 9.63 MeV level leads to the break-up of the $^{12}C^*$ into an alpha particle and ^8Be as shown.
(1) Assignment given by A.G. Gregory (GR 61).

A typical gamma-ray spectrum taken with the detector #1 at $\theta_1 = 135°$ is shown in Fig. A-2 where the 6.5 MeV gamma-ray peak from the competing reaction $^{11}B(p,\gamma\alpha)^8Be$ is indicated. Fig. A-3 shows a typical background spectrum for detector #1.

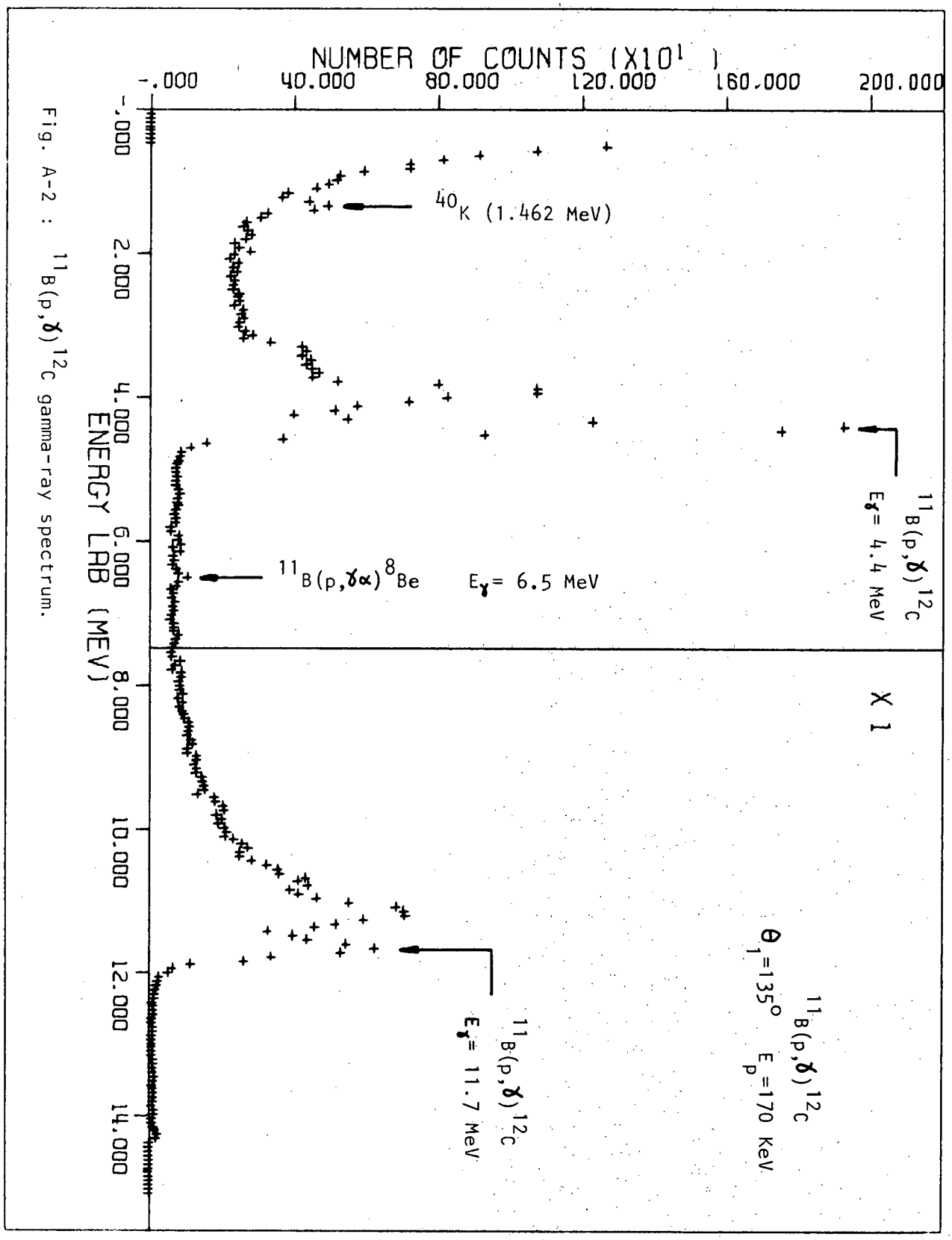

Fig. A-2 : $^{11}B(p,\gamma)^{12}C$ gamma-ray spectrum.

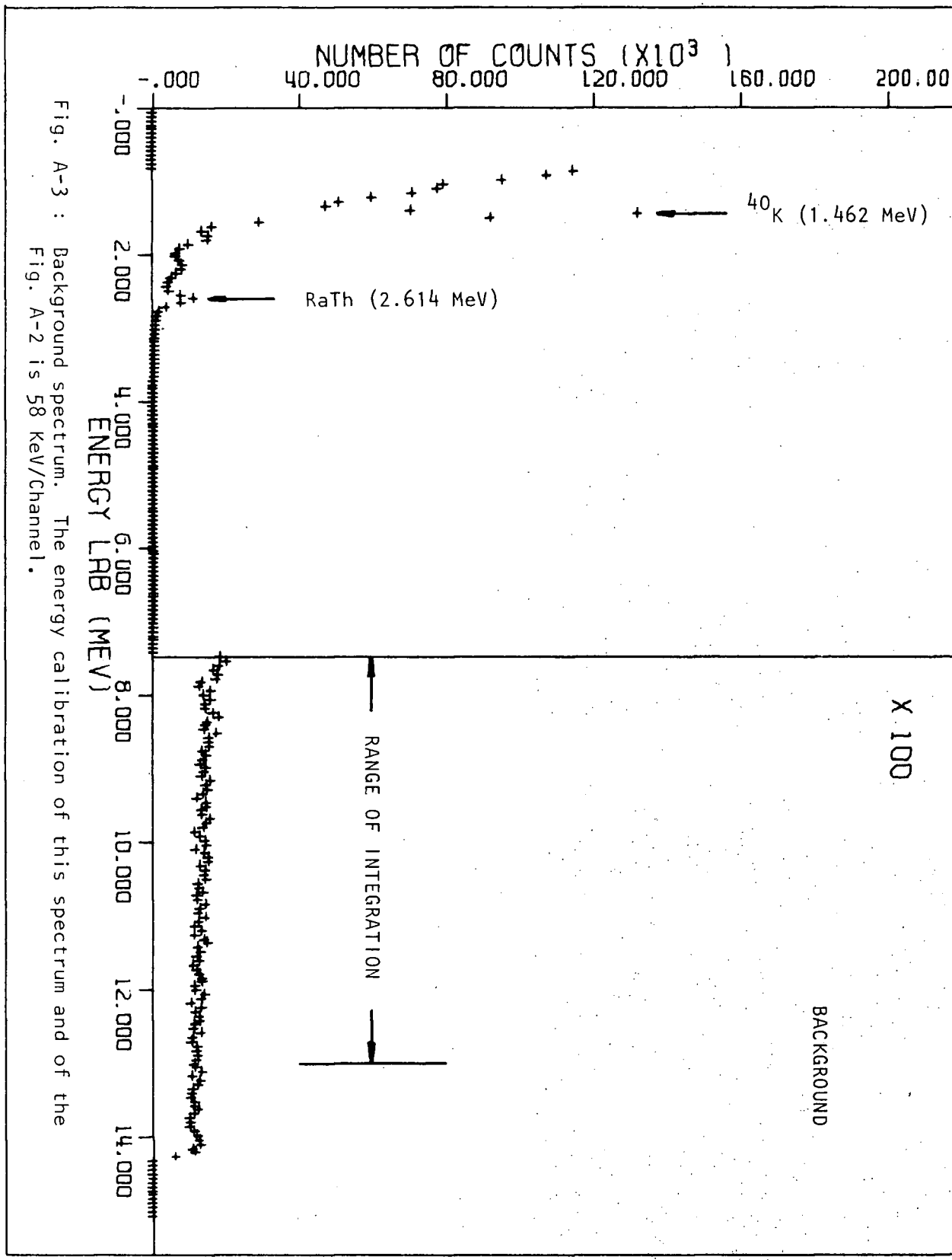

Fig. A-3 : Background spectrum. The energy calibration of this spectrum and of the Fig. A-2 is 58 KeV/Channel.

The spectra were analyzed following the procedure described in Chapter III. Here, however, the spectra were integrated from 7.5 MeV to 13 MeV covering the 11.7 MeV gamma-ray peak. The lower limit was chosen to be above the 6.5 MeV peak and below the 16.11 MeV peak which is off the curve shown in Fig. A-2. The results are summarized in Table A-1 using the same heading as described in Chapter III. The absorption coefficients used in the correction due to the target holder absorption are shown in Table G-1.

Although the intensity ratio of the 16.1 MeV to the 11.7 MeV gamma-rays is about 3.3% (CR 56) the overall contribution of the 16.1 MeV gamma-rays to the energy range counted for angular distribution measurement of the 11.7 MeV gamma-rays is less than 0.3% and was disregarded.

The experimental data were fitted to the following function:

$$W(\theta) = \left[\sum_{\ell=0}^{4} B_\ell P_\ell \right] (1 + \varepsilon K) \qquad (A - 1)$$

with

$$\varepsilon = \begin{cases} 0 & -45^\circ \leq \theta \leq 50^\circ \\ 1 & 60^\circ \leq \theta \leq 135^\circ \end{cases}$$

where $P_1 \equiv P_1 \cos(\theta+\theta_o)$ are the Legendre polynomials and K and θ_o the parameters defined in Chapter III. The least squares fitting procedure outlined in Chapter III was followed and the

i	θ_1	A	θ_2	B	T(sec)	C	D	E	F	G	$_G\sigma^2$	H	$_H\sigma^2$
0	----	17811	----	16767	50400	----	----	----	----	----	----	----	----
1	-45	15638	-115	15844	180	64	60	15574	15784	15574	31064	16888	36526
2	-40	22048	-115	22313	300	106	100	21942	22213	15591	22124	16802	25694
3	-30	15486	-115	15071	300	106	100	15379	14971	16215	34894	17323	39828
4	-20	17728	-115	16759	180	64	60	17664	16700	16696	32589	17745	36813
5	-10	23705	-115	22433	300	106	100	23599	22333	16678	24352	17677	27355
6	0	18303	-115	16790	300	106	100	18197	16690	17210	34224	18224	38377
7	10	21335	-115	19936	300	106	100	21229	19836	16893	27969	17904	31418
8	20	14098	-115	13533	180	64	60	14034	13473	16441	39797	17474	44956
9	30	12723	-115	12566	300	106	100	12616	12466	15974	41030	17066	46832
10	40	17582	-115	17674	300	106	100	17475	17574	15695	28279	16913	32840
11	50	14213	-115	14768	180	64	60	14149	14708	15185	32110	16600	38372
12	45	18955	-90	16434	240	85	80	18870	16354	18870	40836	----	----
13	60	13536	-90	12264	240	85	80	13451	12184	18055	50516	----	----
14	75	45933	-90	43016	480	170	160	45763	42857	17464	13832	----	----
15	90	15933	-90	15301	240	85	80	15848	15221	17028	37543	----	----
16	105	16050	-90	14959	240	85	80	15965	14878	17548	40198	----	----
17	120	16752	-90	15289	240	85	80	16667	15209	17922	40602	----	----
18	135	17050	-90	15011	240	85	80	16965	14931	18582	43707	----	----

Table A-1 : $^{11}B(p,\gamma)^{12}C$ gamma-ray angular distribution data of the E_γ=11.7 MeV γ-ray at E_p=170 KeV

results are summarized in Table A-2. From the results of previous workers the angular distribution has the form $(a + b \cos^2\theta)$. The data was fitted to equation (A-1) in which the parameters B_1, B_3, and B_4 were set equal to zero. The result of this is shown in row 2, of Table A-2.

In addition, the experimental data were also fitted to the same function (A-1) including the P_1 term. Although no P_1 term was expected, a term of this form was included in the analysis as a check on the alignment and the fitting procedure. The results of this fitting are shown in row 1, of Table A-2; clearly the coefficient B_1 is undefined with an error greater than 100%. The χ^2 test also indicates that a good fit is obtained without a P_1 term.

The values obtained for θ_o are also undefined. This is to be expected since the angular distribution is rather flat and the accuracy of zeroing the angle scale was smaller than the $\Delta\theta_o$ which results from the measurement. The fit obtained for an angular distribution of the form $B_oP_o + B_2P_2$ is shown in Fig. A-4.

The angular distribution coefficients expressed in terms of $F_1 = E(A_1/A_o)$, following the procedure outlined in Chapter IV, are shown in Table A-4. The corrected angular distribution is shown in Fig. A-5. The calculated smoothing factors Q_1 for 11.7 MeV gamma-rays are shown in Table A-3.

	B_o	ΔB_o	B_1	ΔB_1	B_2	ΔB_2	$\theta_{(rad)}^{o}$	$\Delta\theta_{(rad)}^{o}$	K	ΔK	χ^2	ν	p	E_p (KeV)
# 1	16252	196	12	194	1611	156	0.007	0.030	0.117	0.016	9.43	12	0.67	170
# 2	16261	112	0	0	1612	155	0.006	0.025	0.117	0.011	9.43	13	0.74	

Table A-2 : $^{11}B(p,\gamma)^{12}C$ angular distribution least squares fit parameters and Chi-squared test.

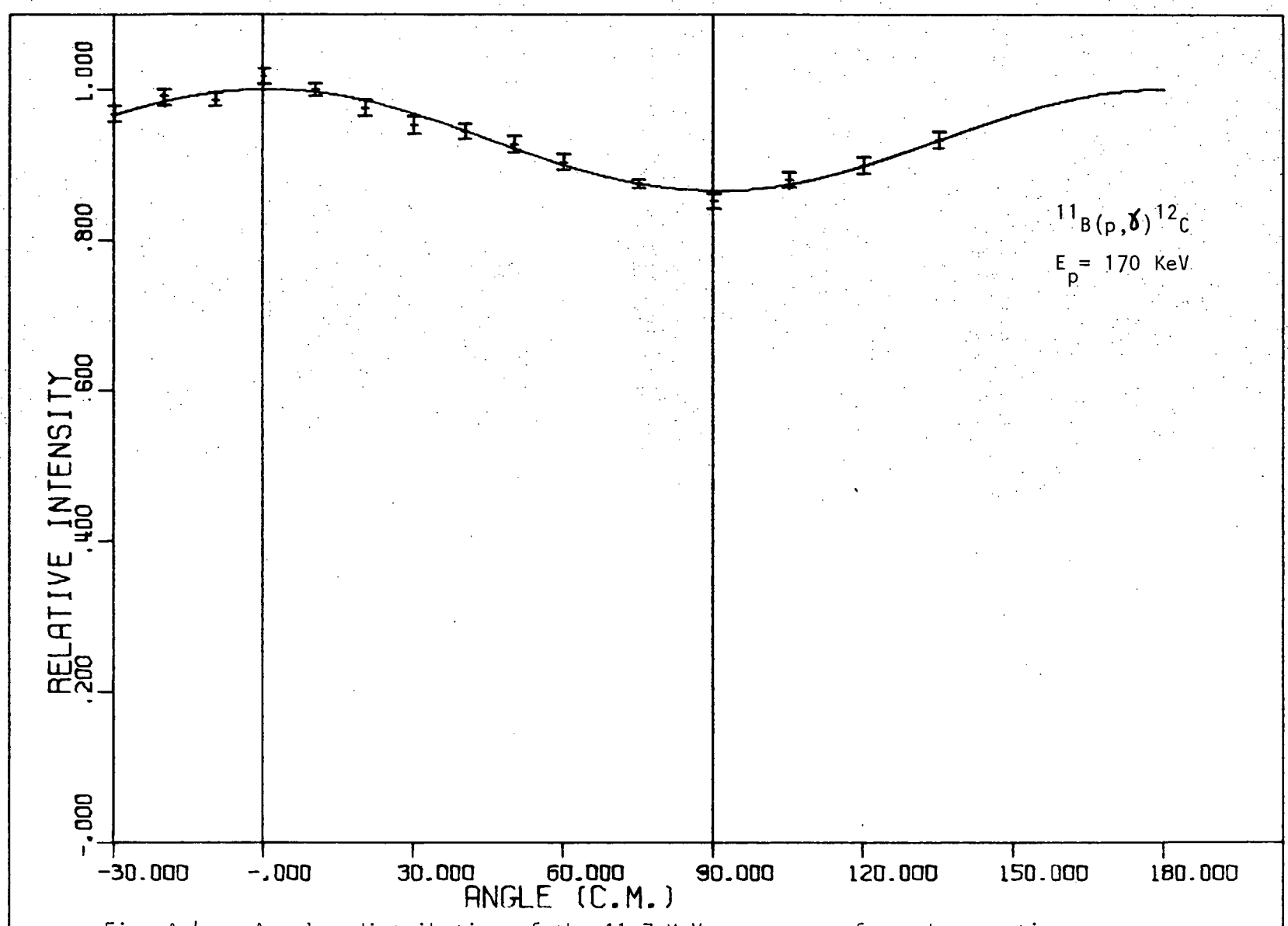

Fig. A-4 : Angular distribution of the 11.7 MeV gamma-rays from the reaction $^{11}B(p,\gamma)^{12}C$ at E_p = 170 KeV (case #2)

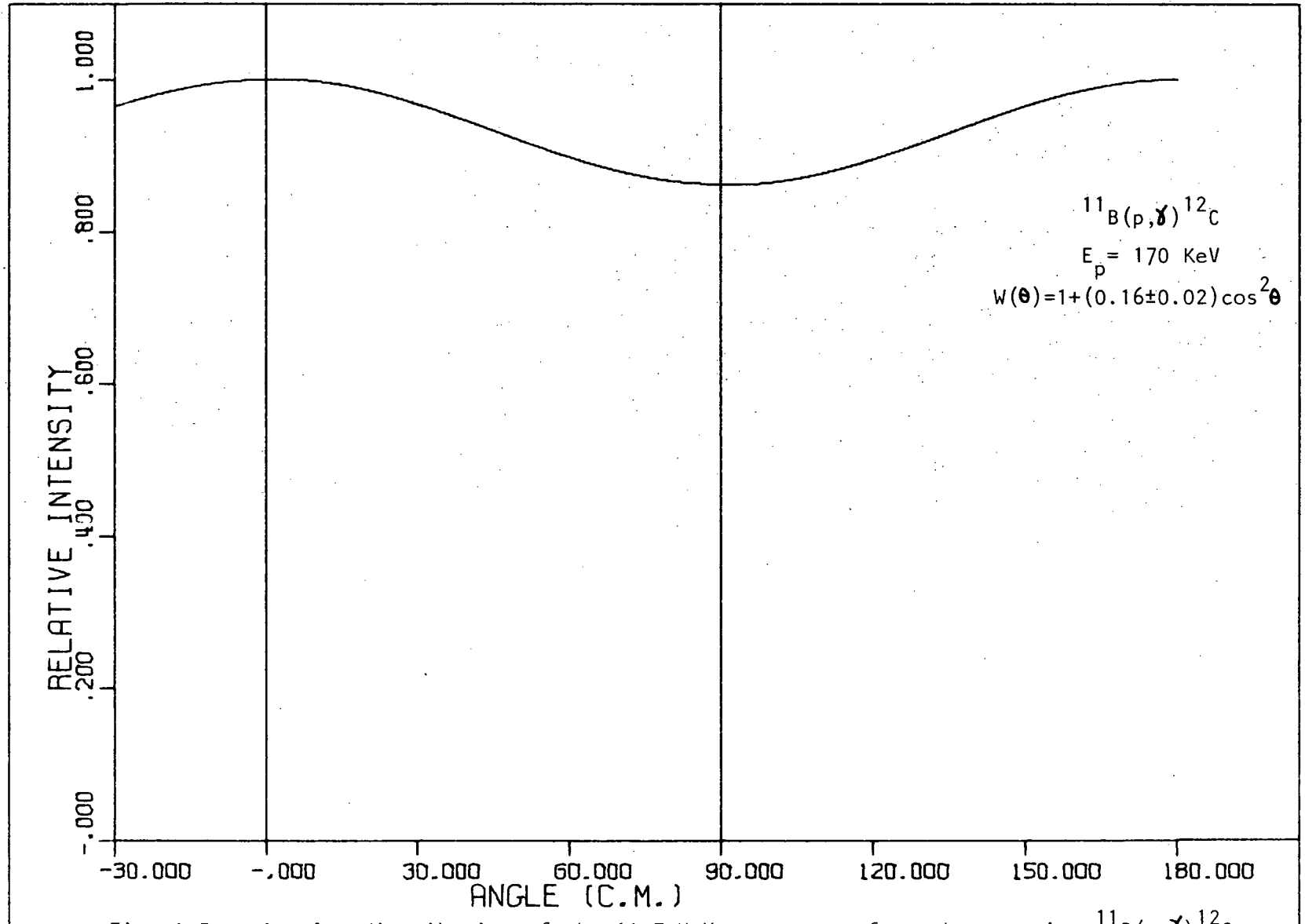

Fig. A-5 : Angular distribution of the 11.7 MeV gamma-rays from the reaction $^{11}B(p,\gamma)^{12}C$ at E_p = 170 KeV (case #2) with detector finite solid angle correction included.

Table A-3 : Smoothing factors calculated at E_γ = 11.7 MeV for the detector geometry shown in Fig. II-6.

l	0	1	2
Q_l	1.00000	0.98860	0.96606

Table A-4 : Legendre polynomial coefficients corrected for finite solid angle of the detector. F_1 is the expectation value of A_1/A_o $\left[F_1 = E(A_1/A_o)\right]$ and P the Chi-squared test result as defined in the text.

	F_1	ΔF_1	η_1	F_2	ΔF_2	η_2	P	E_p (KeV)
#1	0.001	0.012	1390	0.103	0.011	10.2	67	170
#2	0	0	0	0.103	0.010	10.2	74	

In order to compare the result obtained here with the results of other workers, the angular distribution was expressed in terms of $a(1+b/a\ \cos^2\theta)$ with the result shown below:

Previous Work

(KE 51) $W(\theta) = 1 + (0.15 \pm 0.03)\ \cos^2\theta$ E_p = 170 KeV

(HU 52) $W(\theta) = 1 + (0.23 \pm 0.04)\ \cos^2\theta$ E_p = 170 KeV

(GR 54) $W(\theta) = 1 + (0.26 \pm 0.01)\ \cos^2\theta$ E_p = 175 KeV

(CR 56) $I_{0^o}/I_{90^o} = 1.18 \pm 0.02$ E_p = 168 KeV

Present Work

$W(\theta) = 1 + (0.16 \pm 0.02)\ \cos^2\theta$ E_p = 170 KeV

The result of this experiment is in reasonable agreement with previous measurements except for the results of Grant et. al. (GR 54).

APPENDIX B

THE ACCELERATOR AND MAGNETIC ANALYZER

B.1. The Accelerator

The $D(p,\gamma)^3He$ measurements were made using a high current accelerator constructed by the author and based on an ORTEC duoplasmatron ion source. A brief description of the apparatus and its main characteristics is given below.

B.1.1. The Ion Source and Einzel Lens

The ion source, a modified Von Ardenne (AR 56) duoplasmatron, and Einzel lens are shown in Fig. B-1. The source system (ORTEC Model 504) consists of the duoplasmatron (Model 350), the Einzel lens and the power supplies and controls to operate both. The system was mounted in a aluminum box supported on insulating posts so that its potential could be changed with respect to ground by an external 150 KV power supply.

In order to obtain a large ion current from the duoplasmatron source the pressure in the arc chamber has to be quite high, 0.2 mm of Hg. On the other hand the beam must be injected into a high vacuum region which means that the extraction canal between the two regions must be of small diameter. In order to get a large beam from this small hole the duoplasmatron concentrates a small dense plasma at the exit hole, which is 0.008" in diameter, by means of electric and magnetic fields. The coil C produces a magnetic field between the intermediate electrode IE

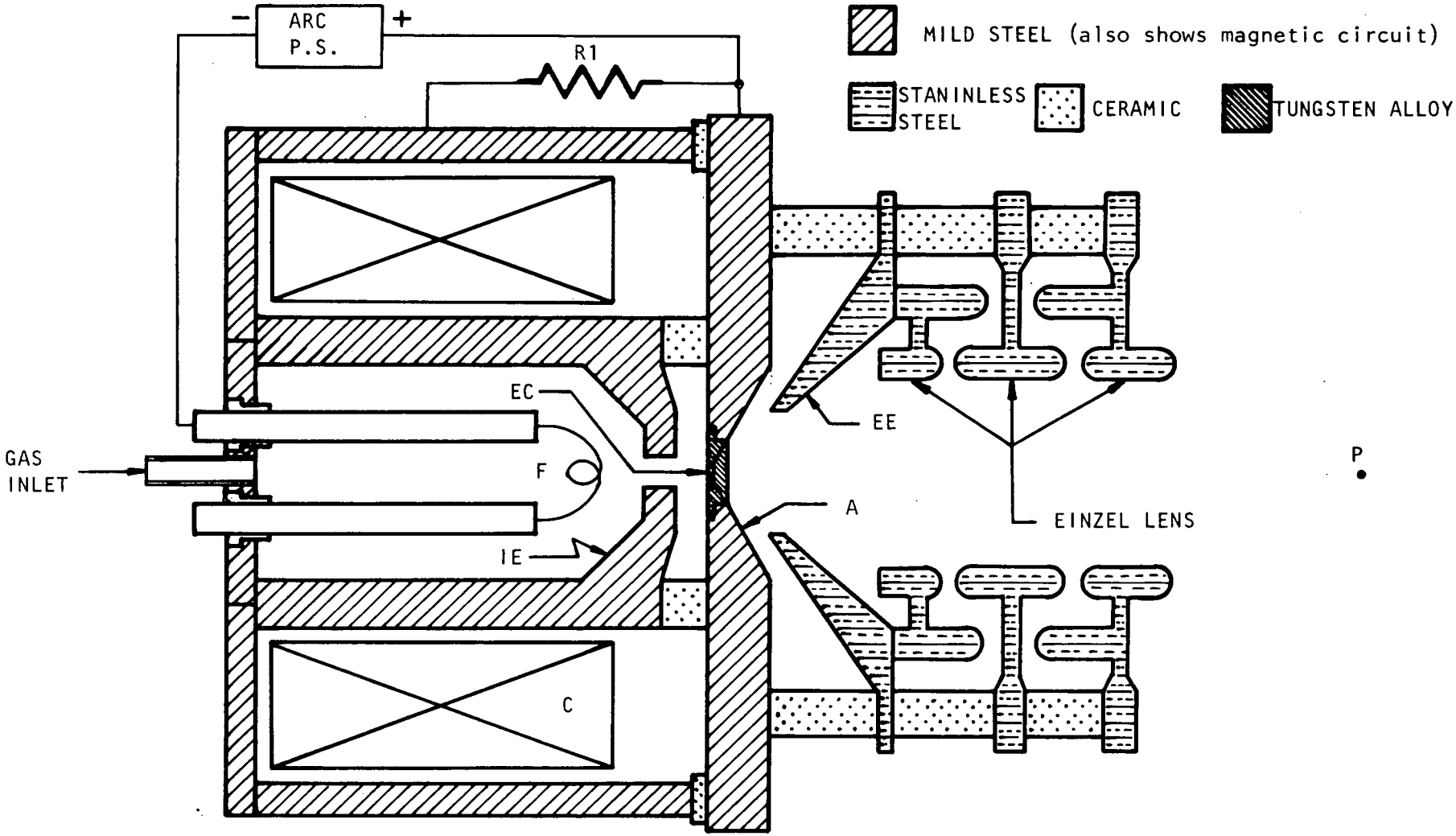

Fig. B-1 : Duoplasmatron ion source and Einzel lens system. This is not the actual schematic view but a simplified version.

and the anode A. This combined with the electric field between IE and A tends to draw a column of plasma from the arc chamber to the tungsten alloy extractor canal EC in the anode. Positive ions are drawn from the plasma (on the opposite side of the anode to the arc chamber) by the electric field between the extractor electrode EE and the anode A.

Because of the low initial kinetic energy and high ion density of the beam leaving the extraction region there is a tendency for the beam to diverge rapidly due to space charge effects. To reduce this "blow-up" effect and minimize the loss of beam to the extractor electrode the extraction voltage needs to be relatively high, that is approximately 10 KV or more. The Einzel lens then focusses the diverging beam to a point P just beyond the lens. The beam is then suitable for injection into the accelerating tube.

On starting the discharge in the arc chamber, the arc power supply provides approximately 350 Volts between the anode and the filament. Before the arc strikes a small electron current from the hot filament flows to the intermediate electrode and returns to the arc supply through R1. Most of the arc supply voltage appears between the intermediate electrode and the filament and this starts the arc which in turn makes a large increase in the current through R1. This causes the potential of IE to fall towards the filament voltage and a dynamic equilibrium is reached causing most of the current from the filament to flow to the anode.

The arc current, which tends to vary with the gas flow or with the magnetic field, is kept constant by means of a current regulated power supply. The initial 350 V potential drops to approximately 80 V under normal operating conditions.

The platinum gauze filament is initially coated with a suspension of $CaCO_3$. This carbonate is converted to the oxide by approximately twenty four hours of filament heating under vacuum.

A thermal leak (WH 62) is used to control the flow of gas from a high pressure storage bottle to the ionization chamber.

Heat is extracted from the magnet coils and the filament by a liquid coolant circulating around the coils. FREON 113 coolant flows in a closed circuit consisting of a pump, a water-cooled heat exchanger and a reservoir. The coolant also removes heat from the whole high voltage terminal. A cut-off switch removes all power from the source if the coolant pressure or flow rate fall below preset values.

B.1.2. The Accelerating Tube

The ion source Einzel lens system was coupled directly to an accelerating tube. The purpose of the tube is to convert a generally divergent low energy beam into a well collimated higher energy beam. Fig. B-2 shows a beam diverging from P and travelling through a zero-field region until it reaches the

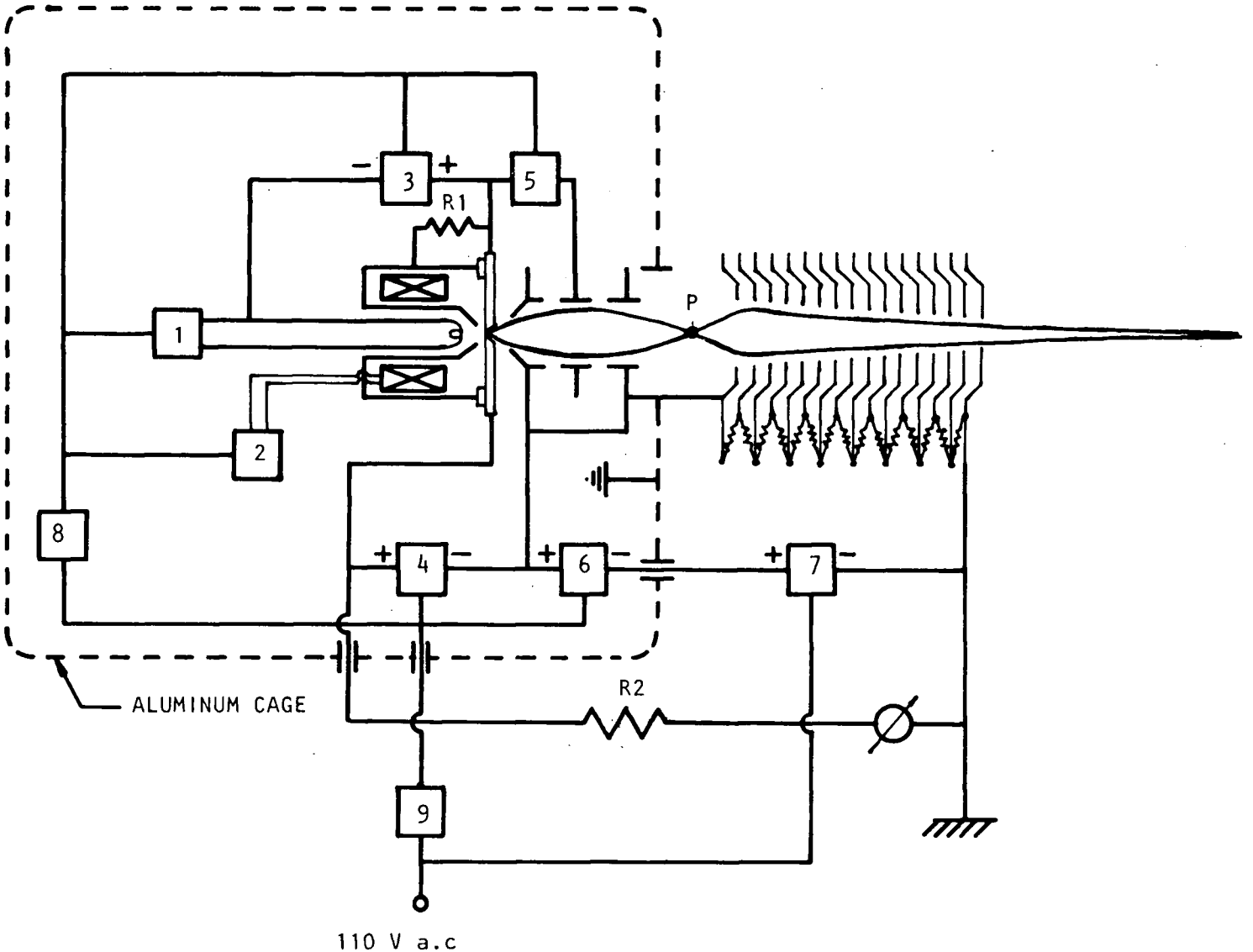

Fig. B-2 : Schematic diagram of the accelerator showing the beam trajectory. The electronic units shown in this diagram by the numbered squared boxes are listed in Table B-1.

first electrode of the tube where it is converged. The beam then travels through an approximately constant-field region following a nearly parabolic path throughout the length of the tube. Finally it is diverged at the exit of the tube as it enters a second zero-field region.

This kind of accelerating structure, known as a three element system (EL 53), has a converging action as the beam passes from the field free region into the uniform field inside the tube and a diverging action as the beam leaves the tube to enter a second field free region. The total effect is to converge the beam since the beam enters the tube at low kinetic energy and leaves at a higher kinetic energy, so that the positive action of the input lens is greater than the negative action of the output lens.

A section of an old accelerating tube from the Chalk River Van de Graaff accelerator was used. It consists of sixteen saucer shaped electrodes with uniformly increasing inside diameter separated by one inch thick glass insulating rings. The electrode shape prevents the beam from "seeing" the glass, thus minimizing the build-up on the glass of any contamination scattered by the beam and protects the metal to glass vacuum seals from exposure to scattered beam.

For practical reasons it was desirable to have the tube as short as possible. Because the column had some cracks in the glass insulators, 12 KV was considered to be the maximum safe

potential difference between individual electrodes. A maximum accelerating voltage of 180 KV then required a total of sixteen electrodes. The diameter of the hole in the first electrode was 8 cm.

The distance between the first electrode of the accelerating tube and the last electrode of the Einzel lens was thought to be not too critical, because the focal distance (exit point) of the Einzel lens could be changed by varying the potential in the lens. However, there is a maximum distance at which the first electrode can be placed, that is, when the diameter of the beam equals the inside diameter of the electrode. With a beam diverging from the exit point of the Einzel lens at a half angle of 4^{o} the maximum distance for an electrode, 8 cm in diameter, is approximately 60 cm. To arrive at the optimum distance a trial and error method was used. Due to the fact that it was desirable to have the whole assembly as short as possible, one-tenth of the maximum distance was chosen. Also there is appreciable aberration if the whole diameter is used.

The accelerating tube was tested with the ion source and Einzel lens operating under normal conditions. In the energy range 100 to 180 KeV a nearly parallel beam, 3 to 6 mm in diameter, was obtained. However, below this energy it was necessary to reduce the effective number of electrodes to obtain similar focusing characteristics. This can be explained by the fact that by shortening the effective length of the tube, the gradient between the remaining electrodes was increased to a

value similar to the one used in the high energy range. The shortening can be done on either side of the tube, but it was found that better results can be obtained if it is done on the ion source side.

The high voltage was distributed uniformly along the accelerating tube by means of 15 (20 MΩ, 5 W each) high voltage resistors attached to the electrodes in a zig-zag fashion and placed above the tube. To prevent corona from the somewhat irregular resistor chain, five flat aluminium rings were evenly distributed along the tube. With the maximum high voltage applied to the tube, no corona was observed.

Because of the short length of the accelerating tube and the relatively large inside diameter of the electrodes, the conductance of the tube was adequate for the gas load from the ion source.

A short "extension tube" couples the accelerating tube to the analyzing magnet and provides a connection to the vacuum system. This tube also holds a pair of water cooled tantalum beam choppers which are used to check the characteristics of the beam before it is analyzed.

B.1.3. High Voltage

A d.c. UNIVERSAL VOLTRONICS Model BAL-130-14 power supply was used to provide the main accelerating voltage. It contains a conventional solid state Cockroft & Walton voltage doubler

in one tank and a double LC filter unit in a second tank.

The power supply is able to deliver 5 mA at 150 KV, or 14 mA maximum at 130 KV with a 3% R.M.S. ripple. The ripple is attenuated by a factor of 1/100 by the filter unit.

The high voltage was later increased to 180 KV in order to cover the first resonance in the reaction $^{11}B(p,\gamma)^{12}C$ which occurs at a proton energy of 163 KeV in the laboratory frame. The extra 30 KV was provided by a UNIVERSAL VOLTRONICS Model BPE-32-5.5 power supply. It was placed in the accelerator terminal in series with the main high voltage set. This power supply can deliver 5.5 mA with a 1.5% R.M.S. ripple.

A UNIVERSAL VOLTRONICS 5 KW, 115/115 V, 200 KV isolating transformer supplies a.c. power to the electronic equipment in the accelerator terminal.

A chain of high voltage low temperature coefficient resistors R2 (Fig. B-2) totaling 2000 MΩ is used to determine the accelerating voltage (beam energy). The resistors, placed under oil in a PIREX tube, are connected between the anode electrode of the ion source and the ground through a 20 μA, 0.5% tracking microammeter. The whole assembly was calibrated to 1%.

Fig. B-2 shows the power distribution in the accelerator terminal. The electronic units shown in this diagram by the numbered square boxes are listed in Table B-1.

Table B-1 : Accelerator's electronic units

1. Filament a.c. supply (0-30 A)
2. Magnet d.c. supply (0-3 A)
3. Arc d.c. supply (0-3 A)
4. Extraction d.c. supply (0-30 KV)
5. Einzel lens d.c. supply (0-6 KV)
6. Booster d.c. supply (0-30 KV)
7. High voltage d.c. supply (0-150 KV)
8. Isolation transformer 1 : 1 (Isol. 40 KV)
9. Main isolation transformer 1 : 1 (Isol. 200 KV)

B.1.4. The Vacuum System

A 700 l/sec (@ 10^{-5} mm of Hg) oil diffusion pump provides vacuum to the machine. It is coupled, through a water-cooled chevron ring baffle and a liquid nitrogen trap, directly to the "extension tube". The fore-pressure is provided through a ballast tank, by an 80 l/sec (@ 10^{-3} mm of Hg) mechanical pump. The pressure, under normal conditions, with the ion source "OFF", is about 7×10^{-7} mm of Hg measured at the "extension tube".

B.1.5. The Shielding

The components in the accelerator terminal were assembled on two steel frames, one isolated at the extractor potential (30 KV) with respect to the other. Both frames are supported by four ceramic insulators attached to another steel frame at ground potential .

To avoid corona the whole high voltage assembly was enclosed in an aluminium shielding box. The controls, situated inside the box, are manipulated externally by means of LUCITE rods. A series of meters, mounted inside the box behind a LUCITE window, are used to indicate the operating conditions. No corona was observed when the full voltage was applied.

An aluminium fence, supporting a 1/8 inch thick lead sheet, was built around the accelerator and accelerating tube, for protection against the high voltage and to shield the room from X-rays.

B.1.6. Characteristics

A typical set of conditions for a 160 KeV proton beam under normal operating conditions is shown in Table B-2. An extractor channel 0.008 inch in diameter was used throughout the experiment. The machine was operated for continuous periods up to 76 hours without observing any significant change in its performance. The filament was found to have a life of approximately 400 hours with hydrogen gas. A picture of the accelerator is shown in Fig. B-3 and the accelerating column is shown in Fig. B-4.

B.2. The Magnetic Analyzer

In order to analyze the nearly parallel beam produced by the accelerator, a 45° deflection magnetic analyzer was designed and built by the author.

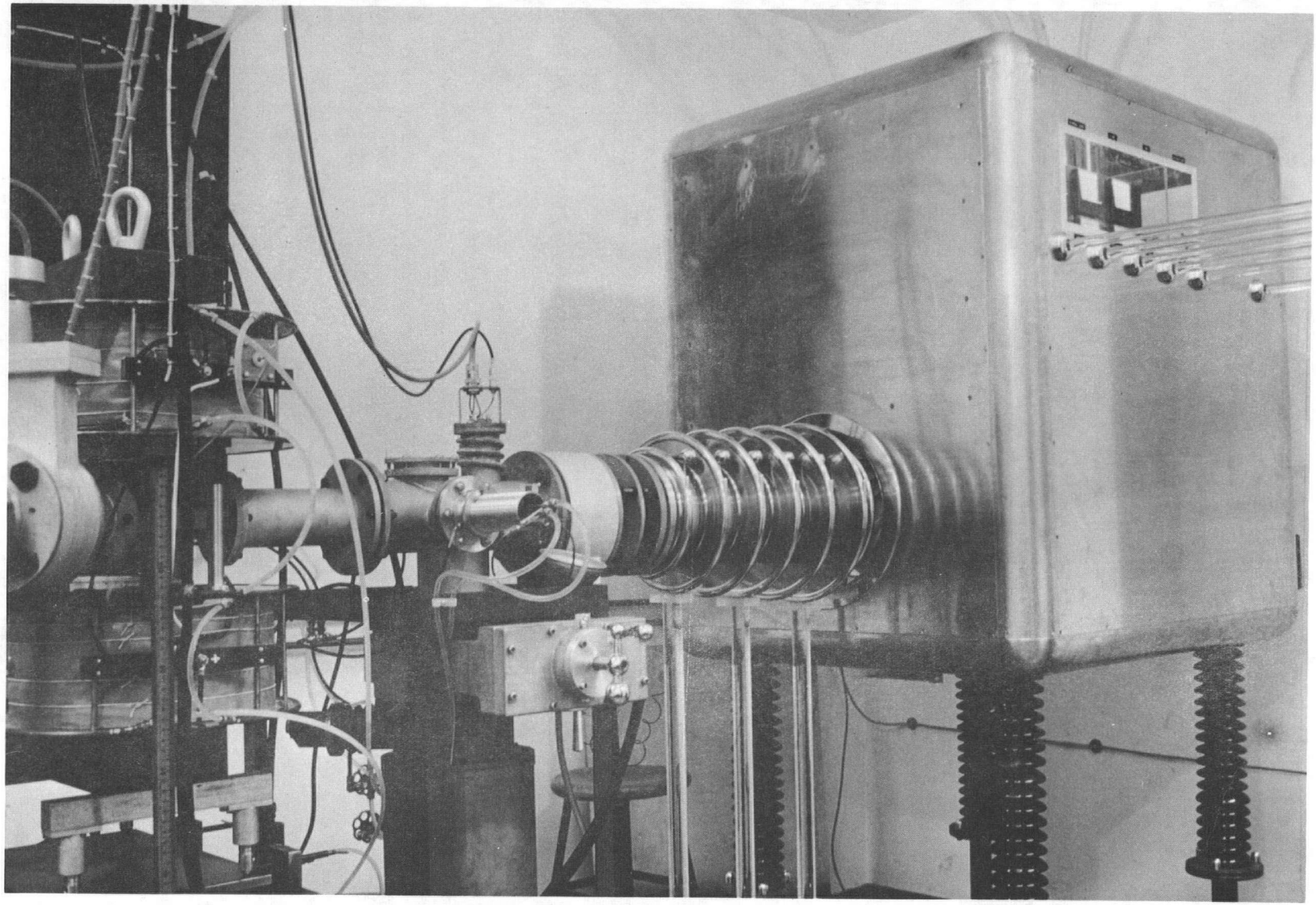

FIG. B–3 : VIEW OF THE ACCELERATOR. THE MAGNETIC ANALYZER IS SHOWN AT THE LEFT.

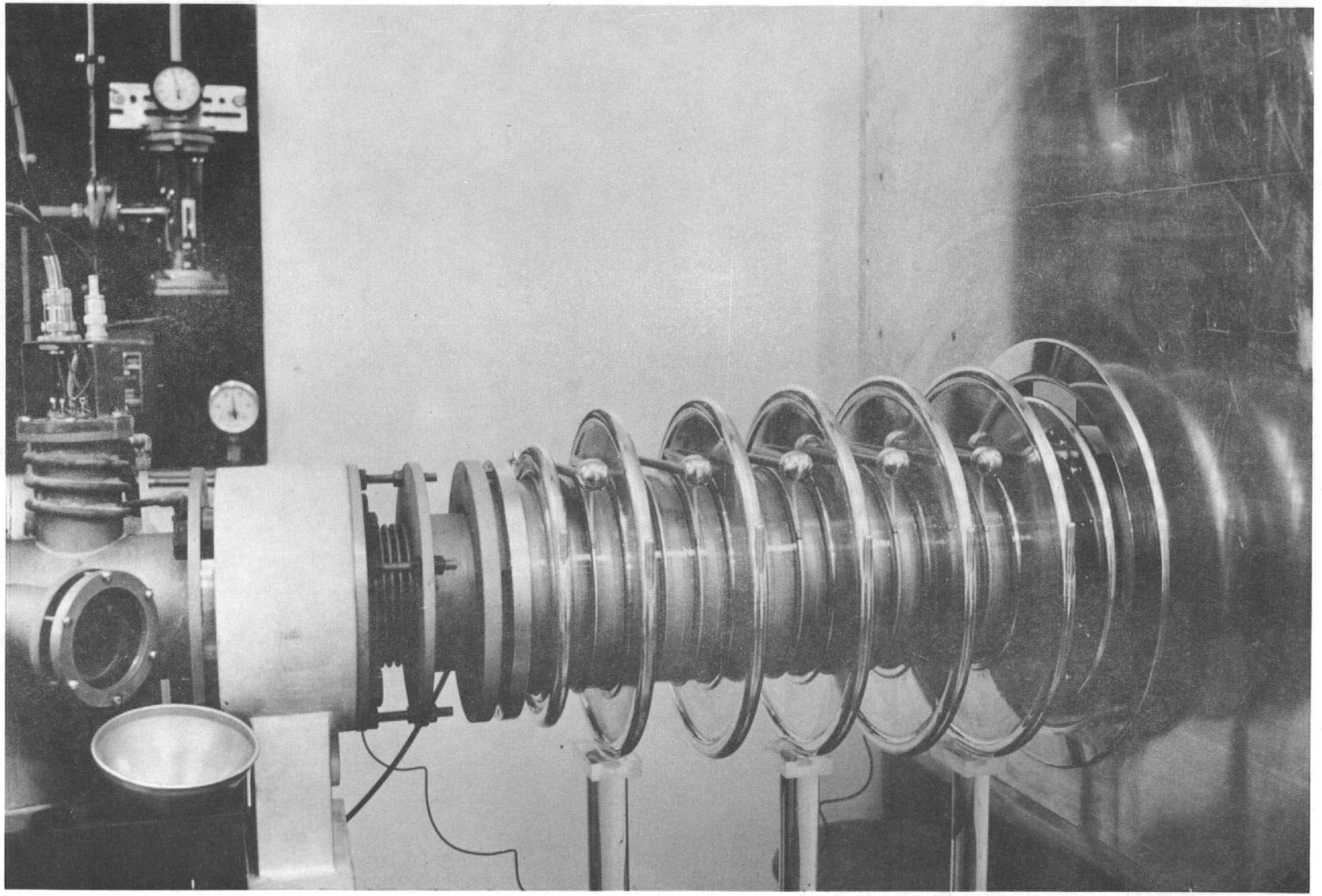

FIG. B–4 : CLOSE-UP VIEW OF THE ACCELERATING COLUMN.

Table B-2 : Typical accelerator conditions for a 160 KeV proton beam.

Thermal leak	0.66	A (approx. 0.2 mm of Hg in the arc chamber)
Filament	26.0	A (approx. 30 W)
Arc voltage	88.0	V
Arc current	1.4	A
Intermediate electrode	30.0	V
Magnet current	0.6	A
Extraction voltage	10.2	KV
Einzel lens	0.0	V
H_1^+ beam current	300.0	μA
Vacuum	8.7×10^{-6}	mm of Hg

B.2.1. The Magnet

The magnet can transmit a $^4He^+$ beam of 200 KeV. The yoke has a conventional C-shape with two identical coils placed at both sides of the magnet gap. The pole tips were designed to have a double focusing effect on the beam in the manner discussed by W. Cross (CR 51).

The conditions for double "line focusing" (that is, for concentrating to a point a parallel beam of particles which has a finite cross section) can be expressed by the following geometrical relationships:

$$\tan \varepsilon_2 = \frac{1}{2}\left[\tan(\Phi-\varepsilon_1) + 1/(\Phi - \cot \varepsilon_1)\right] \qquad \text{(B.2.1. - 1)}$$

$$1/\ell'' = \frac{1}{2}\left[\tan(\Phi-\varepsilon_1) - 1/(\Phi - \cot \varepsilon_1)\right] \qquad \text{(B.2.1. - 2)}$$

where, following Cross' notation, l_o'' is the image distance (in units of the radius of curvature of the mean particle in the uniform magnetic field) measured from the edge of the pole tip; ε_1 is the angle between the incident particles and the normal to the edge of the pole tip; similarly ε_2 is for the emerging mean particle; and Φ is the deflection angle of the mean particle in the uniform field. The equations (B.2.1. - 1) and (B.2.1. - 2) are valid provided the pole gap is small compared to the length and radius of curvature of the particle's path in the uniform magnetic field. Fig. B-5 shows the shape of the pole tip chosen and the trajectory of the mean particle, where ρ is its radius of curvature.

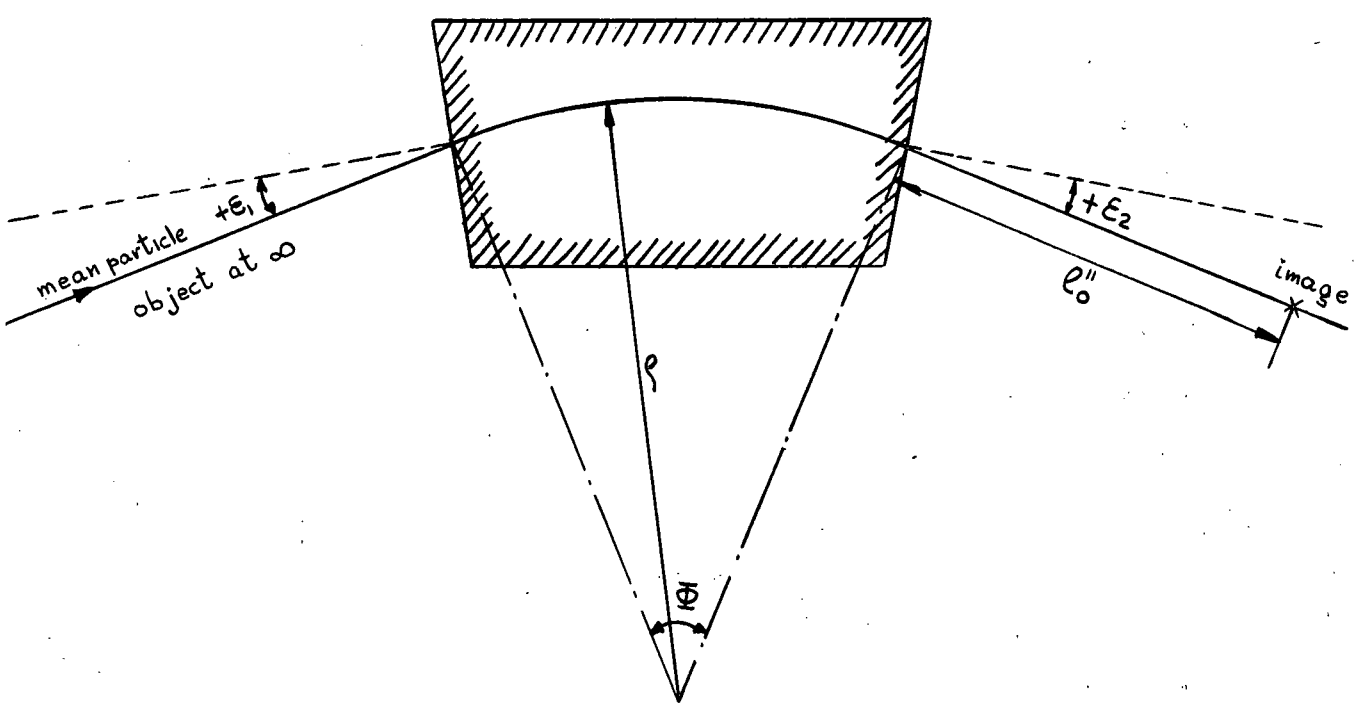

Fig. B-5 : View of the pole tip in the horizontal plane of deflection, ($\vec{B}$ perpendicular to the page), and trajectory of the mean particle.

It was desirable to have l''_o as large as possible. The minimum in the equation B-2 occurs for ε_1 approximately equal to $+12^\circ$. Taking this value for ε_1; the final design parameters were:

$$\Phi = 45^\circ$$
$$\varepsilon_1 = +12^\circ$$
$$\varepsilon_2 = +11^\circ\ 9'$$
$$l''_o = 2.3$$
$$\rho = 15.0 \text{ cm}$$
$$d = 3.175 \text{ cm (air gap)}$$

B.2.2. The Power Supply

A regulated d.c. power supply was built. The circuit is a modified version of the 100 A power supply used to drive the U.B.C. spectrometer (SM 61). Its main characteristics are: I = 20 A (max.) ; E = 90 V ; ripple = 0.05% (R.M.S.). The stability was better than 0.3% over an 8 hour period.

APPENDIX C

THE ENERGY OF THE GAMMA-RAYS FROM THE REACTION $D(p,\gamma)^3He$ AND THE COORDINATE SYSTEM TRANSFORMATIONS

The energy of the gamma-rays in the center of mass system is given by:

$$E'_\gamma = \frac{M_D}{M_p+M_D} E_p + Q - \frac{\left(\frac{M_D}{M_p+M_D} E_p + Q\right)^2}{2 M(^3He) c^2} \qquad (C-1)$$

where E_p is the energy of the incoming protons in the laboratory system. Using the relativistic transformation equations, the gamma-ray energy in the laboratory system is found to be:

$$E_\gamma = E'_\gamma \frac{\sqrt{1-\beta^2}}{1-\beta\cos\theta_L}$$

where θ_L is the angle of the emitted gamma-ray with respect to the incoming particle in the laboratory system and

$$\beta = \frac{M_p}{M_p+M_D} \sqrt{\frac{2E_p}{M_p c^2}}$$

This reaction has a Q = 5.49 MeV. At E_p = 160 KeV the third term in the equation (C-1), which corresponds to the nuclear recoil energy, is negligible. The energies of the gamma-rays as a function of the incident proton energy and as a function of the angle of observation, computed for this experiment, are shown in Table C-1.

The variation of the gamma-ray energy at E_p = 160 KeV over the observed angles is less than 1.1% (and less than 1% at

E_p = 90 KeV). In the computation of the gamma-ray intensity (Chapter III) this variation was not taken into account.

Table C-1 : $D(p,\gamma)^3He$ gamma-ray energies at E_p = 160 KeV and E_p = 90 KeV for different angles of observation.

E_p (KeV)	E_γ (MeV)		
	$\theta_L = 0^o$	$\theta_L = 90^o$	$\theta_L = 135^o$
160	5.63	5.60	5.57
90	5.58	5.55	5.53

In order to obtain the angular distribution in the centre of mass system (Chapter III) the experimental data (Tables III-1 and III-2) were accordingly transformed using the following equations:

$$\theta' = \tan^{-1}\left\{\frac{\sin\theta_L\sqrt{1-\beta^2}}{\cos\theta_L - \beta}\right\}$$

and

$$d\Omega' = d\Omega_L\left\{\frac{1-\beta^2}{(1-\beta\cos\theta_L)^2}\right\}$$

APPENDIX D

NUCLEAR INSTRUMENTS AND METHODS 57 (1967) 353–354; © NORTH-HOLLAND PUBLISHING CO.

LOW COST DEUTERATED POLYETHYLENE TARGETS OF CONTROLLED THICKNESS FOR HIGH CURRENT ACCELERATORS

M. A. OLIVO and G. M. BAILEY

Physics Department, University of British Columbia, Vancouver, Canada

Received 13 September 1967

Thin copper backed deuterated polyethylene targets have been prepared and their performance and characteristics compared with commercial deuteride targets.

Experimental studies on the reaction $D(p,\gamma)^3He$ being carried out in this laboratory required thin deuterium targets of known composition capable of withstanding a large beam current of 160 keV protons. Solid copper backed targets of zirconium-deuteride and titanium-deuteride, soldered to a water cooled target rod have proved the most stable, but have the disadvantage of having an uncertain composition as well as producing considerable multiple scattering at these low energies.

Thin self-supporting deuterium targets of polyethylene on carbon have been developed in this laboratory by Tripard and White[1]). We have applied their technique to prepare solid backed deuterated polyethylene targets and found them to have a number of advantages. These targets are relatively stable, have a well defined composition $(C_2D_4)_n$, and for the same energy loss give less multiple scattering and a higher γ-ray yield than deuteride targets.

Targets were prepared by dissolving a weighed quantity of deuterated polyethylene* in boiling xylene. The solution is gently boiled for at least 2 min and then carefully poured on to a horizontal 0.025 cm thick copper backing which had previously been cleaned and flattened. Surface tension keeps the solution within the confines of the target backing while the xylene slowly evaporates at room temperature, in a dust free atmosphere. In the present case targets of about 40 μg/cm were prepared on a 15 cm^2 copper backing by dissolving 600 μg of the polyethylene in 1 g of xylene. Target performance has been compared with commercial

* Deuterated polyethylene (>98%D) obtained from Merck, Sharp and Dohme of Canada Ltd., Montreal, Canada.

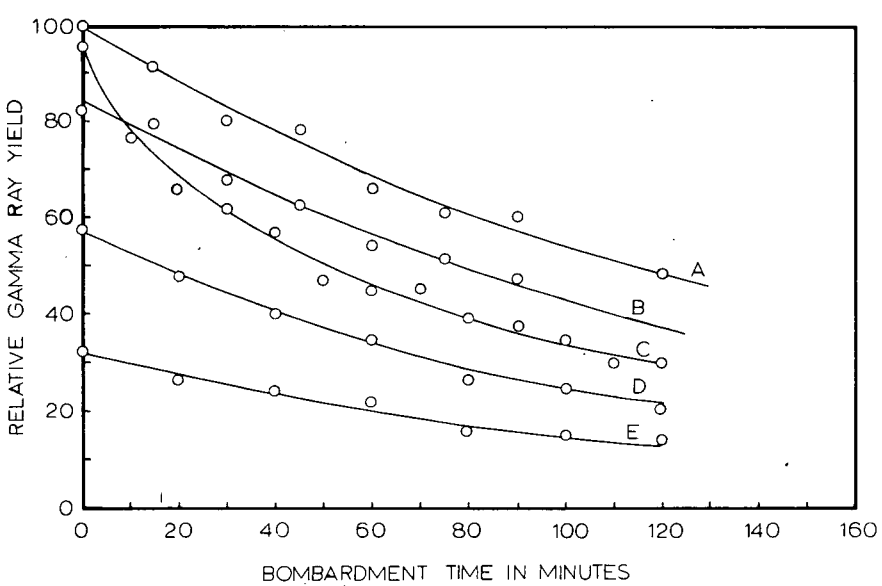

Fig. 1. Target deterioration for solid water cooled targets of zirconium-deuteride and deuterated polyethylene. The curves have been normalized to correspond to an initial deuterium content of 2.8×10^{18} atoms/cm^2. Targets A and B correspond to commercial deuteride targets of equal thickness (nominally 280 μg/cm^2 for an assumed composition $ZrD_{1.5}$), bombarded with 60 μA of 160 keV protons. Curves C, D and E correspond to polyethylene targets $(C_2D_4)_n$ of thickness 40 μg/cm^2 bombarded with 60 μA, 40 μA and 25 μA of 160 keV protons respectively. The beam spot in all cases was a circle of area 20 mm^2.

TABLE 1

Target	Deuterium content (atoms/cm²)	Thickness (μg/cm²)	Energy loss (keV)	<θ>* (deg)
$ZrD_{1.5}$	2.8×10^{18}	280	71	10
$(C_2D_4)_n$	2.8×10^{18}	40	32	1½

* The rms multiple scattering angle <θ> has been calculated from the work of Williams[2]).

deuteride targets by monitoring the 90° γ-yield from the $D(p,\gamma)^3He$ reaction with a 12.5 cm × 10 cm NaI(Tl) crystal. In all cases the targets were clamped to a 1.6 mm thick water cooled copper plate which was an integral part of the target rod assembly. Protons of 160 keV, collimated to give a target spot of 20 mm² were used to check target deterioration. The beam current variation was less than 5% for these tests and a number of target spots were run to allow for possible bad thermal contact with the cooled mount. The result of these tests are summarized in fig. 1.

The difference between curves A and B illustrates the uncertainty in the composition of deuteride targets, which can contain anything from one to two atoms of deuterium per atom of zirconium. From these curves it can be inferred that the deuteride targets give superior yield and stability for a given deuterium content. However, if the energy loss or the multiple scattering of the protons is of prime concern, the polyethylene targets are superior. This is indicated in table 1.

The rapid initial deterioration of the polyethylene targets at high beam currents appears to be a surface effect and is probably due to poor thermal conduction through the polymer. It is quite possible that the polymer itself breaks down losing deuterium in the process. It is interesting to note that at a later stage the deterioration is comparable to the deuteride targets. The present tests at 60 μA correspond to a beam current density of 0.3 mA/cm² at the target.

The polyethylene targets are extremely simple to make and with practice one can judge a good target from the uniformity of the surface. A reject target would have a noticeable shrinkage pattern on its surface. We have made as many as 30 targets in a day and had only two failures. Thickness variation across the surface (excluding the edges) of a target is typically 10% but this could be improved with careful attention to the surface flatness and horizontal mounting of the backing and a controlled drying environment. A characteristic of these targets is that they rapidly show a dark spot even when bombarded with quite small beams. This deposit, presumably carbon from breakdown of the polymer, does not seem to affect the performance of the target, and has in fact proved useful in determining the profile of the beam spot.

Targets made by this technique are quite inexpensive compared with the commercial deuteride targets and can be made to any physical size. Further tests to reduce target deterioration are planned using a rapidly rotating target holder.

References

1) G. E. Tripard and B. L. White, Rev. Sci. Instr. **38** (1967) 435.
2) E. J. Williams, Rev. Mod. Phys. **17** (1945) 217.

APPENDIX E

MULTIPLE SCATTERING

The mean square multiple scattering angle of charged massive particles is given in the centre of mass system by (MO 65):

$$\langle\theta^2\rangle = 2K \ln\left(\frac{K^{1/2}}{\theta_{min}}\right) \qquad (E-1)$$

where $K = \pi Nt\, Z_1^2 Z_2^2 e^4 (M_1 + M_2)^2 M_2^{-2} E^{-2}$; Nt being the number of scattering nuclei/cm^2, Z_2 and M_2 the atomic number and mass of the scattering nuclei, and Z_1 and M_1 the corresponding quantities for the incident particles, which possess an energy E in the laboratory frame. θ_{min} is defined by:

$$\theta_{min} = \begin{cases} 2.1\, Z_2^{1/3} \hbar (M_1+M_2)/(a_o M_2 \sqrt{2M_1E}) & (Z_1Z_2e^4/\hbar\sqrt{2EM_1^{-1}} < 1) \text{ (a)} \\ 3.8\, Z_2^{4/3} e^2 (M_1+M_2)/(2a_o M_2 E) & (Z_1Z_2e^2/\hbar\sqrt{2EM_1^{-1}} > 1) \text{ (b)} \end{cases} \qquad (E-2)$$

a_o being the Bohr orbit radius.

For the $(CD_2)_n$ compound the total R.M.S. multiple scattering angle was calculated using the following expression:

$$[\theta] = \sqrt{\langle\theta_D^2\rangle + \langle\theta_C^2\rangle}$$

where $\langle\theta_D^2\rangle$ and $\langle\theta_C^2\rangle$ are the mean square multiple sacttering angles due to the deuterium and carbon atoms, respectively.

To calculate $[\theta] = \sqrt{\langle\theta^2\rangle}$ a program was written using a

PDP-8 computer, available in this laboratory. A test is included in the program to determine which of the two conditions referred to in equation (E-2), (a) wave or (b) classical, applies.

The values of the multiple scattering angle shown in Table II-1 were calculated assuming that the energy of the incident particles remains constant as they traverse the target. The values in column 2 were obtained at an energy equal to the incident energy. The equation (E-1) indicates that the scattering angle increases as the particle energy decreases. Thus a more reliable estimate for the multiple scattering angle is obtained (column 6) at an energy which is the average over the thickness of the target. That is at $\overline{E}_p = E_p - \Delta E/2$.

APPENDIX F

THE REACTIONS $^{12}C(p,\gamma)^{13}N$ AND $^{13}C(p,\gamma)^{14}N$

The maximum available energy for the gamma-ray transitions in the reaction $^{12}C(p,\gamma)^{13}N$ is

$$E_\gamma \simeq \frac{M(^{12}C)}{M_p + M(^{12}C)} E_p + Q = \frac{12}{13} 0.160 + 1.941 = 2.089 \text{ MeV}$$

which is below the 2.95 MeV discrimination level used in the computation of the gamma-ray intensity (Chapter III). The total cross section, for 160 KeV protons, is $\sigma(^{12}C)=4.6 \times 10^{-3}$ μb. In the $^{13}C(p,\gamma)^{14}N$ reaction the maximum available energy for the gamma-ray transitions is

$$E_\gamma \simeq \frac{M(^{13}C)}{M_p + M(^{13}C)} E_p + Q = \frac{13}{14} 0.160 + 7.546 = 7.695 \text{ MeV}$$

The total cross section, for 160 KeV protons, is in this case $\sigma(^{13}C)=2.5 \times 10^{-2}$ μb (which is comparable to the $\sigma(D)=8 \times 10^{-2}$ μb for the isotropic component in the $D(p,\gamma)^3He$ reaction at the same bombarding energy). The finite value of the cross section indicates the possibility of having gamma-rays of that energy or lower (due to cascades to the various levels in the ^{14}N) which will be present as an indiscriminated beam dependent background together with the 5.6 MeV from the $D(p,\gamma)^3He$ reaction. Because only 1.11% of ^{13}C is present in the natural carbon the total gamma-ray contribution from the reaction involving this isotope will be proportional to $\sigma(^{13}C) \times 1.11 \times K/100 = 2.8 \times K \times 10^{-2}$ compared with $\sigma(D) \times 2 \times K = 16 \times K$ from the $D(p,\gamma)^3He$, (in K were

included the appropriate units; the factor 2 arises from the composition of the target). This means that in the gamma-ray yield arising from $D(p,\gamma)^3He$ and $^{13}C(p,\gamma)^{14}N$ only 0.17% will be due to the second reaction. Its contribution can therefore be neglected.

The total cross sections for the reactions $^{12}C(p,\gamma)^{13}N$ and $^{13}C(p,\gamma)^{14}N$ were evaluated at 160 KeV from the results given by Hall and Fowler (HA 50). In the first reaction the cross section was extrapolated using their semi-empirical expression $\sigma(^{12}C)=0.0024\ E^{-1}\ \exp(-6\ E^{-\frac{1}{2}})$ which was found to fit the 88 KeV and 128 KeV data. The extrapolation is in good agreement with the experimental value of $\sigma(^{12}C)=(5.0 \pm 0.3) \times 10^{-3}$ μb obtained at 161 KeV by Bailey and Stratton (BA 50). For the second reaction the same energy dependance $\sigma(^{13}C)=a\ E^{-1}\ \exp(b\ E^{-\frac{1}{2}})$ was used. The parameters a and b were found by fitting this expression to the experimental cross section obtained at 114 KeV and 126 KeV by Lamb and Hester (LA 57). The cross section so obtained may be somewhat out from the actual value. Woodbury and Fowler (WO 52) using the single level Breit-Wigner dispersion formula determined the contribution of the 554 KeV and the broad 1.25 MeV resonances to the cross section at 129 KeV. It was found that nearly 75% was due to these resonances. However, we are here only interested in knowing the order of magnitude of the cross section. The extrapolated value is then acceptable because:

a. the extrapolation was based on cross sections obtained experimentally, thus they include the contribution from the resonances and

b. the extrapolation was done to an energy which is only 30% higher than the one in which the experimental data was obtained.

APPENDIX G

CORRECTION DUE TO THE GAMMA-RAY ABSORPTION IN THE TARGET HOLDER

Assume a point source of gamma-rays whose intensity per unit of solid angle is I_i, Fig. G-1.

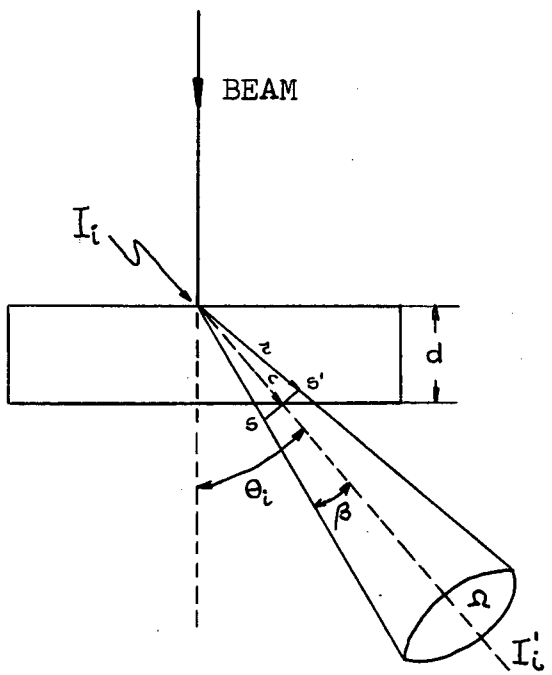

Fig. G-1 : Target holder absorption correction

I_i' is the transmitted gamma-ray intensity integrated over the solid angle of the detector and d the thickness of the absorber. For simplicity it is assumed that the cone subtended by the detector cuts at the target holder in SS'.

Then

$$c = \frac{d}{\cos\theta_i} \quad \text{and} \quad r = \frac{c}{\cos\beta} \quad \therefore \quad r = \frac{d}{\cos\theta_i \cos\beta}$$

$$I_i' = \left(2\pi I_i \int_0^{\beta} e^{-\mu \frac{d}{\cos\theta_i \cos\beta}} \sin\beta \, d\beta \right) \Big/ \int_{\Omega} d\Omega$$

where μ is the total linear attenuation coefficient. If the target holder is made of different materials, then

$$\mu d \Rightarrow \sum_j \sigma_j \rho_j d_j$$

where σ_j is the total mass attenuation coefficient for a given material, ρ_j its density and d_j its thickness. We have finally

$$I_i = I_i'/Z_i$$

where the correction factor Z_i is

$$Z_i = \int_0^{\beta} e^{-\frac{\sum_j \sigma_j \rho_j d_j}{\cos\theta_i \cos\beta}} \sin\beta \, d\beta \Big/ (1 - \cos\beta)$$

The Target Holder "TA": A cross section of the target holder "TA" is shown below:

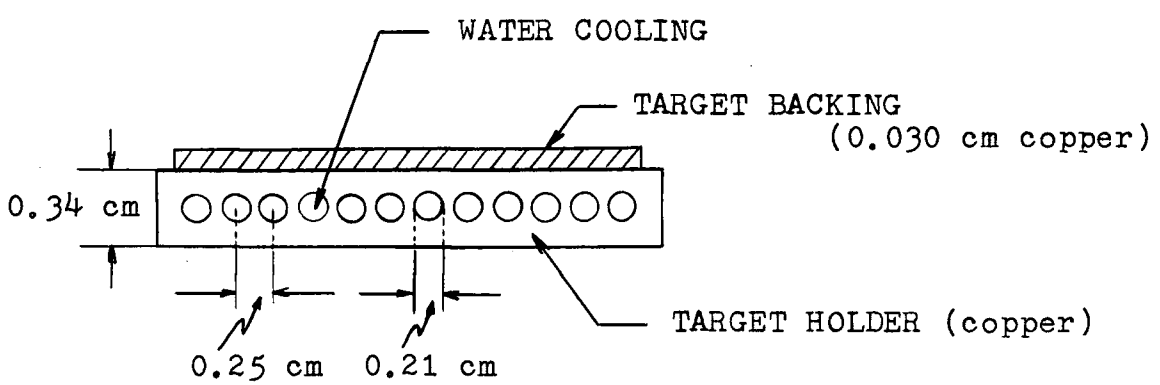

This was assumed to be equivalent to:

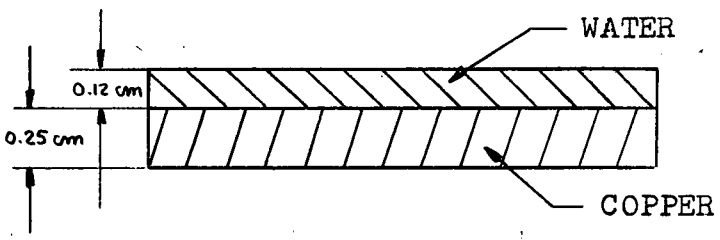

The Target Holder "TB" : A cross section of the target holder "TB" is shown below:

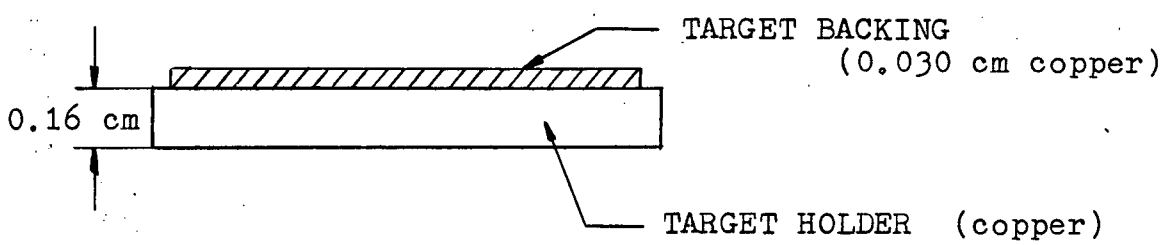

The data used for $D(p,\gamma)^3He$ and $^{11}B(p,\gamma)^{12}C$ absorption corrections are shown in Table G-1. An average gamma-ray energy of 5.58 MeV for the $D(p,\gamma)^3He$ reaction was chosen to determine the mass attenuation coefficients. These vary over the energy range of the gamma-rays shown in Table G-1 by less than 0.5%.

For the $^{11}B(p,\gamma)^{12}C$ the coefficients were determined for E_γ = 11.7 MeV. The mass attenuation coefficients were obtained from the work of G.W. Grodstein (GR 57).

Table G-1 : Target holder correction parameters for the $D(p,\gamma)^3He$ and $^{11}B(p,\gamma)^{12}C$ reactions.

	"TA"				"TB"
	WATER		COPPER		COPPER
	$D(p,\gamma)^3He$	$^{11}B(p,\gamma)^{12}C$	$D(p,\gamma)^3He$	$^{11}B(p,\gamma)^{12}C$	$D(p,\gamma)^3He$
σ (cm^2/g)	0.0286	0.0206	0.0312	0.0308	0.0312
ρ (g/cm^3)	1.0	1.0	8.92	8.92	8.92
d (cm)	0.124	0.124	0.249	0.249	0.189

The target holder absorption correction for holder "TA" was checked with 11.68 MeV gamma-rays from the reaction $^{11}B(p,\gamma)^{12}C$. The results obtained are summarized in Table G-2.

Table G-2 : Target holder absorption measurements for E_γ=11.7 MeV.

θ_1	CALCULATED FRACTION TRANSMITTED	MEASURED FRACTION TRANSMITTED
30°	0.9358	0.94 ± 0.02
45°	0.9219	0.93 ± 0.02
60°	0.8914	0.90 ± 0.02

The experimental results are in good agreement with the calculated absorptions.

APPENDIX H

BEAM DEPENDENT BACKGROUND

The possibility of neutrons arising from secondary processes in the target or from the accelerator during the $D(p,\gamma)^3He$ experiment was considered since it would affect the results of the angular distribution measurements. Such neutrons would interact in the NaI crystal and in the surrounding materials giving rise to an extra gamma-ray yield. Because the gamma-ray yield from the reaction $D(p,\gamma)^3He$ is very small, specially at 0^o, a careful check for such neutron contributions was carried out. At the bombarding energies considered here no direct neutrons can arise from the reaction D(p,n)2p which has a threshold of 3.3 MeV.

H.1. Neutrons Arising from the Accelerator

The hydrogen used in this experiment was natural with 1.5×10^{-3} parts of D_2, therefore deuterium was present in the mass two beam which struck inside of the analyzing magnet vacuum chamber. An accumulation of deuterium in the stainless steel magnet box would give rise to neutrons from the reaction $D(d,n)^3He$.

A thirty hours angular distribution run was performed with a 160 KeV beam hitting a clean copper target. This run was made in order to check whether a neutron background built up after a long period of running. The counting rate was found

to be independent of the position of the detector #1, and equal to the counting rate without the beam, so within the accuracy of the $D(p,\gamma)^3He$ measurement no significant contribution came from the deuterium hitting the magnet box.

H.2. Neutrons Arising in the Deuterated Polyethylene Targets

As was mentioned in Chapter II, neutrons may arise from the reaction $D(d,n)^3He$ caused by the deuterons in the polyethylene target which have picked up energy by collisions with incident protons. Neutron contributions of this kind have been observed for proton energies below 500 KeV when bombarding heavy ice targets (SE 59).

A direct determination of the number of neutrons produced would not give a direct answer to the problem, because the efficiency of the NaI crystal for detecting neutrons was not known. Furthermore, because the neutrons will be scattered in the surrounding materials it would be difficult to evaluate how many will enter the crystal. A further difficulty is to evaluate how many of those gamma-rays which arise from the interaction of the neutrons in surrounding materials are scattered into the crystal.

Because of these difficulties the shape of the spectrum from the detector when bombarded with neutrons was measured and compared to the gamma-ray spectra from the reaction $D(p,\gamma)^3He$.

The neutrons were obtained from the reaction $D(d,n)^3He$,

by bombarding a deuterium gas target with 876 KeV deuterons from the U.B.C. Van de Graaff accelerator. Using the same collimator and shielding geometry as for the $D(p,\gamma)^3He$ runs the detector was placed at 0^o with respect to the incoming beam, with the front face of the crystal 20 cm from the centre of the gas target. The target contained a 0.83 cm beam path in deuterium gas at 200 mm of Hg pressure with a 127 micron Ni window. The spectrum shown in Fig. H-1 was obtained after background subtraction for a total charge of 30 μC delivered to the target in a four minute run at an average current of about 135 nA.

The maximum kinetic energy available for the knock-on deuterium atoms is $E_D(max.) = 8/9\ E_p$ (head on collision). Therefore, for 160 KeV protons we have $E_D = 142$ KeV. The angular distribution of the neutrons from the reaction $D(d,n)^3He$ at a bombarding energy of $E_D = 142$ KeV is approximately isotropic.

The cross section for the isotropic component in the reaction $D(p,\gamma)^3He$ ranges from approximately 0.08 μb at E_p=160 KeV to 0.07 μb at $E_p = 90$ KeV (GR 62 ; GR 63) while the cross section for the reaction $D(d,n)^3He$ varies from approximately 27 mb at $E_D = 142$ KeV to 12 mb at $E_D = 80$ KeV (AR 54). Because the cross section for the reaction $D(d,n)^3He$ falls more rapidly than the $D(p,\gamma)^3He$ the comparison was made with the $D(p,\gamma)^3He$ data obtained at 160 KeV with the detector at 0^o where the gamma-ray yield is minimum. If the neutron background does not show any effect at this energy it certainly will not show any effect

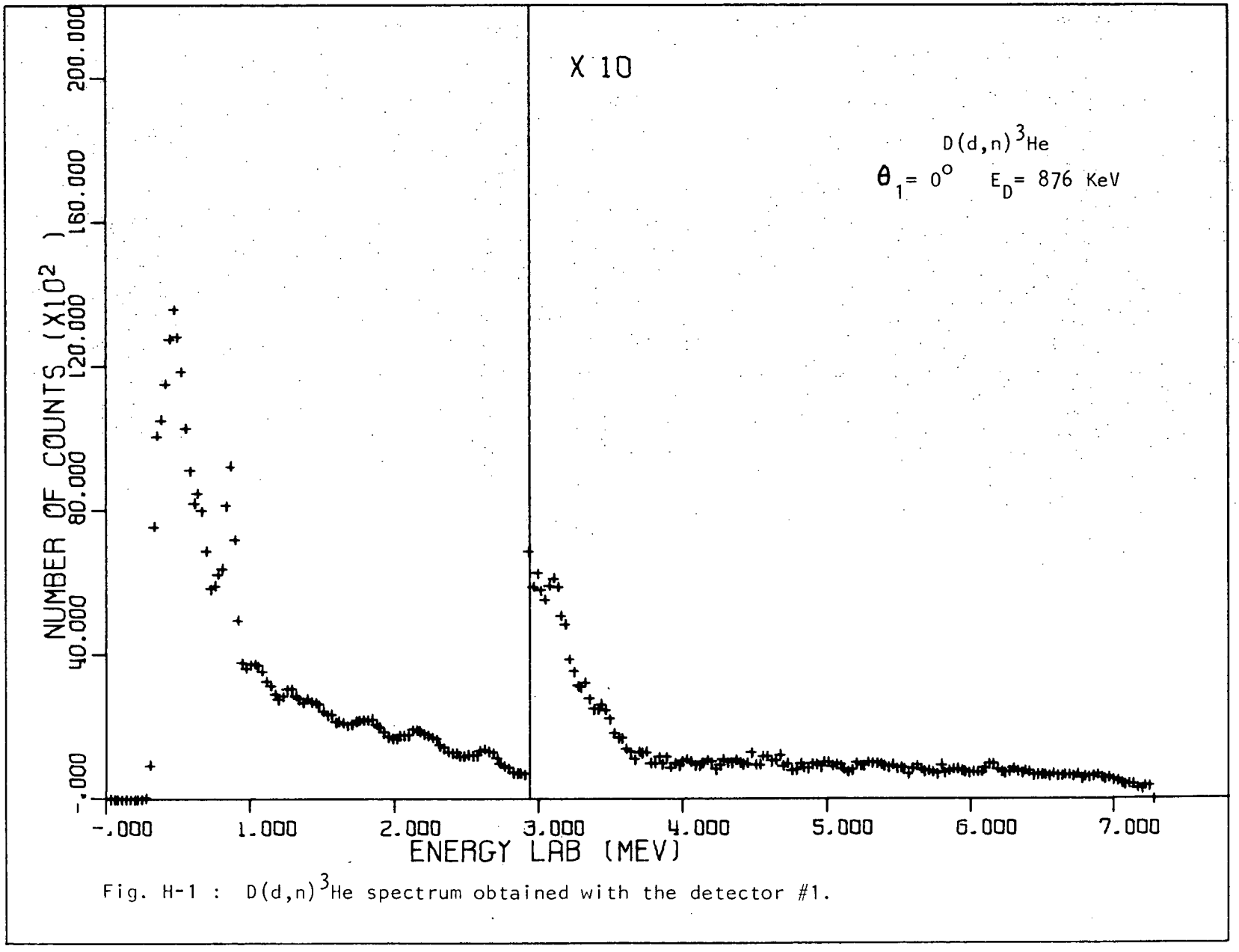

Fig. H-1 : $D(d,n)^3He$ spectrum obtained with the detector #1.

at 90 KeV.

It should be mentioned here that the energy of the neutrons from the gas target at 0° for E_D = 876 KeV, have an energy of 3.99 MeV, while the energy of the neutrons leaving the polyethylene targets at 0° would have a maximum energy of 2.94 MeV (E_D = 142 KeV). However, the shape of the spectrum in the gamma-ray detector does not change appreciably with neutron energy over this range.

Fig. H-2 shows the gamma-ray spectrum from the reaction $D(p,\gamma)^3He$ taken at 0° for E_p = 160 KeV (Table III-2, i=3). Fig. H-3 shows the 0° spectrum with the background removed. It was obtained by subtracting the background spectrum shown in Fig. III-2 when it was normalized to the same running time as for the 0° run. The statistical errors in the low energy channels look very large. However, this is due to the fact that they correspond to small differences between large numbers.

It is more convenient to remove this statistical scatter before comparing this spectrum with the $D(d,n)^3He$ one. The method used to filter out the statistical fluctuations follows the technique described by H.P. Yule (YU 67). It is based on the least squares fitting of the experimental points (number of counts in each channel) to a power function over a small region of the original data.

Let N_i be the number of counts in the channel i.

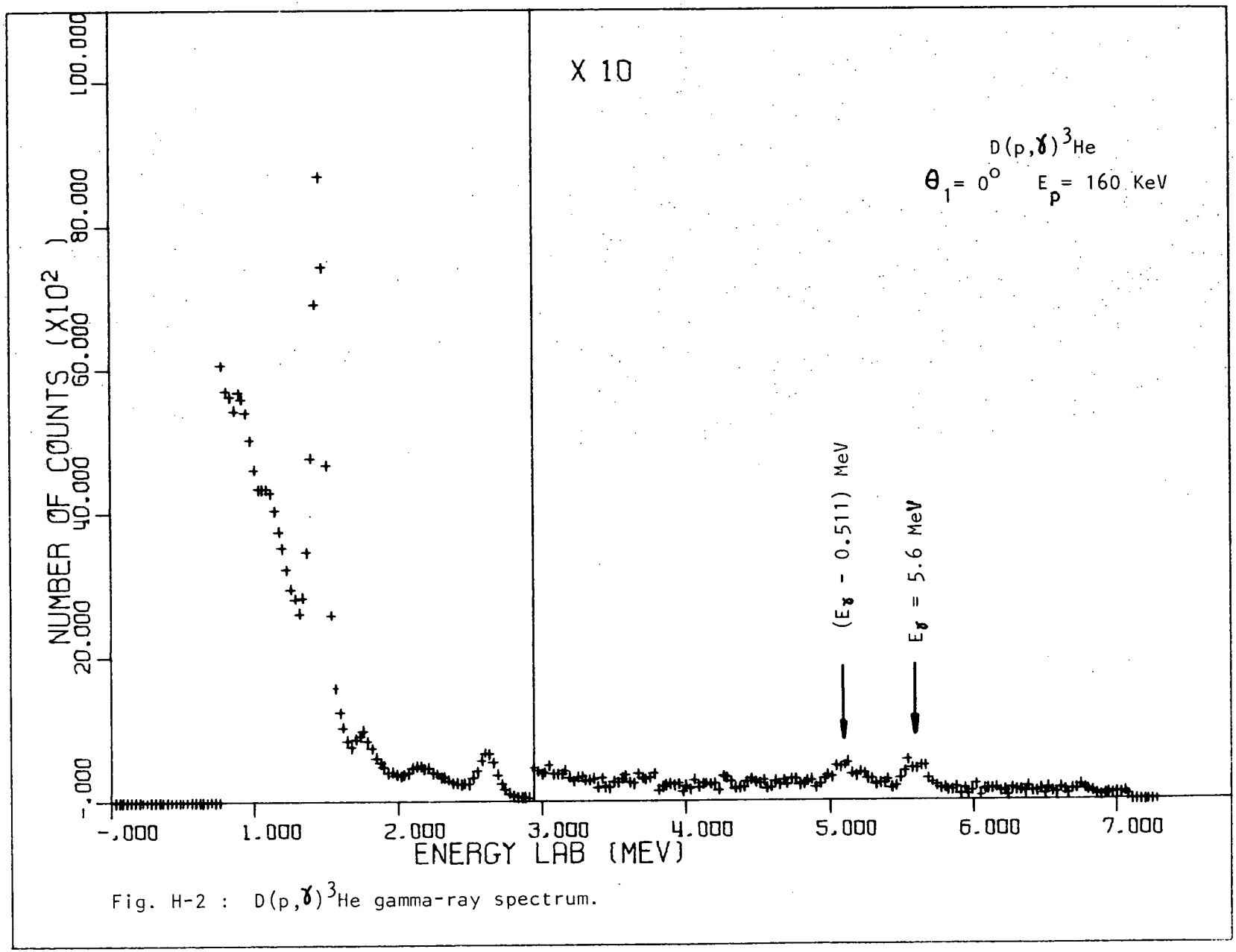

Fig. H-2 : $D(p,\gamma)^3He$ gamma-ray spectrum.

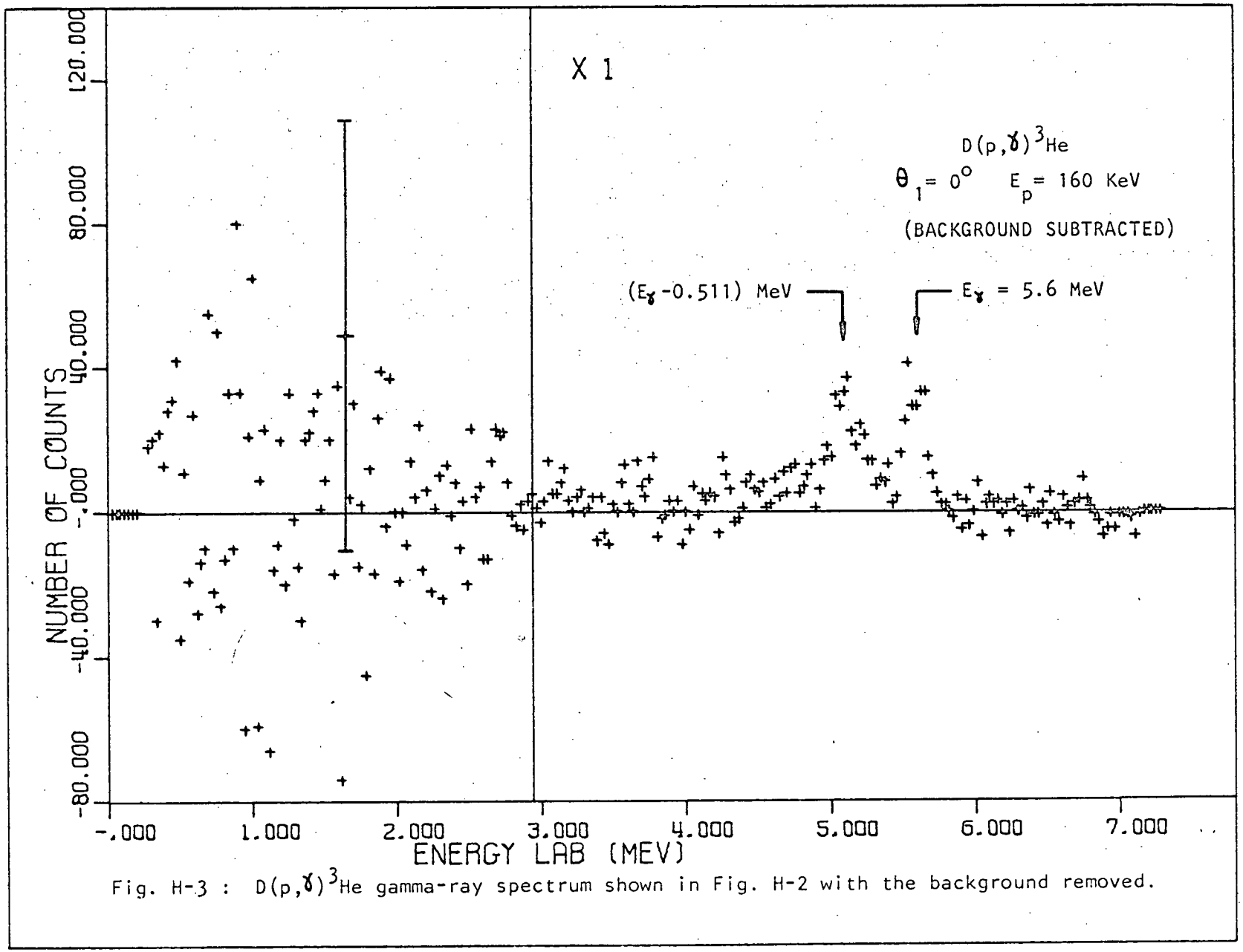

Fig. H-3 : $D(p,\gamma)^3He$ gamma-ray spectrum shown in Fig. H-2 with the background removed.

The smoothed value of N_i is defined as S_i, where

$$S_i = N_m^{-1} \sum_{j=-m}^{j=m} (a_{m,j} N_{i+j}) \qquad (H - 1)$$

The constants $a_{m,j}$ and the normalization constant N_m depend upon the power of the function chosen to which the raw data is to be fitted. Tables of these constants for different degree of polynomials are given by A Savitzky and M. Golay (SA 64).

The equation (H-1) then gives a new value for N_i which is found by fitting m lower channels and m higher channels (including the channel to be smoothed) to a power function $f_i = \sum_{k=0}^{n} b_k i^k$. This process is repeated for all the channels excluding the first and the last m channels.

This technique was applied to the spectrum shown in Fig. H-3. The result is shown in Fig. H-4. This spectrum was obtained under the following conditions:

a. 19 point smooth was used (m=9)

b. A quadratic function was used (n=2)

c. The smoothing process was not carried out for channels above approximately 4 MeV.

d. The process was repeated twice; that is, the original points were smoothed and the new points were smoothed again.

A computer program, written by Bailey (BA 68), was used to carry out the smoothing operation.

In order to assess the significance of a neutron contribution which may be present, the $D(d,n)^3He$ neutron

spectrum, shown in Fig. H-1 was normalized so that the number of counts in the energy range 2.95 to 6.1 MeV was equal to 2% of the number of counts in the same energy range of the gamma-ray system shown in Fig. H-3. Then the normalized neutron spectrum was subtracted from the smoothed gamma-ray spectrum shown in Fig. H-4 to give the curve shown in Fig. H-5. Since the resulting curve is negative in the lower energy range it is clear that too much has been subtracted. Therefore the neutron contribution to the counting rate in the energy range used for evaluating the gamma-ray flux is significantly less than 2% and to the accuracy of these measurements it can be said to be insignificant.

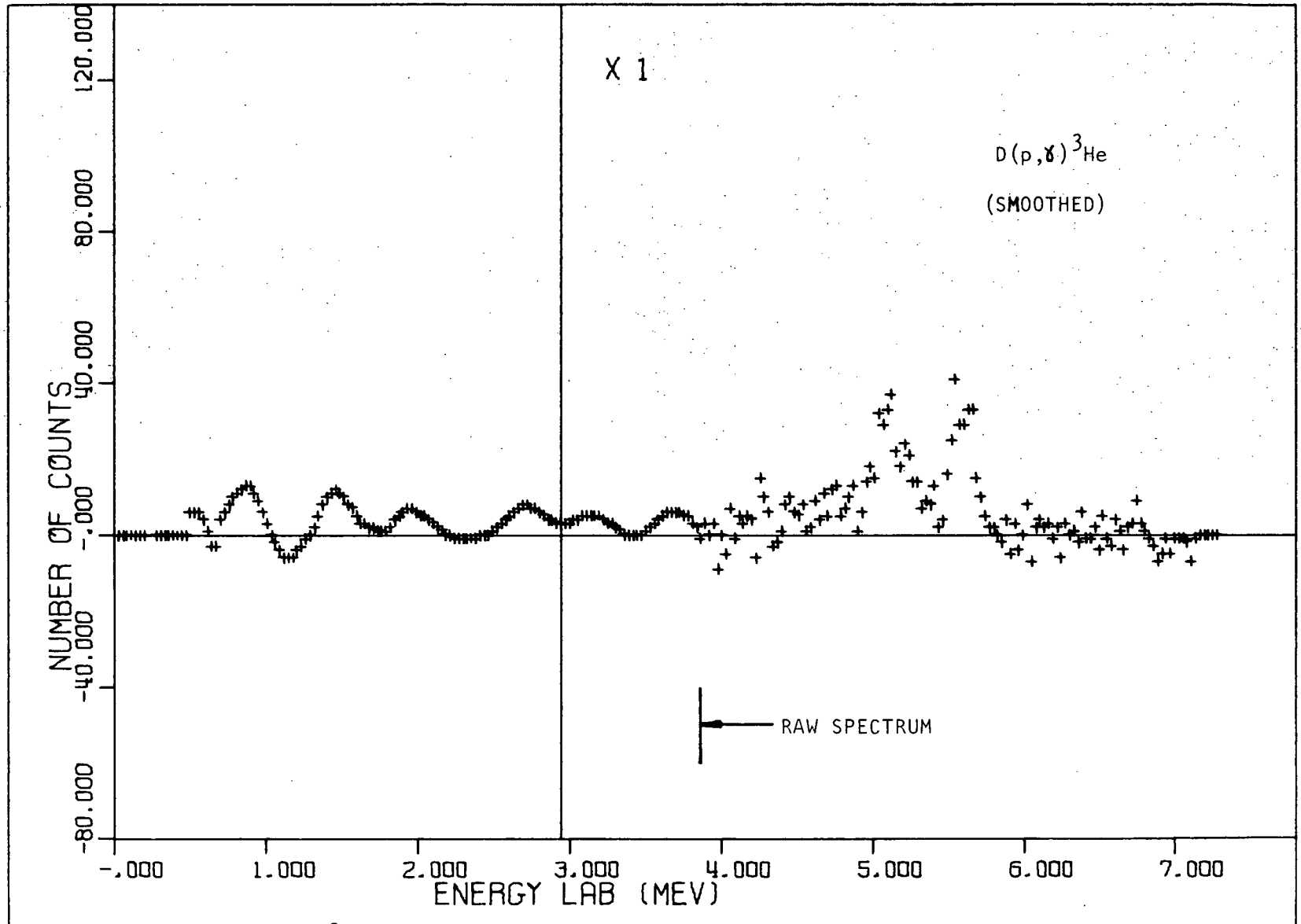

Fig H-4 : $D(p,\gamma)^3He$ gamma-ray spectrum of Fig. H-3 with the first 145 channels smoothed.

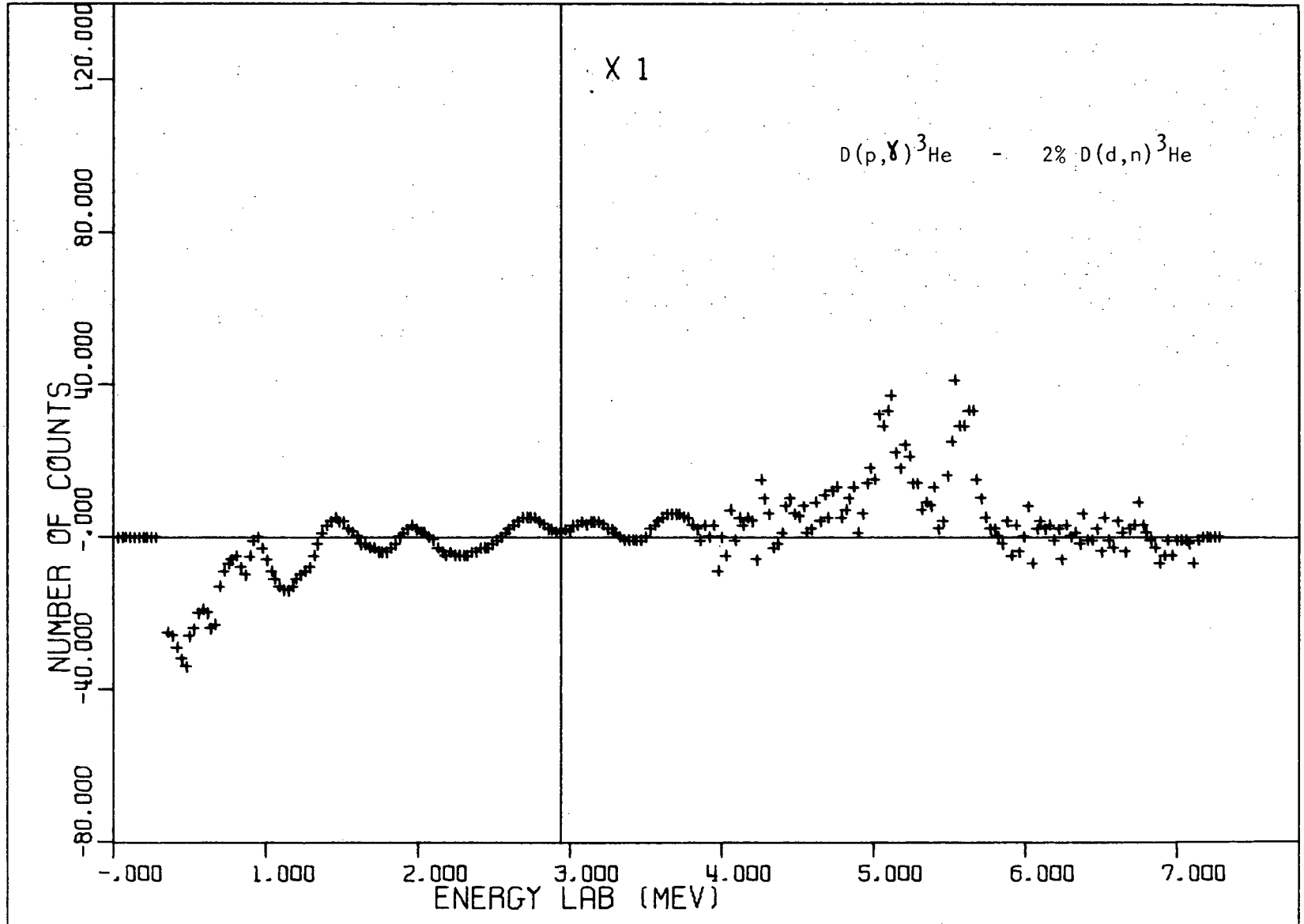

Fig. H-5 : Gamma-ray spectrum obtained by subtracting the normalized neutron spectrum from the spectrum shown in Fig. H-4.

APPENDIX I

LIST OF COMPUTER PROGRAMS USED IN THIS THESIS

Program Name	Function
	IBM 7040/7044
ND-160	TALLY paper tape decoder
SPECTRA	Energy calibration, energy shift and integration of the spectra
NORABS	Background subtraction, normalization and absorption corrections
POLYLS	Initial estimate of the parameters for the iterative least squares fit
MLKH1F	Iterative least squares fit and plotting
COMPSC	Compton scattering calculation front collimator
DE-WFC	Detector efficiency and finite solid angle corrections (smoothing factors)
NDPTHE	Spectra plotting
SMOOTH	Gamma-ray smoothing spectra
KONRAS	Non-relativistic kinematics two body break-up used for the reaction $D(d,n)^3He$
	PDP-8
RMSAMS	R.M.S. Multiple scattering angle calculations